CANADIAN THESES ON MICROFICHE

I.S.B.N.

THESES CANADIENNES SUR MICROFICHE

National Library of Canada
Collections Development Branch

Canadian Theses on
Microfiche Service

Ottawa, Canada
K1A 0N4

Bibliothèque nationale du Canada
Direction du développement des collections

Service des thèses canadiennes
sur microfiche

NOTICE

The quality of this microfiche is heavily dependent upon the quality of the original thesis submitted for microfilming. Every effort has been made to ensure the highest quality of reproduction possible.

If pages are missing, contact the university which granted the degree.

Some pages may have indistinct print especially if the original pages were typed with a poor typewriter ribbon or if the university sent us a poor photocopy.

Previously copyrighted materials (journal articles, published tests, etc.) are not filmed.

Reproduction in full or in part of this film is governed by the Canadian Copyright Act, R.S.C. 1970, c. C-30. Please read the authorization forms which accompany this thesis.

AVIS

La qualité de cette microfiche dépend grandement de la qualité de la thèse soumise au microfilmage. Nous avons tout fait pour assurer une qualité supérieure de reproduction.

S'il manque des pages, veuillez communiquer avec l'université qui a conféré le grade.

La qualité d'impression de certaines pages peut laisser à désirer, surtout si les pages originales ont été dactylographiées à l'aide d'un ruban usé ou si l'université nous a fait parvenir une photocopie de mauvaise qualité.

Les documents qui font déjà l'objet d'un droit d'auteur (articles de revue, examens publiés, etc.) ne sont pas microfilmés.

La reproduction, même partielle, de ce microfilm est soumise à la Loi canadienne sur le droit d'auteur, SRC 1970, c. C-30. Veuillez prendre connaissance des formules d'autorisation qui accompagnent cette thèse.

THIS DISSERTATION
HAS BEEN MICROFILMED
EXACTLY AS RECEIVED

LA THÈSE A ÉTÉ
MICROFILMÉE TELLE QUE
NOUS L'AVONS REÇUE

NL-339 (r. 82/08)

Canada

35

0-315-15945-6

National Library of Canada | Bibliothèque nationale du Canada

Canadian Theses Division | Division des thèses canadiennes

Ottawa, Canada
K1A 0N4

63854

PERMISSION TO MICROFILM — AUTORISATION DE MICROFILMER

• Please print or type — Écrire en lettres moulées ou dactylographier

Full Name of Author — Nom complet de l'auteur

ROGER W. TOOGOOD

Date of Birth — Date de naissance

27 March, 1951

Country of Birth — Lieu de naissance

Canada

Permanent Address — Résidence fixe

Dept. of Mechanical Engineering
Univ. of Alberta

Title of Thesis — Titre de la thèse

Boundary Fitted Coordinate Systems For Estimation of Single and Multi-Element Airfoil Force Coefficients, and Application to Wind Tunnel Corrections

University — Université

University of Alberta

Degree for which thesis was presented — Grade pour lequel cette thèse fut présentée

Ph. D.

Year this degree conferred — Année d'obtention de ce grade

1983

Name of Supervisor — Nom du directeur de thèse

D. J. Marsden

Permission is hereby granted to the NATIONAL LIBRARY OF CANADA to microfilm this thesis and to lend or sell copies of the film.

The author reserves other publication rights, and neither the thesis nor extensive extracts from it may be printed or otherwise reproduced without the author's written permission.

L'autorisation est, par la présente, accordée à la BIBLIOTHÈQUE NATIONALE DU CANADA de microfilmer cette thèse et de prêter ou de vendre des exemplaires du film.

L'auteur se réserve les autres droits de publication; ni la thèse ni de longs extraits de celle-ci ne doivent être imprimés ou autrement reproduits sans l'autorisation écrite de l'auteur.

Date

21 March 1983

Signature

Roger W. Toogood

NL-91 (4/77)

THE UNIVERSITY OF ALBERTA

Boundary Fitted Coordinate Systems For Estimation of Single and Multi-element Airfoil Force Coefficients, and Application to Wind Tunnel Corrections

by

(C) Roger W. Toogood

A THESIS

SUBMITTED TO THE FACULTY OF GRADUATE STUDIES AND RESEARCH

IN PARTIAL FULFILMENT OF THE REQUIREMENTS FOR THE DEGREE

OF Doctor of Philosophy

Department of Mechanical Engineering

EDMONTON, ALBERTA

Spring, 1983

THE UNIVERSITY OF ALBERTA

RELEASE FORM

NAME OF AUTHOR Roger W. Toogood

TITLE OF THESIS Boundary Fitted Coordinate Systems For Estimation of Single and Multi-element Airfoil Force Coefficients, and Application to Wind Tunnel Corrections

DEGREE FOR WHICH THESIS WAS PRESENTED Doctor of Philosophy

YEAR THIS DEGREE GRANTED Spring, 1983

Permission is hereby granted to THE UNIVERSITY OF ALBERTA LIBRARY to reproduce single copies of this thesis and to lend or sell such copies for private, scholarly or scientific research purposes only.

The author reserves other publication rights, and neither the thesis nor extensive extracts from it may be printed or otherwise reproduced without the author's written permission.

(SIGNED) Roger W. Toogood

PERMANENT ADDRESS:

10710 - 74 Ave.

Edmonton, Alberta

DATED 21 March 1983

THE UNIVERSITY OF ALBERTA

FACULTY OF GRADUATE STUDIES AND RESEARCH

The undersigned certify that they have read, and recommend to the Faculty of Graduate Studies and Research, for acceptance, a thesis entitled Boundary Fitted Coordinate Systems For Estimation of Single and Multi-element Airfoil Force Coefficients, and Application to Wind Tunnel Corrections submitted by Roger W. Toogood in partial fulfilment of the requirements for the degree of Doctor of Philosophy.

Supervisor

External Examiner

Date January 20, 1983

Abstract

Despite the advances in the theoretical analysis, the science of aerodynamics still relies heavily on the use of wind tunnels to provide design and performance data from test models. Such data must be corrected for the influence of the tunnel walls. For tests where the model is small in relation to the tunnel test section area the correction procedures are well-established and accurate. Modern aerodynamic research is often concerned, however, with test configurations where the model is quite large compared to the tunnel area, or develops very high lift. The latter category includes multi-component sections. For these geometries the standard correction forms become increasingly inadequate, and there are many difficulties with the interpretation of such experimentally obtained data.

A potential flow method for determining the wind tunnel corrections has been developed which contains explicitly the effect of the wall interference. Consideration was limited to the case of two-dimensional, incompressible flow in closed wind tunnels. There are no restrictions on model size or tunnel geometry. The method relies on a numerical solution for the stream function describing the complete flow field in the wind tunnel. The solution is obtained using finite difference techniques in a boundary fitted coordinate system. The coordinate system is generated

numerically, and allows an accurate and efficient solution for the potential flow. Several types of coordinate systems were investigated to determine the applicability of each to the wind tunnel problem. With suitable grids, the numerical solution for the entire flow field yields results which are comparable in accuracy to other potential flow analysis techniques.

The corrections are obtained by comparison of the aerodynamic force coefficients obtained using the numerical analysis with values obtained using a proven singularity method for the free flow field, that is, without the interference of the walls. The corrections so obtained represent the combined effect of lift interference and solid blockage, the coupling of which is essentially ignored by the standard correction forms.

Three airfoil sections of markedly different geometries and performance, including one two-element section, were tested in the University of Alberta low-speed wind tunnel. The tunnel size was made adjustable by using two large wall inserts, allowing a wide range of test geometries for each model. The numerically generated corrections were found to be accurate in reducing the measured data to a common set of data indicative of free field performance.

The procedure for obtaining the corrections is both expensive and time consuming, and requires major computing facilities. Therefore, no attempt was made to develop universal correction formulae, since the corrections appear

to be highly model dependent for these extreme geometries. However, the corrections are shown to be capable of substantially increasing the range of allowable test configurations for which reliable wall corrections can be made.

Acknowledgments

The author wishes to express his deep appreciation to Dr. D. J. Marsden for the opportunity to undertake this research, and for his patience and support throughout the course of the work.

The financial support of the Department of Mechanical Engineering and the Natural Sciences and Engineering Research Council of Canada is gratefully acknowledged.

The author would like to thank the members of his committee for their suggestions and encouragement. In particular, Dr. Masliyah is responsible for the author's interest in the use of boundary fitted coordinates, and numerical methods in general.

Special thanks are due to several individuals: Edward Cheng for his assistance with the wind tunnel tests, Ron Torgerson of the Department of Computing Services for his unfailing assistance in debugging the array processor, Gary Kovacik for his careful drafting of figures, and Helen Wosniak for efficiently and expertly typing the equations. The staff of the Mechanical Engineering shop are thanked for their aid in setting up the experiments.

The author would also like to thank the graduate students in the Department for keeping him on his toes.

Last, but definitely not least, the author wishes to thank his family and friends for providing sympathy and encouragement when nothing was working.

Table of Contents

Chapter		Page
I.	Introduction	1
II.	Wind Tunnel Corrections - Standard Forms	9
	A. Tunnel Blockage	17
	Solid blockage	18
	Wake Blockage	20
	B. Lift Interference	21
	C. Application of the Corrections	25
	D. Viscous Effects and Non-Linear Coupling	31
	E. Modern Methods	32
	F. Conclusion	33
III.	Theoretical Analysis of Tunnel Interference	35
	A. Grid Generation	42
	Grid Types	44
	Boundary Point Distribution	58
	Grid Control Functions	59
	B. Potential Flow Solution	67
	Evaluation of Velocities and Surface Pressures	72
	Kutta Condition Implementation	74
	Lift and Moment Calculations	79
	C. Numerical Implementation	84
	D. Data Interpretation	90
	E. Accuracy of BFC Solutions	99
	F. Conclusion	111
IV.	Experiments	112
	A. Test Equipment, Procedure, and Data Reduction	113

Tunnel Calibration 113
Models 115
Wall Inserts 119
Pressure Measurements - Transducers and Calibrations 120
Data Acquisition and Reduction 123
Free Field Drag Calculation 125
B. Free Field Results 125
C. High Blockage Results 129
D. Conclusion 148
V. Conclusion 149
References 153

List of Tables

Table		Page
1	Boundary Conditions for Single Element Potential Flow	69
2	Boundary Conditions for Two Element Potential Flow	71
3	Relaxation Parameters for Optimum Convergence	85
4	Comparison of Numerical Solution with Singularity Solution of Kennedy [13]	108

List of Figures

Figure		Page
1	Effect of Tunnel Walls on Measured Lift	12
2	Definition of Tunnel Geometry	14
3	Method of Images	16
4	Analytical Coordinate Transformation - Polar Coordinates	39
5	O-Type Grid - General Form	45
6	C-Type Grid - General Form	47
7	S-Type Grid - General Form	48
8	2S-Type Grid - General Form	50
9	O-Type Grid - Wind Tunnel Geometry	52
10	C-Type Grid - Wind Tunnel Geometry	53
11	C-Type Grid - Tunnel Contraction Geometry	54
12	S-Type Grid - Wind Tunnel Geometry	56
13	2S-Type Grid - Wind Tunnel Geometry	57
14	Airfoil Boundary Point Distribution	60
15	Grid Control - O-Type Grid with Q Control	63
16	Grid Control - S-Type Grid with P Control	64
17	2S-Type Grid - Airfoil Detail - No Grid Control	65
18	2S-Type Grid - Airfoil Detail - Strong P and Q Grid Control	66
19	Trailing Edge Points For Velocity Kutta Condition	77
20	Airfoil Force System	80
21	Effect of Relaxation Parameter on Convergence Rates for an O-Type Grid	86
22	Determination of Optimum Relaxation Parameter for an O-Type Grid	87

Figure		Page
23	S-Type Grid Alpha Surface Plot	93
24	S-Type Grid Beta Surface Plot	94
25	S-Type Grid Gamma Surface Plot	95
26	S-Type Grid Jacobian Surface Plot	96
27	S-Type Grid Orthogonality Surface Plot	97
28	S-Type Grid Aspect Ratio Surface Plot	98
29	Stream Function Contours - Uniform Stream at Zero Degrees (No Circulation)	100
30	Stream Function Contours - Uniform Stream at Ninety Degrees (No Circulation)	101
31	Stream Function Contours - Circulatory Flow	102
32	Stream Function Contours - Total Flow at 20 Degrees Incidence	103
33	Pressure Coefficient Contours through a Contraction Using a C-Type Grid	104
34	O-Type Grid Trailing Edge Details	106
35	Comparison of S-Type Solution With Singularity Solution for a Wind Tunnel Geometry	110
36	Profiles of Models Tested	117
37	Tunnel Geometry for Free Field Tests	121
38	Tunnel Geometry for Blockage Tests	122
39	Data Acquisition Schematic	124
40	Model #1 - Free Field Lift and Moment Coefficients	126
41	Model #2 - Free Field Lift and Moment Coefficients	127
42	Model #3 - Free Field Lift and Moment Coefficients	128
43	Contributions of Corrections - Model #1, Free Field	130

Figure Page

44 Contributions of Corrections - Model #2, Free Field 131

45 Contributions of Corrections - Model #3, Free Field 132

46 Model #1 - Effect of Wall Position on Uncorrected Data 133

47 Model #2 - Effect of Wall Position on Uncorrected Data 134

48 Model #3 - Effect of Wall Position on Uncorrected Data 135

49 Model #1 - High Blockage Results (Standard Corrections) 137

50 Model #2 - High Blockage Results (Standard Corrections) 138

51 Model #3 - High Blockage Results (Standard Corrections) 139

52 Model #1 - Correction Table 140

53 Model #2 - Correction Table 141

54 Model #3 - Correction Table 142

55 Spline Interpolation Scheme for Correction Tables 143

56 Model #1 - High Blockage Results Using Correction Table 145

57 Model #2 - High Blockage Results Using Correction Table 146

58 Model #3 - High Blockage Results Using Correction Table 147

List of Symbols

A	airfoil cross section area
a	grid aspect ratio
$\bar{b}$	unit vector on trailing edge bisector
c	airfoil chord (=1)
d	model distance from tunnel lower wall
h	tunnel height
$\bar{i}, \bar{j}$	Cartesian unit vectors
J	Jacobian of coordinate transformation
P	grid control function
Q	grid control function
q	wind tunnel dynamic pressure,
Re	Reynolds number
t	airfoil maximum thickness
u,v	Cartesian velocity components
V	tunnel free stream velocity
$\bar{V}$	velocity vector
W	over-relaxation parameter in numerical solution
x,y	Cartesian coordinates
x_r	model rotation point from leading edge
y	model maximum camber

Aerodynamic Force Coefficients

C_d	drag coefficient
C_ℓ	lift coefficient

C_m	quarter-chord pitching moment coefficient
$C_{M_{LE}}$	leading edge pitching moment coefficient
C_N	force coefficient normal to chord line
C_X	force coefficient parallel to chord line
C_r	resultant force coefficient
C_p	pressure coefficient

Greek Letters

α, β, γ	coordinate transformation metrics
β_F	flap angle
Γ	circulation
δ	transformed coordinate mesh orientation
Δ	increment
ε	total velocity increment due to blockage
ε_s	velocity increment due to solid blockage
ε_w	velocity increment due to wake blockage
θ	section angle of attack
θ	transformed coordinate orthogonality
λ	Kutta condition parameter, single element section
λ_1, λ_2	Kutta condition parameters, two element section
ξ, η	transformed coordinates
σ	tunnel interference correction parameter
ϕ	circular coordinate of airfoil section
ψ	stream function

Subscripts

$\mathfrak{L}$	tunnel centre-line
a	aft of section maximum thickness
f	foreward of section maximum thickness
l	lower surface
u	upper surface
F	free field value
T	measured, test value

Superscripts on ψ

1	uniform stream parallel to chord, zero circulation
2	uniform stream perpendicular to chord, zero circulation
3	unit circulation about main section, zero onset flow
4	unit circulation about flap section, zero onset flow
T	total stream function

I. Introduction

The science of aerodynamics, and its utilization in practical aviation, has advanced rapidly since the introduction of the boundary layer theory in 1904. This major step in the theoretical analysis allowed the division of the fluid flow field into two distinct regions: the thin boundary layer near solid surfaces where viscous effects could not be neglected, and the external inviscid flow which could be analyzed using the established procedures of classical hydrodynamics. However, the theoretical analysis of real fluid flows still could not accurately provide all the necessary data for aerodynamic design purposes, and knowledge of the real flow behaviour could be gained only by experimental observation. To a large extent, the need for experimental studies still remains, although the development of the various mathematical techniques has allowed a large reduction in the required experimental effort. In the last three decades, an explosive growth in the use of the computer for solving flow problems has occurred.

Using mathematical procedures developed much earlier but impractical at the time and by devising new methods, theoreticians can now model many real fluid flows with reasonable accuracy. The theory and application of numerical analysis techniques for problems in fluid flow has come to be called computational fluid dynamics. Computational

methods presently form a large portion of basic research in aerodynamics. Coupled with the ever-increasing capability of modern digital machines, this effort has both improved the accuracy and increased the efficiency of numerical solutions, and allowed application to a wider range of flow problems. Such numerical investigations, in what have been termed electronic wind tunnels, can provide quick solutions to analysis problems in which dozens of parameters are involved, making it possible to quickly modify and optimize a design to meet particular goals.

However, numerical methods are subject to sometimes very severe restrictions, either in a mathematical sense or a practical one. The physics of fluid motion is very complex, and there are no adequate mathematical models which will handle the general problems of aerodynamics. Often these numerical simulations can be accomplished only by making severe assumptions about the flow field. There are many physical phenomena (turbulent flow, separated, and three dimensional flows, to name a few) for which universal and adequate models do not yet exist or cannot be practically implemented due to the limited capacity of digital hardware. It is often these phenomena which are the most important features of the flow and until totally adequate numerical models and techniques are developed the need for experimental investigation will persist.

The Wright brothers relied on aerodynamic data obtained in their own wind tunnel, and there are few aircraft

companies today which will proceed with a major project without very careful experimental verification of designs. The major tool of these investigations is the wind tunnel, which allows precise control over the environment in which an aerodynamic model is tested. The validity of the wind tunnel tests is assured, i.e. the behaviour of the full scale design may be extrapolated with confidence from model tests, if certain conditions are satisfied. When the model shape is scaled accurately, these requirements are met by matching the Reynolds number and Mach number of the test with the full scale situation. This is the well known concept of dynamic similarity.

Besides the attainment of dynamic similarity, the wind tunnel and its operation must be thoroughly understood if the data it provides are to be interpreted correctly. This is complicated by the wide variety of tunnel configurations and sizes, and the diverse nature of the experimental tests which might be performed. Furthermore, the wind tunnel does not provide a free flow field in which the test will be carried out. Only rarely are tests carried out for bounded flows, such as testing for ground effect of aircraft or air cushion vehicles. The fact that the wind tunnel flow field is bounded can affect the data as much as variations in Reynolds or Mach number. These boundary constraints on the flow must be clearly understood, and their effects carefully assessed.

There are two approaches to the problem of boundary constraint or tunnel wall interference. Usually, the effect of the boundaries is compensated by making corrections to the measured data. These standardized corrections are found either empirically or using simple mathematical theories, based on several assumptions about the tunnel geometry. The second approach, the subject of much recent research, is the design of tunnels and test geometries which are interference free. This may be done by varying the shape of the tunnel walls or providing semi-open walls, so that the interference is minimized or totally eliminated. Such modifications would need to be based on very large and expensive research efforts in their own right. The prospects for modification to an interference-free configuration seem minimal, assuming such modifications could be physically accommodated, if the tunnel is to host a wide range of test geometries.

Much recent research has been directed towards high lift systems operating at low Mach numbers and high Reynolds numbers, such as occur during take-off and landing of large aircraft. To obtain the large Reynolds numbers, ever larger models are being tested which press to the limit the applicability of the standard correction techniques. Very little high speed work is done with large models. For these tests, the Mach number is of primary importance, with the Reynolds number assuming a secondary role. Because of power demands, tests where compressibility is important are therefore usually carried out using small models in special

ventilated tunnels.

The aim of the present work is to investigate the use of certain numerical techniques in extending the range of applicability of the standard method of applying boundary corrections for non-standard geometries and high lift sections. Although in principle the numerical technique developed could be extended to three dimensional flows and open tunnels, consideration will be limited to the case of two dimensional flow in closed jet tunnels with fixed walls. There are several motivations for this. First, the vast majority of wind tunnels operating today are of this type, and high lift research is primarily concerned with the flow past the two dimensional wing section profile. Second, the existing methods for obtaining wall corrections are valid only for a limited range of test geometries which will be detailed in the next chapter. Finally, the investigation of new and advanced numerical procedures in aerodynamic research will help to determine the applicability of such methods. Wind tunnel testing can become very expensive and time consuming and although computational methods will not likely replace the wind tunnel, they will undoubtedly continue to assume a larger share of the work load. It is worthwhile therefore to explore the use of these numerical techniques, to identify useful applications and areas for improvement.

As pointed out by Garner in [1], there is a need for improved understanding of the wall interference effects when

the model is large in relation to the tunnel cross section and/or develops high lift. In these cases, the problem becomes non-linear and the various wall effects interact. Garner suggests that ([1], p.15) "a convincing theory of wall interference on high lift systems may require an improved mathematical model" and that ([1], p.14) "the most promising method of solution may well be one of numerical analysis by a finite-difference technique." The coupled effects of the tunnel walls may then be calculated simultaneously.

The present work is an investigation of just such a solution scheme. By eliminating many of the underlying assumptions used to develop the standard correction schemes, the analysis results in corrections which are applicable to a much wider range of test situations. In the case of multi-element and high lift sections, the present analysis offers an accurate and intuitively correct interpretation of the wall interference corrections.

The theoretical analysis is accomplished using a finite difference solution for the stream function which describes the tunnel flow. The solution for a given test geometry is carried out in a numerically generated boundary fitted coordinate system. This coordinate system offers the advantage of placing computational nodes exactly on the flow boundaries and distributing the nodes in a rational manner throughout the field. This technique alleviates the difficulty of performing finite difference solutions on

fields with irregular boundaries. For the present work, several grid topologies were investigated, to determine the applicability of each grid type to the given flow problem. Each grid topology offered certain advantages to the present solutions. By carefully controlling the nature of the computational grid in the physical plane, adequate theoretical results were attainable. These results lead directly to the estimation of the corrections necessary to account for the interference of the walls during the wind tunnel tests.

In the following chapters the material is organized as follows. Chapter II reviews the existing theories for wind tunnel boundary corrections. The need for a more general theory will be pointed out. The following chapter describes the theoretical approach developed to handle arbitrary test configurations. By comparing solutions for the bounded wind tunnel flow with those for a free field flow, the interference of the walls may be assessed, and suitable corrections devised for each tunnel geometry. Chapter IV describes some experiments carried out in the University of Alberta low speed wind tunnel to demonstrate the applicability and accuracy of the proposed corrections, with a comparison with standard forms, for a wide range of test configurations.

The results indicate that the present method can generally provide better corrections than the standard methods for the extreme geometries tested. Thus, the

permissible range of geometries for which reliable corrections are available has been extended. The method applies equally well to multi-element and high lift sections, which are not adequately treated by the standard corrections.

II. Wind Tunnel Corrections - Standard Forms

Experimental investigations in wind tunnels are usually directed towards the measurement of the net forces and moments exerted on the model by the moving stream. This data is to be applied to the estimation of the full scale performance which occurs in the free air of the atmosphere. There are two fundamental concerns associated with the generation of reliable wind tunnel test data. The first is the attainment of dynamic similarity, i.e. matching the Reynolds and Mach numbers, which ensures that the wind tunnel flow corresponds geometrically and dynamically with the full scale flow. The second concerns the estimation of the effect of the tunnel boundaries on the flow surrounding the model, specifically the effect on the measured aerodynamic forces and moments. The nature of these effects depends upon whether the tunnel is of the open jet type, or constrains the flow between rigid walls. (There are numerous other experimental considerations, such as free stream turbulence and non-uniformity, growth of wall boundary layers, and the presence of measuring gear in the test section, which will not be examined here.)

The boundary effects are usually obtained as small incremental corrections which must be applied to the measured data such that the corrected data is indicative of the free field performance. These incremental adjustments

depend upon the geometry of the wind tunnel and model, primarily the chord-to-height ratio. For usual geometries the corrections may be 5% to 10% of the measured values. Various theoretical approaches, which will be discussed shortly, have been developed for the estimation of these corrections.

The methods to be treated here are concerned with two dimensional testing in tunnels with closed walls. Very little two-dimensional testing is done in open tunnels because the flow is often far from two-dimensional due to end effects. However, the open-wall corrections are of the opposite sign to the closed-wall corrections, which raises the possibility of providing semi-open walls where the corrections should cancel. Such a configuration was developed by Williams and Parkinson [2], who obtained a zero correction tunnel using a slotted upper wall with an open area ratio of 0.7. With the slotted wall extending from two to six chord lengths upstream and downstream from the model, application of this method seems limited for large tunnels due to physical constraints.

Other zero interference tunnels have been described by Goodyer [3] and by Vidal, Erickson, and Catlin [4]. The self-streamlining tunnel of Goodyer utilizes flexible upper and lower walls, which are automatically positioned during the test to simulate streamlines in a free flow field. This technique does not appear to be applicable to large tunnels, again because of the extent of the required modifications.

The self-correcting tunnel of Vidal, et al., utilizes large regions of suction and/or blowing through porous walls, the result being the duplication of the free field streamline pattern at the model. This method was developed for transonic flow, where interference of the wall with the shock waves is critical, and may be impractical for large tunnels due to power demands.

Figure 1 represents diagramatically the situation which occurs in a closed tunnel with straight walls, where the measured lift coefficient C_{ℓ_T} at the test angle of attack θ_T is compared to the free field data. It is seen that the measured lift is too high, the measured incidence is too low, or both. The measured drag and pitching moment are also larger than free field values. The three lines I, II, and III, represent three possible correction strategies to obtain proper free air lift coefficients, C_{ℓ_F} at θ_F , C'_{ℓ_F} at θ'_F , etc. These strategies will be discussed at length in a later section. For the present, it is necessary to identify the sources of the experimental deviations.

Theoretically, the need for the tunnel wall corrections may be deduced from the fact that although the governing flow equations are the same for the flow in the tunnel and in free air, the outer boundary conditions on the flow field are different. In free air, the streamlines far from the airfoil are able to curve freely, whereas in the tunnel, the flow is constrained between straight rigid walls. For subsonic, steady flow the governing equations are elliptic

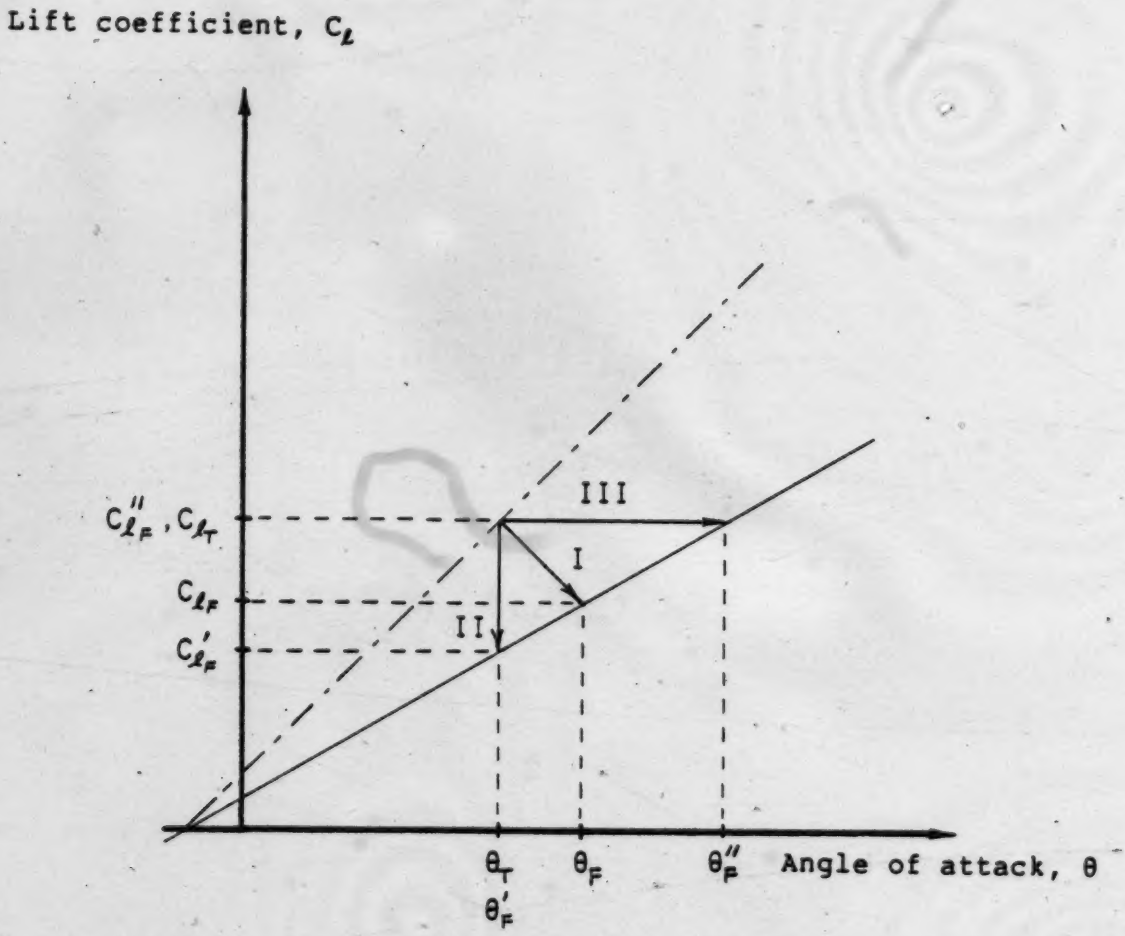

Figure 1 Effect of Tunnel Walls on Measured Lift

and the boundary conditions have a major effect on the flow solution, and hence, on the aerodynamic forces on the model.

The increments in the force coefficients caused by wall interference, hence the corrections required to the experimental data, may be attributed to two major effects. These are described in Pope and Harper [5] and, in greater detail, in Garner, Rogers, Acum and Maskell [1]. Of primary importance to two dimensional testing in closed tunnels are the corrections required to account for the interference due to the blockage of the tunnel by the model and its wake, and to the constraining effect of the straight walls on the curvature of the flow around the model. The geometric parameters which govern these corrections are defined in Figure 2. These may be grouped into the non-dimensional terms representing the chord-to-height ratio (c/h), model position (d/h), and model rotation point (x_r /c). Along with the angle of attack θ_T (and the flap angle β_f for two element sections), these determine the basic tunnel geometry. The profile of the model itself may be described in rough terms by the thickness-to-chord ratio (t/c), cross-sectional area (A), and the camber ratio (y/c).

Early work on the theory of tunnel corrections, being analytical in nature, was possible only by restricting the consideration to the case of small, thin models at low angle of attack whose mid-chord was on the tunnel centre-line. The tunnel was also assumed to extend infinitely far upstream and downstream from the model. Later theories included

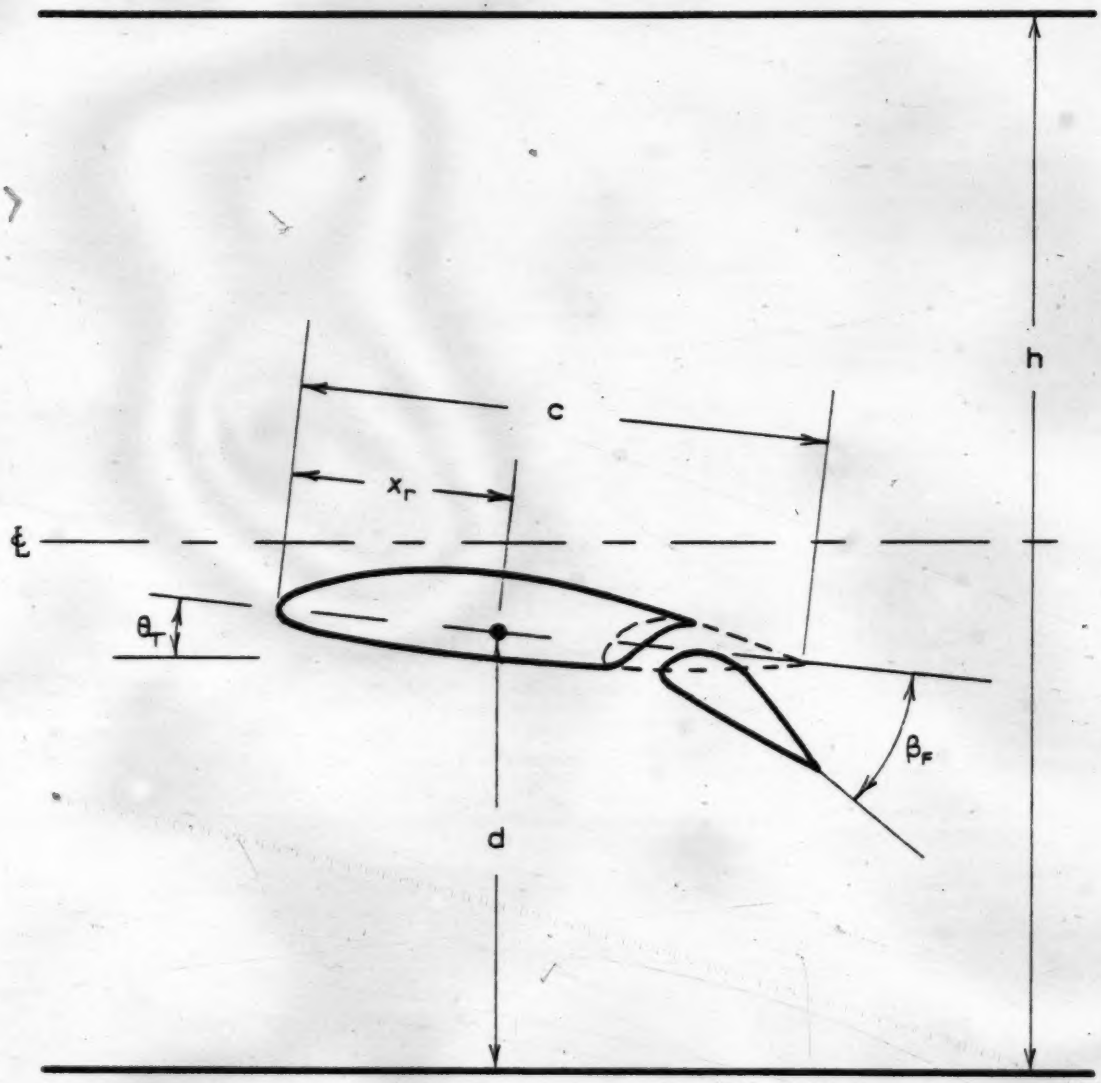

Figure 2 Definition of Tunnel Geometry

special cases for off-center model locations, and consideration of the effects of thickness and larger c/h ratios.

For incompressible unseparated flow, the wall effect may be analysed using potential flow techniques, by ignoring the effects of viscosity. Historically, the most important of these is the method of images, Figure 3, where the influence of the walls is calculated from the flow field induced at the model by the infinite set of mirror images above and below the tunnel (only the first images are shown). Of necessity these early analyses were limited to single airfoils, and mathematically soluble only by making the assumptions described previously.

Extensions to these early theories have been developed to account for higher order corrections for larger models, as described below. These methods have been used for test cases at moderate chord-to-height ratios, but due to numerical complexity are not in common use.

In arriving at corrections using the method of images, the implicit assumption was made that the tunnel blockage and streamline curvature effects were independent. Thus, since the governing flow equation is linear, the blockage and curvature effects could be analysed separately, using image systems composed of either doublets or vortices. More advanced image theories used continuous source-sink or vorticity distributions. In either case, the combined wall effect was obtained by superposition. Following this

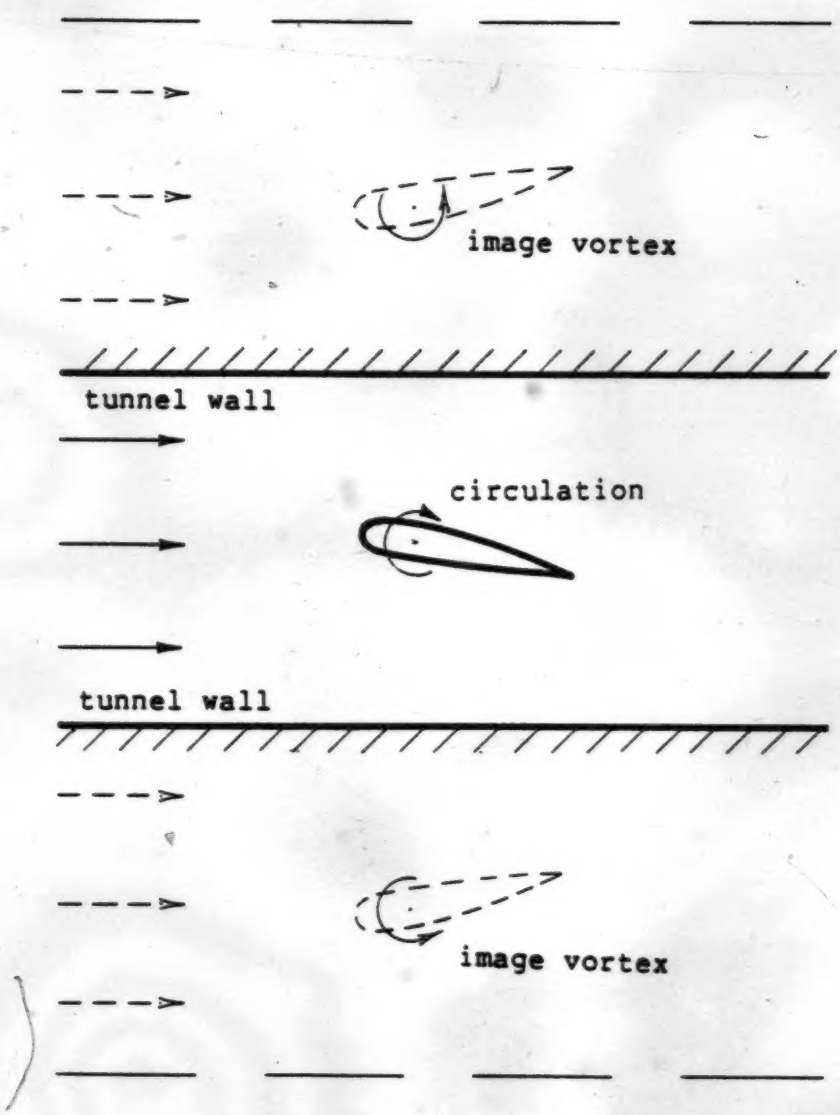

Figure 3 Method of Images

procedure, the wall effects will be discussed separately, although it develops (section D) that the corrections are not independent except under special circumstances. In the discussion which follows, the subscripts "T" and "F" refer to measured test values and corrected free field values, respectively.

A. Tunnel Blockage

Tunnel blockage corrections arise from the volume occupied by the model and its wake in the tunnel. The model reduces the cross-sectional area of the tunnel, and since the flow is incompressible, the effective free stream velocity at the model is increased slightly above the tunnel speed measured far upstream. The required correction to the tunnel velocity is usually divided into independent solid and wake blockage components, where the former refers to the physical size of the model and the latter relates to the displacement thickness of the airfoil boundary layers and wake, and hence is related to the airfoil drag. The ratio of the total velocity increment to the free stream velocity is represented by

$$\varepsilon = \frac{\Delta V}{V} = \varepsilon_s + \varepsilon_w \qquad (1)$$

where ε_s and ε_w are the solid and wake blockage velocity increments, respectively.

Solid blockage

The solid blockage component ε_s depends on the model chord, maximum thickness, and thickness distribution, and is considered to be independent of camber and lift. Thus, the determination of ε_s is based on consideration of the section thickness distribution obtained with the camber removed, and mounted at zero incidence. Early analyses were also based on the assumption that only the longitudinal flow was affected, which is only true if the model is mounted on the tunnel center line. This early work is well documented in Garner, et al. [1]. Briefly, these solid blockage corrections were developed as follows:

1. Lock (1929) represented the airfoil and images by doublets. The blockage factor obtained was given by the formula

$$\varepsilon_s = \frac{\pi^2}{12} \lambda_2 \left(\frac{c}{h}\right)^2 \left(\frac{t}{c}\right)^2 \qquad (2)$$

where λ_2, the body-shape factor, is a function of the thickness distribution, values of which are tabulated for various sections.

2. Goldstein [6], using a series solution technique, developed a formula accurate for higher c/h ratios. This formula was later re-arranged by Allen and Vincenti [7] to the form

$$\varepsilon_s = \frac{\pi A}{6h^2} + \frac{\pi^3}{960}\frac{c}{h}\int_0^{\pi} y(x)\,\frac{\cos 4\phi}{\sin\phi}\,d\phi \qquad (3)$$

where A is the cross sectional area of the profile, and (x,y) are the coordinates of the thickness distribution. The variable ϕ is given by the function

$$x = \frac{1}{2}(1 - \cos\phi)$$

3. Thom (1943) replaced the doublet of Lock by a distribution of sources and sinks on the chord line to obtain the formula (for thin sections)

$$\varepsilon_s = \frac{\pi A}{6h^2} = 0.52\,\frac{A}{h^2} \qquad (4)$$

4. Young and Squire (1945) proposed that the formula of Thom could be improved for thicker sections using

$$\varepsilon_s = 0.62\,\frac{A}{h^2} \qquad (5)$$

5. Thompson (1948) proposed a different improvement to Thom's relation by including a term which depended explicity on the model thickness, making the formula valid up to t/c=0.2, as follows,

$$\varepsilon_s = \frac{\pi}{6}\left[1 + 1.2\,\frac{t}{c}\right]\,\frac{A}{h^2} \qquad (6)$$

More complex expressions were developed to account for streamwise variations in blockage, Woods (1954), and for variations due to angle of attack and off-center model position, Batchelor (1944). The latter correction is

$$\varepsilon_s(d) = \varepsilon_{s_\ell} \left[1 + \frac{3}{4} \cot^2 \pi \frac{d}{h} \right] \tag{7}$$

For small models at low lift coefficients these corrections have been proven to be accurate in numerous experimental tests. Allen and Vincenti [7] showed the accuracy of the Goldstein corrections up to c/h=0.4 at low Mach numbers.

Thus, for the cases of large models, high lift coefficients, or off-center mounting position, the above corrections, which become quite large, are questionable. In these cases, such effects as the chordwise variation in the longitudinal velocity increment and induced transverse velocities must be considered. These will interact with the corrections to lift and incidence described in a later section.

Wake Blockage

The blockage effect of the wake behind the model is obtained by representation of the wake by a source at the section trailing edge and a sink far downstream. The velocity increment at the model due to the source-sink image system may then be related to the original source strength,

and ultimately to the airfoil drag coefficient. Using this approach, the wake blockage increment

$$\varepsilon_w = \frac{1}{4}\frac{c}{h} C_{d_T} \tag{8}$$

has been developed by several authors, for example Allen and Vincenti [7]. Goldstein [6] showed in addition that the resulting correction is valid when the drag is small even if the chord to height ratio is large. The wake blockage increment is much smaller than the solid blockage increment as long as the drag remains small, i.e. the flow remains attached to the airfoil surface. For the present work, which utilizes inviscid theory and therefore restricts consideration to unseparated flow, the above wake blockage formula will be assumed to be adequate.

B. Lift Interference

The presence of the walls constrains the natural curvature of the flow around a lift-producing airfoil. The resulting corrections to the stream direction and curvature are known as lift interference corrections since they arise solely from the lift or circulation generated by the model. The effect of the interference is to increase the effective camber and incidence of the model, while there is no effect on the longitudinal velocity if the model is mounted on the tunnel center-line. To a first approximation, the lift interference is independent of the model thickness, and so

can be analysed independently of the blockage. However, it is important even for small models, vanishing only at zero lift.

The methods of analysis detailed below ignore the model thickness and place either the mid-chord or the aerodynamic centre on the tunnel center-line. The model is represented by a single vortex or continuously distributed vorticity along the chord line and the effect of the walls is deduced using the method of images. The primary effects of the image system are treated as an induced upwash and an induced flow curvature. The upwash is evaluated at the model mid-chord and treated as an incidence correction. The flow curvature produces a change in effective camber or loading and yields the required correction to the section lift and pitching moment.

A complete discussion of lift interference appears in Garner, et al. [1], highlights of which appear below. The theories are classed as first or second order, depending on the terms retained in the final expressions for the corrections. The second order theories are generally preferred when the c/h ratio becomes large. Briefly, the development of the lift interference theories has occurred as follows:

1. Glauert (1933) considered small, thin airfoils at small incidence. In developing this first order theory, the airfoil was represented by a single vortex at the centre of pressure giving the induced upwash angle at position

x on the chord line as

$$\Delta\theta = \frac{\pi}{16}\left(\frac{c}{h}\right)^2 \left[\left(\frac{x}{c} - \frac{1}{4}\right) + \frac{C_{m_T}}{C_{\ell_T}}\right]\left[\frac{2}{3} + \cot^2\pi\,\frac{d}{h}\right] C_{\ell_T} \qquad (9)$$

This is one of the few theories which consider off-center models, the effect of which is shown by the last term. This arises from an induced longitudinal velocity component which vanishes when d=h/2.

2. Tomotika (1938) used a conformal transformation method to analyse a flat plate mounted on the tunnel center-line, obtaining variations in lift and moment with angle of attack for various chord-to-height ratios.

3. Allen and Vincenti [7] devised a first order correction for thin airfoils by replacing the model with a continuous vorticity distribution on the chord line. The upwash at the mid-chord induced by the image system is given by

$$\Delta\theta = \frac{\pi}{96}\left(\frac{c}{h}\right)^2 \left[1 + 4\,\frac{C_{m_T}}{C_{\ell_T}}\right] C_{\ell_T} \qquad (10a)$$

This agrees with the expression of Glauert, equation (9), evaluated at x/c=.5 and d/h=.5. The induced curvature results in lift and moment corrections

$$\Delta C_\ell = -\frac{\pi^2}{48}\left(\frac{c}{h}\right)^2 C_{\ell_T} \qquad (10b)$$

$$\Delta C_m = \frac{\pi^2}{192}\left(\frac{c}{h}\right)^2 C_{\ell_T} \qquad (10c)$$

With these corrections the new lift and moment

coefficients relate to the unconfined flow at the corrected incidence $\theta_T + \Delta\theta$. Comparison of these results with Tomotika's results showed large discrepancies for c/h>0.4, indicating the need for higher order corrections for these geometries.

4. Havelock (1938) considered a flat plate whose mid-point was an arbitrary distance from the tunnel floor, and neglected terms of order greater than $(c/h)^4$ to obtain a second order method. Havelock showed that even for small c/h, the effect of incidence and higher terms in c/h can be of primary importance when the model is off the center-line. Moreover, the downward displacement of the model at positive incidence can change the sign of the correction due to the induced longitudinal velocity, which can no longer be ignored.

5. Goldstein [6] approached the general problem of the thick cambered section using power series in (c/h). The derived second order corrections, valid only when the model is on the center-line, are as follows:

$$\Delta\theta = \left[\frac{\pi^2}{96}\left(\frac{c}{h}\right)^2 - \frac{41\pi^3}{92160}\left(\frac{c}{h}\right)^4\right] C_{\ell_T} \qquad (11a)$$

$$\Delta C_\ell = \left[-\frac{\pi^2}{48}\left(\frac{c}{h}\right)^2 + \frac{7\pi^4}{3072}\left(\frac{c}{h}\right)^4\right] C_{\ell_T} \qquad (11b)$$

$$\Delta C_m = \left[\frac{\pi^2}{192}\left(\frac{c}{h}\right)^2 - \frac{7\pi^4}{15360}\left(\frac{c}{h}\right)^4\right] C_{\ell_T} \qquad (11c)$$

Goldstein showed that for c/h>0.3 the terms in $(c/h)^4$,

which reduce the magnitude of the correction, cannot be ignored. Goldstein also solved the problem of the off-center model using power series, but it suffers from very slow convergence.

6. Moses [9] derived a conformal transformation technique to calculate the velocity distributions on an arbitrary airfoil located anywhere within the tunnel, although providing results only for the center-line position. Results were similar to Goldstein's method, and in the opinion of Garner, easier to obtain. Also according to Garner, the Moses analysis showed that if terms in $(c/h)^4$ are neglected, the corrected lift curve slope is too low, while if the thickness is neglected, the slope is too high, by a few per cent.

As with the solid blockage corrections, there have been numerous experimental verifications of the above lift interference corrections. Knechtel [8] showed the accuracy of the first order correction of Allen and Vincenti for low Mach numbers so long as the c/h ratio was less than 0.4. For incompressible flow, the second order correction of Goldstein is preferred when the c/h ratio is large.

C. Application of the Corrections

Assuming that the blockage and lift interference corrections are independent, they may be applied separately to the measured wind tunnel data. The blockage correction

results in a change in the tunnel velocity at the model. Thus, the tunnel speed is corrected by

$$V_F = V_T (1 + \varepsilon)$$

where V_T is the tunnel speed measured far upstream, or at least obtained without interference from the model. The dynamic pressure is therefore corrected using

$$q_F = q_T (1 + \varepsilon)^2$$

The measured aerodynamic force coefficients are corrected for blockage using the corrected dynamic pressure:

$$C_F = C_T \cdot \frac{q_T}{q_F} = C_T \cdot \frac{1}{(1+\varepsilon)^2}$$

and if higher order terms in ε are neglected, these corrections become

$$C_{\ell_F} = C_{\ell_T} (1 - 2\varepsilon) \qquad (12a)$$

$$C_{m_F} = C_{m_T} (1 - 2\varepsilon) \qquad (12b)$$

The correction due to the lift interference involves one of the three strategies shown in Figure 1. The usual strategy is to correct both the incidence and the lift coefficient, line I, using either equations (10) or (11). Thus, with σ defined by

$$\sigma = \frac{\pi^2}{48} \left(\frac{c}{h}\right)^2$$

the first order corrections of Allen and Vincenti, equations (10) are

$$\Delta\theta = \frac{\sigma}{2\pi}\left(1 + 4\frac{C_{m_T}}{C_{\ell_T}}\right) C_{\ell_T} \tag{13a}$$

$$\Delta C_\ell = -\sigma C_{\ell_T} \tag{13b}$$

$$\Delta C_m = \frac{\sigma}{4} C_{\ell_T} \tag{13c}$$

and the second order corrections of Goldstein, equations (11), become

$$\Delta\theta = \frac{\sigma}{2\pi}\left(\left[1 - \frac{21}{20}\sigma\right] + 4\frac{C_{m_T}}{C_{\ell_T}}\right) C_{\ell_T} \tag{14a}$$

$$\Delta C_\ell = -\left(1 - \frac{21}{4}\sigma\right)\sigma C_{\ell_T} \tag{14b}$$

$$\Delta C_m = \left(1 - \frac{21}{5}\sigma\right)\frac{\sigma}{4} C_{\ell_T} \tag{14c}$$

The total corrections are finally obtained by adding the contributions due to blockage and lift interference. Thus, the complete first order corrections become

$$\theta_F = \theta_T + \frac{\sigma}{2\pi}\left(1 + 4\frac{C_{m_T}}{C_{\ell_T}}\right) C_{\ell_T} \tag{15a}$$

$$C_{\ell_F} = \left[1 - \sigma - 2\varepsilon\right] C_{\ell_T} \tag{15b}$$

$$C_{m_F} = \left[1 - 2\varepsilon\right] C_{m_T} + \frac{\sigma}{4} C_{\ell_T} \tag{15c}$$

These are the corrections given in Pope and Harper [5], who

unfortunately do not stress the limitations of their use.

If the model is off the center-line, the corrected incidence at the mid-chord position becomes, using equation (9),

$$\theta_F = \theta_T + \frac{3\sigma}{4\pi}\left[\frac{2}{3} + \cot^2\pi\frac{d}{h}\right]\left(1 + 4\frac{C_{m_T}}{C_{\ell_T}}\right)C_{\ell_T} \qquad (16)$$

Similar expressions may be developed for the second order corrections.

The two correction strategies indicated by lines II and III in Figure 1 represent corrections at constant incidence and constant lift, respectively, as given by Pankhurst and Holder [10]. Both of these strategies require knowledge (or assumption) of the free field lift curve slope $\frac{\partial C_{\ell_F}}{\partial \theta_F}$ approximately equal to 2π for thin airfoils.

For the correction at constant incidence, line II, the lift correction is augmented by an additional increment $\left(C_{\ell_F} - C'_{\ell_F}\right)$ corresponding to the induced upwash angle. Thus, referring to Figure 1,

$$\theta'_F = \theta_T \qquad (17a)$$

$$C'_{\ell_F} = C_{\ell_F} - \frac{\partial C_{\ell_F}}{\partial \theta_F} \cdot \Delta\theta \qquad (17b)$$

The correction at constant lift, line III, is accomplished similarly by treating the lift increment due to the camber effect as an additional incidence correction, thus,

$$\theta_F'' = \theta_F - \left(\frac{\partial C_{\ell_F}}{\partial \theta_F} \right)^{-1} \cdot \Delta C_\ell \qquad (18a)$$

$$C_{\ell_F}'' = C_{\ell_T} \qquad (18b)$$

Theoretically, for both these strategies, the pitching moment and drag coefficients should be adjusted accordingly, using $\frac{\partial C_{m_F}}{\partial \theta_F}$ and $\frac{\partial C_{d_F}}{\partial \theta_F}$. For attached flow however, these derivatives are usually very small and the corresponding additional increments are ignored. For either strategy, then, the corrected pitching moment and drag coefficients are

$$C_{m_F} = C'_{m_F} = C''_{m_F} \qquad (19a)$$

$$C_{d_F} = C'_{d_F} = C''_{d_F} \qquad (19b)$$

The constant incidence strategy will be used for the application of corrections in the experimental work described in Chapter IV as this allows easier comparison with the theoretical results of Chapter III. This affects only the lift interference, as the blockage corrections are assumed, in the above analyses, to be independent of lift and incidence. These corrections result in the following expressions (to first order)

$$\Delta\theta = \theta'_F - \theta_T \equiv 0 \tag{20a}$$

$$\Delta C_\ell = - \left(1 + \frac{1}{2\pi} \left[1 + 4 \frac{C_{m_T}}{C_{\ell_T}} \right] \frac{\partial C_{\ell_F}}{\partial \theta_F} \right) \sigma C_{\ell_T} \tag{20b}$$

$$\Delta C_m = \frac{\sigma}{4} C_{\ell_T} \tag{20c}$$

The second order corrections take the form

$$\Delta\theta = \theta'_F - \theta_T \equiv 0 \tag{21a}$$

$$\Delta C_\ell = - \left((1 - \frac{21}{4}\sigma) + \frac{1}{2\pi} \frac{\partial C_{\ell_F}}{\partial \theta_F} \left[(1 - \frac{21}{20}\sigma) + 4 \frac{C_{m_T}}{C_{\ell_T}} \right] \right) \sigma C_{\ell_T} \tag{21b}$$

$$\Delta C_m = \left[1 - \frac{21}{5}\sigma \right] \frac{\sigma}{4} C_{\ell_T} \tag{21c}$$

For thicker sections, and for multi-element sections, the theoretical inviscid lift curve slope is larger by a small fraction than the thin airfoil value of 2π (per radian). The actual lift curve slope obtained experimentally is slightly less owing to viscous effects, and is therefore also affected by the Reynolds number. For moderately thick single element sections the effects of thickness and viscosity roughly balance, so that the real lift curve slope is near the value 2π . For very thick and/or multi-element sections, however, the situation is not so clear. Experimental values much higher than 2π have been reported: Wentz [11] measured a slope of $1.29*2\pi$ for the NASA section GA(W)-1 with a 30% Fowler flap at 20° deflection. Foster,

Irwin, and Williams [12] measured $1.09*2\pi$ for a section with a 40% slotted flap at 30° deflection. The inviscid two element analysis of Kennedy [13] calculates a slope of $1.25*2\pi$ for the slotted flap section used in the present experimental work. Unfortunately, the real lift curve slope for thick or multi-element sections cannot be known *a priori*. For cases where the experimental lift curve slope differs markedly from the value 2π, the constant incidence corrections must be applied in several steps. The first step utilizes the theoretical value in equation (19b) to obtain an approximation to the corrected lift curve. The slope of this curve is then calculated and the corrections are repeated with the improved value for $\frac{\partial C_{\ell_F}}{\partial \theta_F}$. This procedure is carried out iteratively, and was used in the correction of the experimental data described in Chapter IV. Two iterations were normally required.

D. Viscous Effects and Non-Linear Coupling

Except for the wake blockage, the previous corrections are all based on inviscid flow theory. So long as the flow remains attached this should be satisfactory, with one exception. When the wall interference is large, the airfoil pressure distribution can be altered considerably. On certain airfoils where the pressure distribution has a critical effect on the boundary layers (laminar flow

airfoils), this interference can drastically alter the model behaviour far beyond the normal corrections. The ability to predict such behaviour in order to estimate corrections requires a complete and accurate theory for the viscous flow field itself which, if available, precludes the need for the tunnel tests in the first place. Thus, caution must be exercised when testing such critical boundary layer models, and extreme tunnel geometries should be avoided.

When the model is thick, large, or mounted off the tunnel center-line, the blockage and lift interference are no longer independent. Blockage will then induce transverse velocity components, thereby affecting the incidence and effective camber of the section. Lift interference will induce longitudinal components which will interact with the solid blockage. For multi-element sections the situation becomes much more obscure due to the extreme flow curvature behind high lift flaps.

For tunnel geometries where the corrections are coupled, it is reasonable to formulate a correction theory where a single correction is calculated which simultaneously includes both effects. The theory of the present work, described in the following chapter is one such method.

E. Modern Methods

It is observed that the theory for wall corrections for small thin sections at low incidence was well established by the mid-century. At that time, the computational limit of

existing methods was reached. The extremely involved conformal analysis method of Moses [9] is a case in point. Without the benefit of fast computation the method is quite unwieldy and may explain why the conformal methods and similar exact analyses for correction estimation are not more well known. Several extensions to the theory have occurred more recently, made possible by the development of modern computers. One such method is due to Mokry [14] who determined the corrections for subsonic flow in tunnels with perforated walls. Williams and Parkinson [2], in studying the effect of a slotted upper wall, used a singularity method to model the tunnel flow. De Vries and Schipholt [15], also using the singularity method, found large deviations of the standard forms for two element sections, and showed the importance of the model rotation point. These modern correction techniques are not in wide-spread use, probably due to the difficulty in setting up universal correction formulae for non-standard tunnel geometries.

F. Conclusion

The main result of this brief survey of wind tunnel correction theory is that the usual corrections are valid for small, thin airfoil sections, operating at low incidence, at or near the tunnel center-line. When all higher order terms in thickness, chord-to-height ratio, and incidence are neglected, the lift interference is

independent of the blockage, and vice versa. Clearly, however, the strict assumptions of these theories are not met when testing large, high-lift models. In particular, the treatment of multi-element, high-lift sections with the extreme downward deflection of the trailing streamlines is not complete. Using an improved method, the coupled effects of lift interference and blockage may be obtained simultaneously. The proposed method, described in the following chapter, utilizes a numerical solution for the complete flow field within the tunnel, following the suggestion of Garner, without restrictions on the tunnel geometry.

III. Theoretical Analysis of Tunnel Interference

This chapter will describe the method developed to predict the combined solid blockage and streamline curvature corrections for two dimensional testing in closed wind tunnels. These corrections are necessary due to the reduction in tunnel cross sectional area at the model and the constraining effect of the tunnel walls, and may be derived using potential flow analysis. The method is based on the theoretical calculation of the section force and moment coefficients for both a free field and a bounded field. The difference in values corresponds to the corrections required to the measured wind tunnel data to compensate for tunnel wall interference.

Solutions for incompressible potential flow in an unbounded fluid have generally been accomplished using either conformal transformation or singularity methods. In the first method, the field is transformed to one of simple geometry for which the flow solution is known, usually uniform flow past a circular cylinder with circulation. A description of this procedure may be found in the usual major references, for example Abbott and von Doenhoff [16] or Milne-Thomson [17]. Examples are the Joukowski, Karman-Trefftz, and von Mises airfoils which can be mapped directly onto the circle. These mappings are restricted to particular families of airfoils, few of which are

particularly useful in practice. The method of Theodorsen uses a double mapping for an arbitrary airfoil, first to a near-circle, with the second mapping resulting in a perfect circle. A conformal transformation technique due to Williams [18] allows the analysis of two element airfoil sections by mapping to two circles using a two step mapping process.

The singularity, or panel, methods rely on the principle of superposition of solutions for the linear Laplace equation for the velocity potential or stream function. The airfoil is represented by a distribution of source and/or vortex elements, either on the airfoil surface or in the interior of the profile. The singularity strengths are found such that the total flow composed of the onset uniform stream and the superposed singularities satisfies certain boundary conditions on the airfoil surface and at the trailing edge. This results in the solution of a large set of simultaneous linear algebraic equations. These integral techniques have reached a high level of refinement, can be used for multiple bodies of arbitrary shape, and can be extended to three dimensional flows. Both de Vries and Schipholt [15] and Williams and Parkinson [2] have applied the singularity method to the problem of wind tunnel corrections. Singularity techniques do not easily provide the flow solution throughout the field, but rather give the flow on the airfoil surface as primary solution.

The method to be used in the present work is quite different from these. The potential flow is found throughout

the wind tunnel flow field using finite difference methods to solve the Laplace equation for the stream function. The influence of the tunnel geometry is felt through the boundary conditions imposed on the solution at the airfoil surface and on the tunnel walls. One of the prime difficulties with finite difference techniques is the numerical implementation of boundary conditions at irregularly shaped boundaries. The boundary conditions have a dominant effect on the solution since the Laplace equation is elliptic. It is therefore essential that the boundary conditions be implemented accurately in the numerical scheme. In a Cartesian field, special finite difference expressions must be developed for nodes on or near an irregular boundary, using special differencing and interpolation techniques. This not only increases the numerical error but also adds considerably to the programming effort and precludes the generality of the program code to other shapes.

The use of natural coordinate systems, in which a boundary contour coincides with a constant coordinate line, alleviates this difficulty by allowing the placement of computational nodes exactly on the flow boundaries and distributing the nodes in a rational manner throughout the field. This involves a transformation of coordinates, much as occurs in many analytical solutions where non-Cartesian coordinate systems are chosen to facilitate the solution. The governing equations are written in the transformed

coordinates, and boundary conditions are carried over to the transformed plane. The solution in the transformed plane may then be carried out on a regular rectilinear grid, with well posed boundary conditions. A simple example of such a coordinate transformation is the use of polar coordinates, which is useful when the physical boundaries are composed of concentric circles, as shown in Figure 4a. The actual solution of the transformed governing equation takes place in the transformed plane, Figure 4b. Whether the solution is analytic or numerical in nature, the use of the coordinate transformation has allowed the boundary conditions to be specified on straight lines. Of particular importance to numerical solutions is the fact that the flow field is now represented by a grid of equally spaced computational nodes arranged on a simple rectangular grid.

There are many possible transformations which result in such rectangular grids and in general such curvilinear coordinate systems are non-orthogonal. These coordinate systems may be generated in several ways, which may be classified as algebraic, conformal, analytic, or numerical schemes. The application of analytic and conformal grid generation is limited in that, generally, the variety of shapes that can be treated is small, and only a few specialized mappings can handle multiple bodies. However, analytic and conformal mapping techniques generally produce orthogonal grids, which in a numerical solution reduces some of the truncation errors which result in the discretized

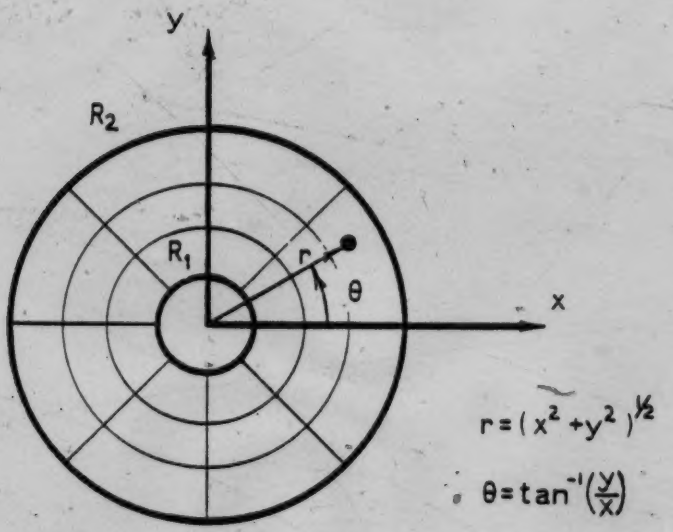

a) physical plane

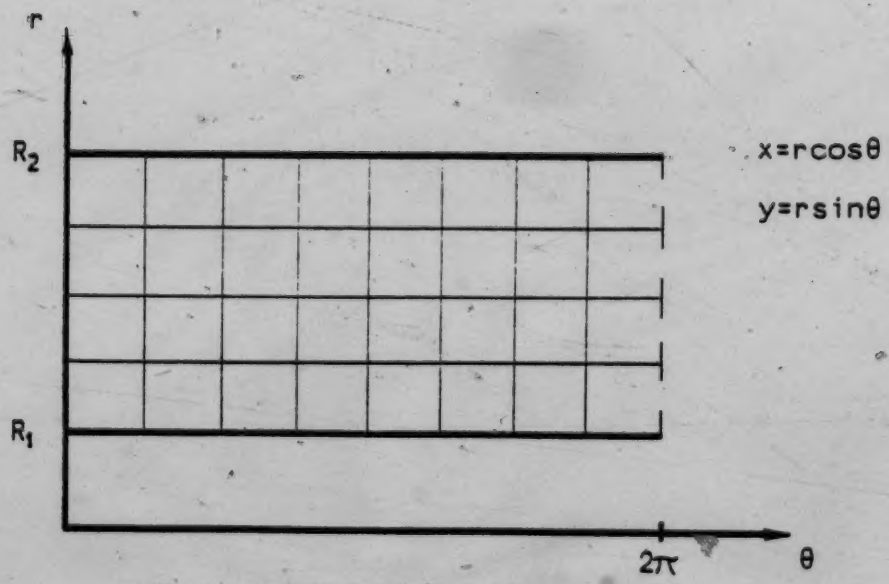

b) transformed plane

Figure 4 Analytical Coordinate Transformation - Polar Coordinates

system. Algebraic systems are currently under development, see for example Eiseman [19].

The method of coordinate transformation to be used here is a numerical grid generation technique. This method is much more general in that it is possible to generate a coordinate grid for a flow field with irregular outer boundaries containing any number of arbitrarily shaped bodies. The grid generation and flow solution algorithms for different flow problems require only that the flow fields be topologically equivalent. The numerical grid generation methods are also easily extended to three dimensional problems. Although this method of grid generation was introduced in the mid-1960's, its recent popularity is due largely to the work of Thompson, Thames, Mastin, et al., at Mississippi State University in the past six years. Application of the method of boundary fitted coordinate systems is currently being made to a wide range of fluid flow problems, including time-dependent, compressible viscous flow with movable boundaries. There is a growing literature on the use of these coordinate systems, with recent efforts directed towards the adaptive and time-dependent grid systems in which the coordinate grid is adjusted during the flow solution to concentrate the computational nodes in regions where the solution exhibits large gradients, thus increasing the solution accuracy.

In the method of Thompson [20,21], the curvilinear coordinate grid is generated by the numerical solution of a

set of elliptic equations, called the grid generators. Boundary conditions for the grid generators are specified by the desired distribution of computational nodes along the physical flow boundaries. The solution of the generating system establishes a correspondence, or mapping, of discrete points in the physical plane to the nodes in the rectangular computational plane. By transforming the grid generation equations to the computational plane, the generator solution is itself carried out in a manner which takes advantage of the well posed boundary conditions.

Once the coordinate system has been obtained, the task remains to solve the partial differential equation which applies to the particular problem. The governing equation is transformed to the new coordinate system, just as is the case when using polar coordinates in an analytical solution as discussed previously. In the present case, the potential flow solution is found by transforming the Laplace equation for the stream function and solving the resulting equation numerically using appropriate boundary conditions. The stream function values are specified on the flow boundaries, i.e. the airfoil surface and the tunnel walls, entrance, and exit planes. By virtue of the coordinate transformation, the boundary computational nodes fall on rectilinear boundaries in the computational grid.

For lifting potental flow, the total solution is found by superposition of the basic solutions for uniform onset flow with zero circulation and for zero onset flow with unit

circulation, which are obtained separately. The required circulation is determined by application of one of several forms of the Kutta condition which are also expressed in the computational plane. Since each computational node in the transformed plane corresponds uniquely to some point in the physical plane, the total flow solution is therefore known at these points.

The remainder of the analysis is composed of the calculation of the surface pressures on the airfoil and tunnel walls, which may be integrated to give the lift and pitching moment coefficients. All of these calculations may be carried out in the computational plane, and in fact, once the physical boundary points are input into the grid generation, they never re-appear until the final results are presented.

The preceeding method of analysis was used to obtain the flow solution for an airfoil section in a two-dimensional wind tunnel. Free field values for the force and moment coefficients were obtained using the singularity method of Kennedy [13]. By comparing results from these two analyses the required adjustments needed to correct the wind tunnel data for the interference of the walls was obtained.

A. Grid Generation

In the method of Thompson, the transformation to (ξ, η) coordinates represented by $\xi(x,y)$ and $\eta(x,y)$, is found by the solution of two elliptic partial differential equations

(the grid generators):

$$\nabla^2\xi = \xi_{xx} + \xi_{yy} = P(\xi,\eta) \tag{22a}$$

$$\nabla^2\eta = \eta_{xx} + \eta_{yy} = Q(\xi,\eta) \tag{22b}$$

with Dirichlet boundary conditions. The boundary conditions take the form of the desired coordinate values (ξ,η) at discrete points on the irregular physical boundaries. One coordinate is held constant while the other varies monotonically around or along the boundary. This form of grid generator and boundary conditions ensures a unique mapping from the physical to the computational space. The inhomogeneous functions $P(\xi,\eta)$ and $Q(\xi,\eta)$ allow the generated mesh to be concentrated in regions of interest, usually where gradients in the flow solution are high or the boundaries are highly curved.

Since it is desired to perform all calculations in the regular transformed plane, i.e. to find $x(\xi,\eta)$ and $y(\xi,\eta)$, the dependent and independent variables in the above generating equations (21) are interchanged to give:

$$\alpha x_{\xi\xi} - 2\beta x_{\xi\eta} + \gamma x_{\eta\eta} = -J^2\left[Px_\xi + Qx_\eta\right] \tag{23a}$$

$$\alpha y_{\xi\xi} - 2\beta y_{\xi\eta} + \gamma y_{\eta\eta} = -J^2\left[Py_\xi + Qy_\eta\right] \tag{23b}$$

where

$$\alpha = x_\eta^2 + y_\eta^2 \qquad \beta = x_\xi x_\eta + y_\xi y_\eta$$

$$\gamma = x_\xi^2 + y_\xi^2 \qquad J = x_\xi y_\eta - x_\eta y_\xi$$

with boundary conditions (i.e. values of x and y at the desired computation points on the physical boundaries) specified on the straight boundaries of the computational grid.

The terms α , β , γ , and J (the Jacobian of the transformation) are called the transformation metrics or scale factors. The metrics are obtained during the grid generation, i.e. the solution of equations (23a) and (23b), and will appear later in the flow solution equations. A physical interpretation of the metrics may be made in terms of the grid orientation, orthogonality, cell size, and cell aspect ratio, as discussed in a later section.

There are numerous configurations which may be generated using the elliptic system due to the flexibility allowed in the specification of the boundary conditions on the computational grid. For the present work, four grid types were investigated. The first two are commonly referred to in the literature as O-type and C-type grids. The last two are designated here as S-type and 2S-type grids.

Grid Types

The O-type grid as it appears in the physical plane is shown in Figure 5a. The corresponding computational grid is

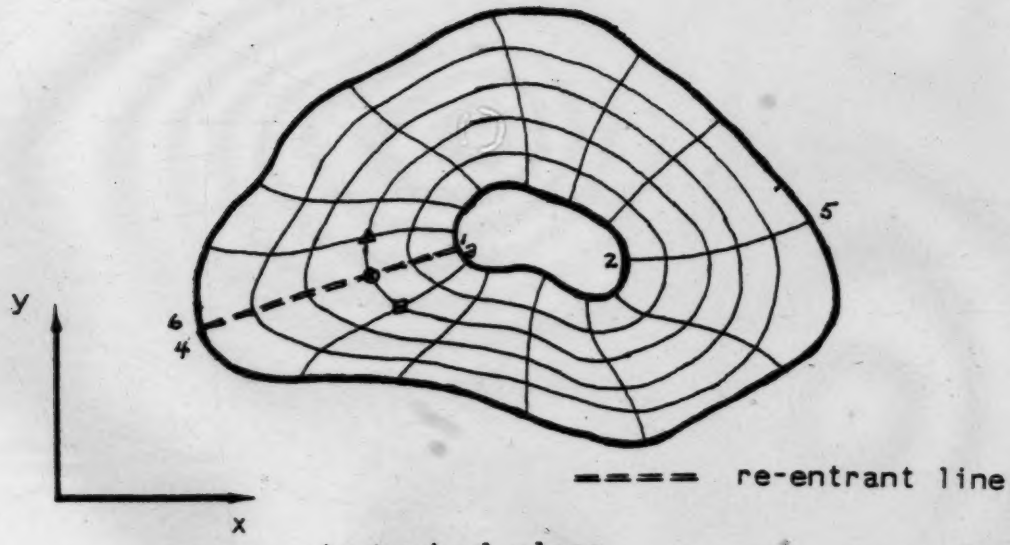

a) physical plane

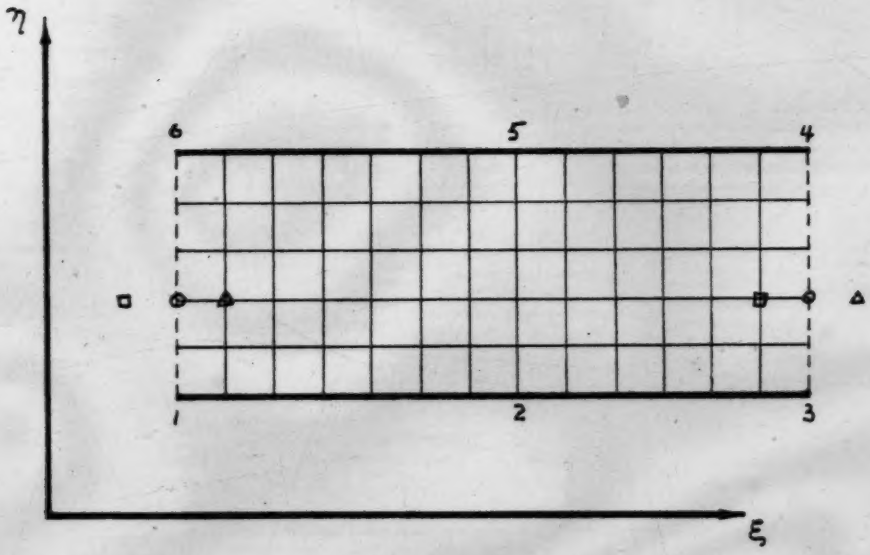

b) transformed plane

Figure 5 O-Type Grid - General Form

shown in Figure 5b, with numbered points corresponding to those in the figure above. The notable features of this grid type are the uniformity of the mesh near the inner boundary, and the re-entrant line on the left and right-hand sides of the computational grid which appears as a cut in the physical plane between the inner and outer boundaries. The O-type grid is similar to a polar coordinate system, where the re-entrant line occurs at $\theta=0$ and 2π. Solutions are required to be continuous across the re-entrant line, and in fact the solution is periodic in ξ. Values of x and y are neither specified nor allowed along the re-entrant line, but are found during the grid generation by requiring continuity of the solution and first derivatives across this line, as shown by the symbols.

The C-type grid is shown in Figure 6a and 6b, again with numbered points to establish the correspondence of computational points with the physical plane. This grid also has a re-entrant line, this time along a portion of the lower edge of the computational grid. Again, specification of values of x and y at these points is neither necessary nor allowed.

The S-type and 2S-type grids present another possible arrangement in the transformed plane. For these grids, interior boundaries are mapped onto slits in the transformed plane. For a single interior body, this mapping results in a grid as shown in Figure 7a, with the slit shown in the transformed plane, Figure 7b. For the grid generation, the

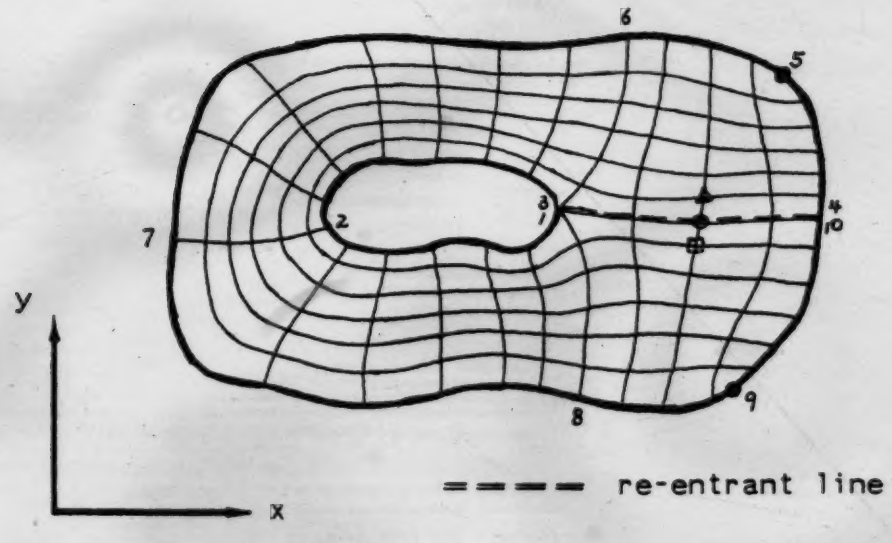

a) physical plane

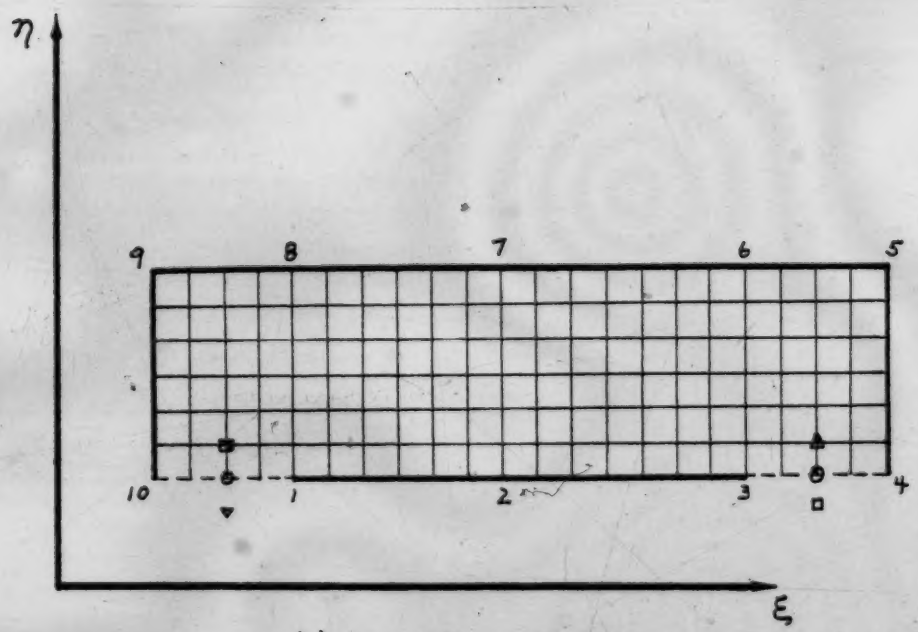

b) transformed plane

Figure 6 C-Type Grid - General Form

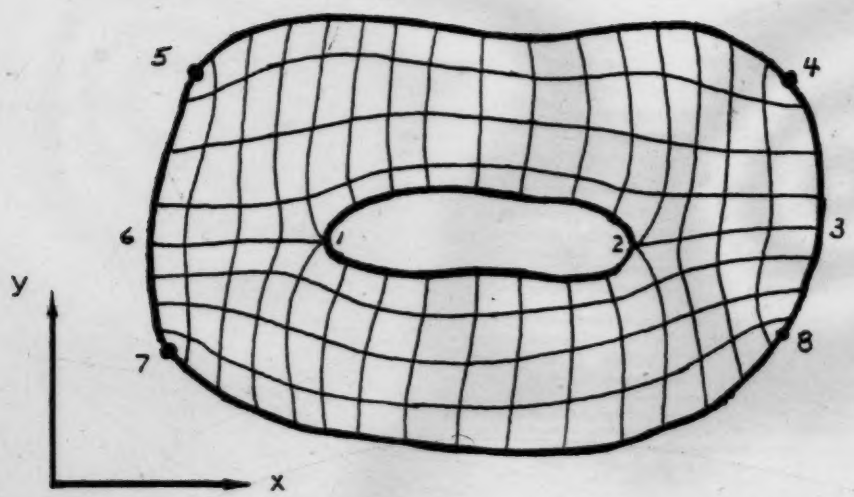

a) physical plane

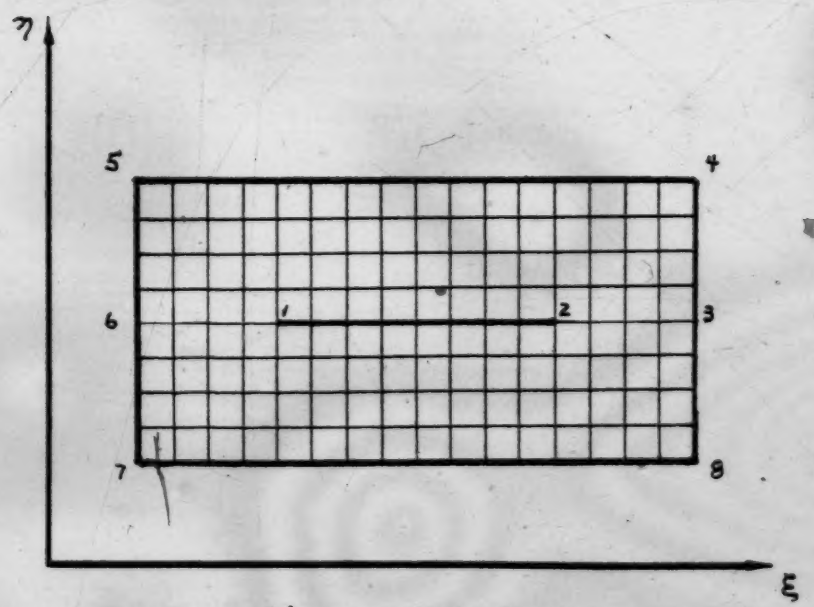

b) transformed plane

Figure 7 S-Type Grid - General Form

slit boundary condition is multi-valued in x and y, the value used depending on which side of the slit computations are performed. There is no re-entrant line. The 2S-type, or double slit geometry, is shown in Figure 8a and 8b for two interior bodies. Here also the slit boundary conditions are multi-valued. Using the slit geometries, it is possible to set up grids for much more complicated sections: a 4S-type grid might be used for an airfoil section with a double slotted flap and leading edge slat. The slits may also appear vertically in the transformed plane. The present work has been limited to the simplest two element case of a single slotted flap.

Of these four grid types, only the O-type grid has been investigated in detail for potential flow solutions (Thompson[24]). Each of these grid configurations offered some advantages to some part of the problem at hand, and were therefore investigated in some detail. The over-all accuracy of the flow solution depends on several properties of the generated coordinate grid in the physical plane. In general, as with all finite difference methods, accuracy deteriorates if the grid cells are large, or if the grid geometry changes abruptly or rapidly from point to point in the physical plane. This is especially true if the solution exhibits high gradients in these regions of rapid grid change. Furthermore, although it is not necessary that the grid be orthogonal, highly skewed grids contribute to the local truncation error of the flow solution. The effect of

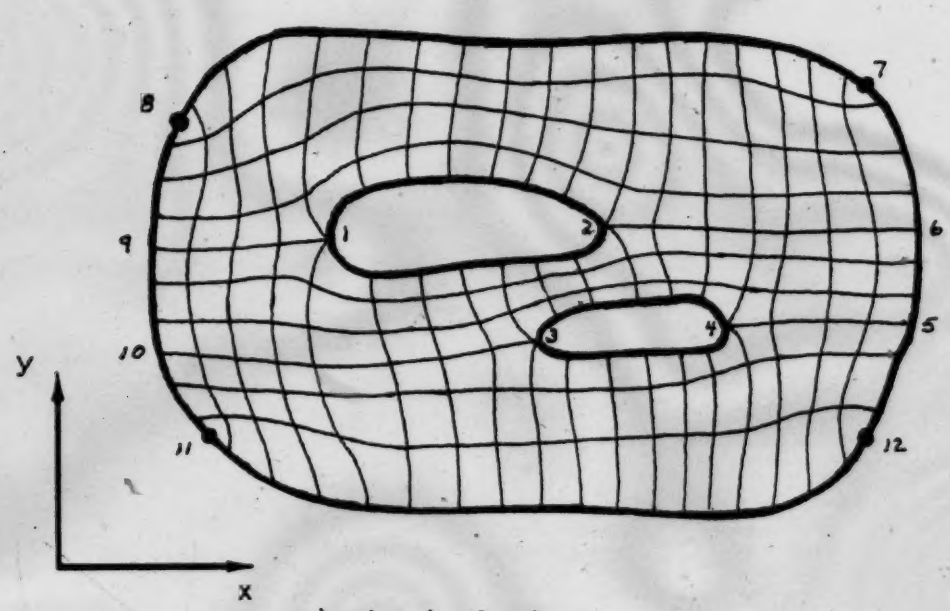

a) physical plane

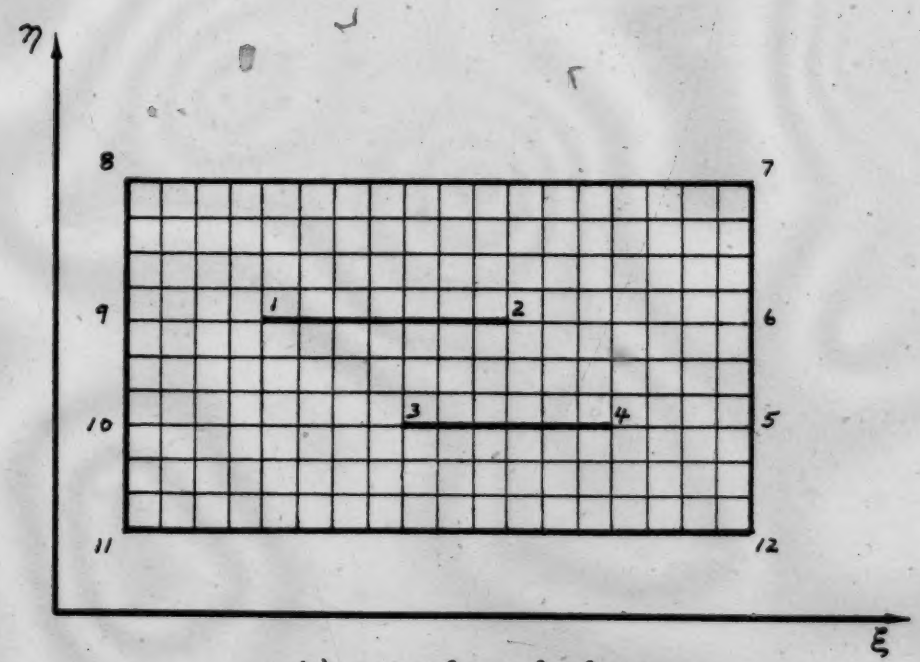

b) transformed plane

Figure 8 2S-Type Grid - General Form

the physical geometry of the computational grid is felt through the metrics. Since the metrics are calculated using standard finite difference forms, they become susceptible to the normal errors of truncation. Thus, although the transformed flow equation may be exact in form, the finite difference solution will be degraded by truncation errors arising not only from the discretization, but also from the transformation metrics which it utilizes, as demonstrated by Kerlick and Klopfer [22]. It is desireable, therefore, to obtain grids with near uniform cell size, or no more than slow size variation over the grid, and with no more than slight skewness. With this in mind, representative grids of each type for the wind tunnel geometry are shown in Figures 9 to 13.

The O-type grid, Figure 9, has the best mesh properties near the airfoil surface, with the exception of the sharp trailing edge, but very poor properties near the outer boundaries, where the mesh is composed of large, highly skewed cells. In these outer regions of the flow the solution does not change rapidly, so the grid may be tolerated.

The C-type grids, Figure 10, were investigated as a means for improving the grid quality upstream from the model. This was desired in order that the wind tunnel contraction could be included in the solution field if desired, as shown in Figure 11.

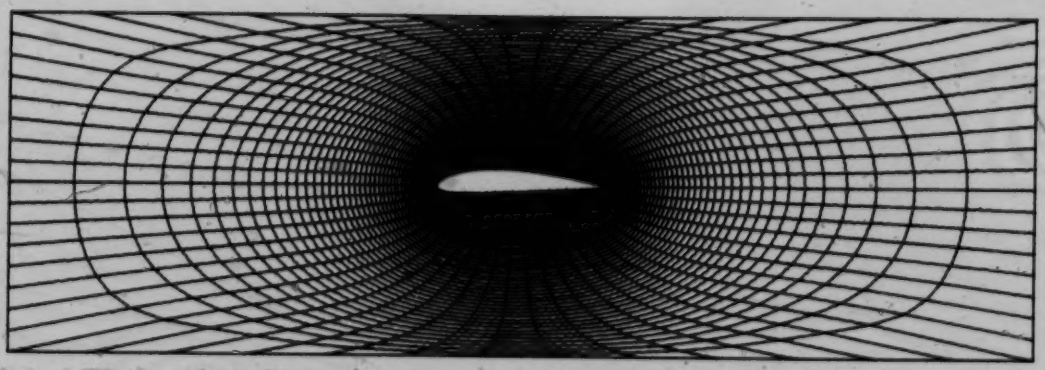

a) entire flow field

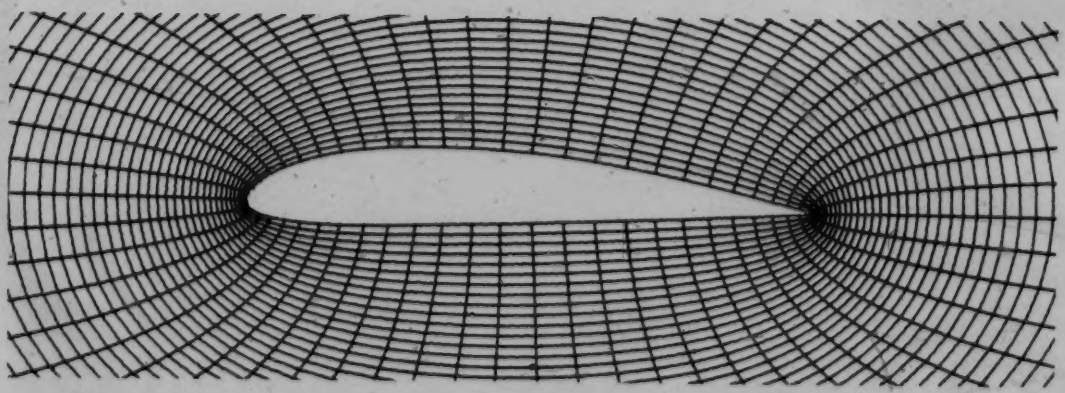

.b) airfoil detail

Figure 9 O-Type Grid - Wind Tunnel Geometry

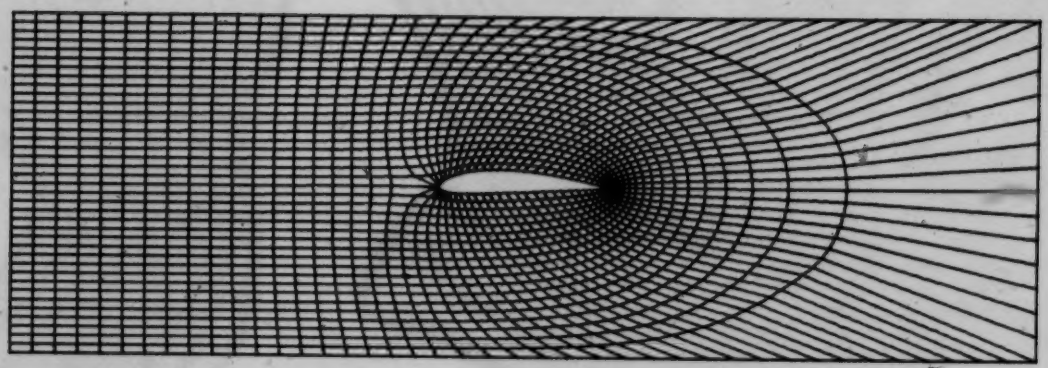

a) entire flow field

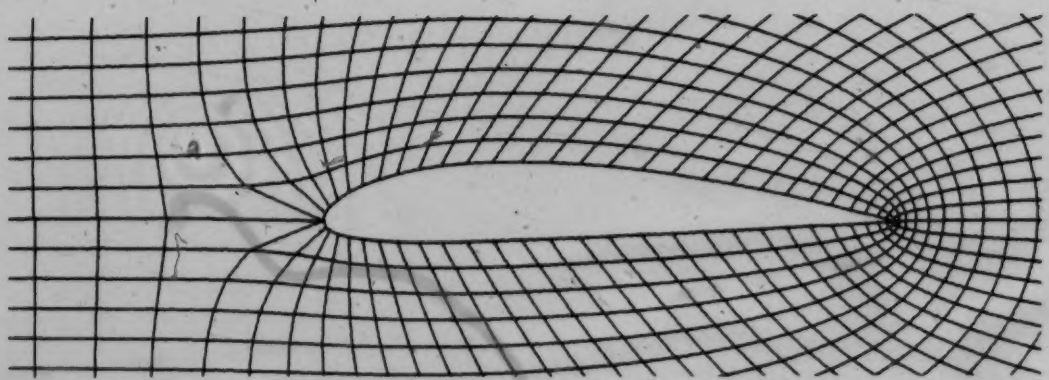

b) airfoil detail

Figure 10 C-Type Grid - Wind Tunnel Geometry

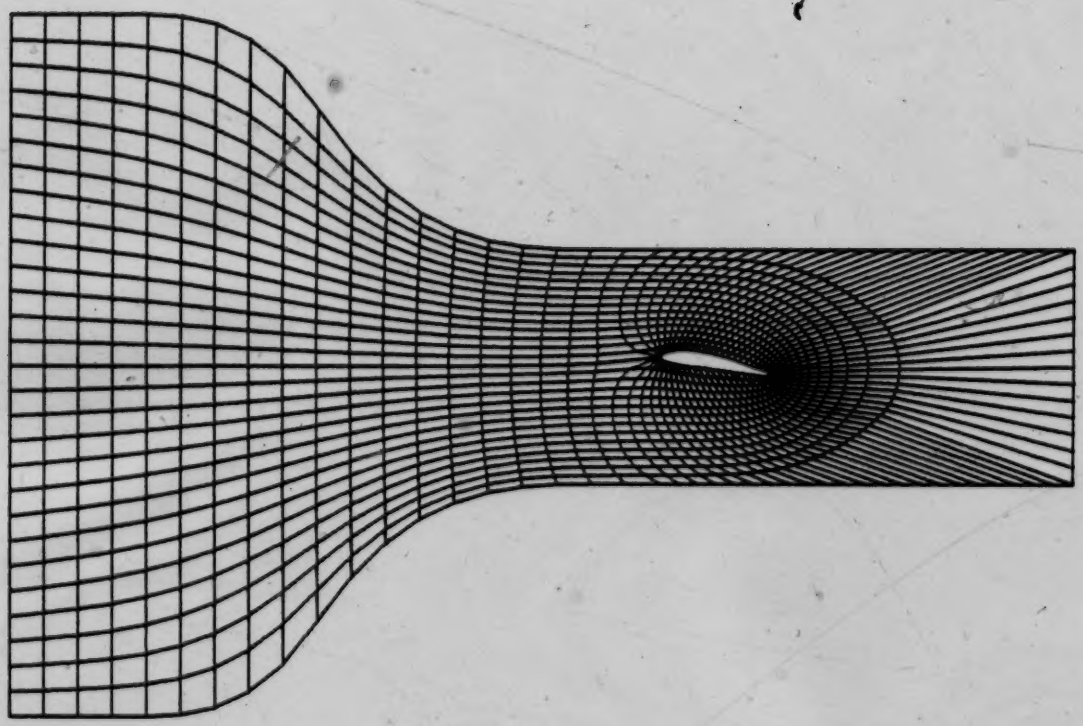

Figure 11 C-Type Grid - Tunnel Contraction Geometry

The S-type grids, which are well suited to duct flows as they have excellent form upstream and downstream from the model, are poor near the section leading edge as shown in Figures 12 and 13. The S-type grids are also well suited to the contraction geometry. The two element section grids could be generated using a form of the C-type grid, however the mesh generated in the slot region is unsatisfactory due to extreme skewness and poor spacing. Thompson solved this problem (see [21]) by performing an auxilliary transformation where the section coordinates were inverted with respect to infinity. This had the added advantage of allowing the outer boundary to be moved a very large distance away from the airfoil, and the implementation of near-infinity boundary conditions for free field flow solutions. The added complexity in the flow equations, which must also be inverted, prevented this method from being applied for an actual flow solution [23]. Using the 2S-type grids an adequate mesh could be generated in the slot region with little difficulty.

It is observed that none of these grids is uniformly orthogonal, however this property is not required, nor even desired. In fact, demanding an orthogonal grid would over-specify the problem and eliminate the freedom with which the boundary point distribution could be specified.

Minimization of the grid induced errors may be accomplished either by proper specification of the boundary point distribution, or by use of the weighting functions P

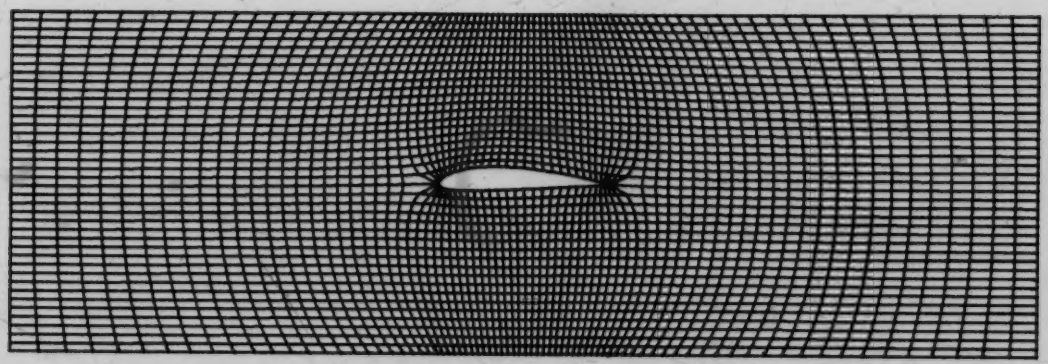

a) entire flow field

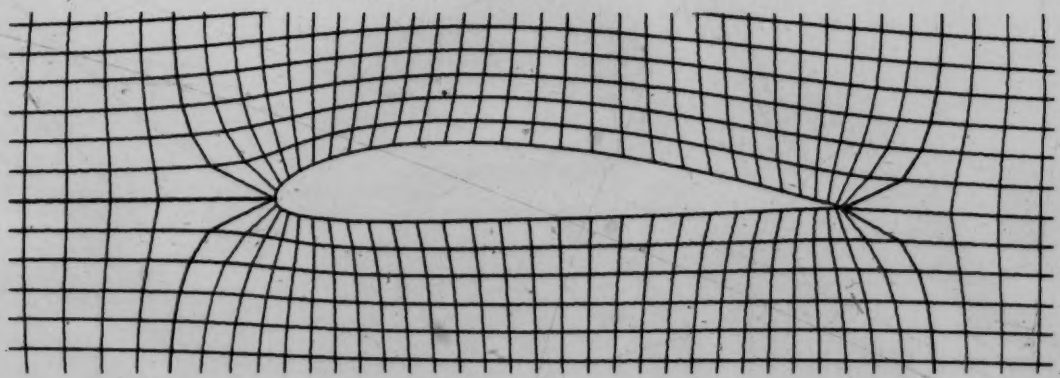

b) airfoil detail

Figure 12 S-Type Grid - Wind Tunnel Geometry

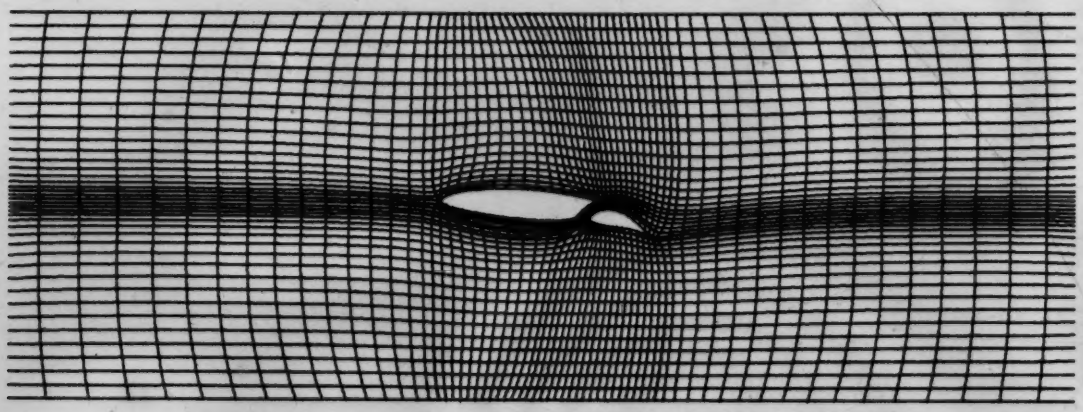

a) entire flow field

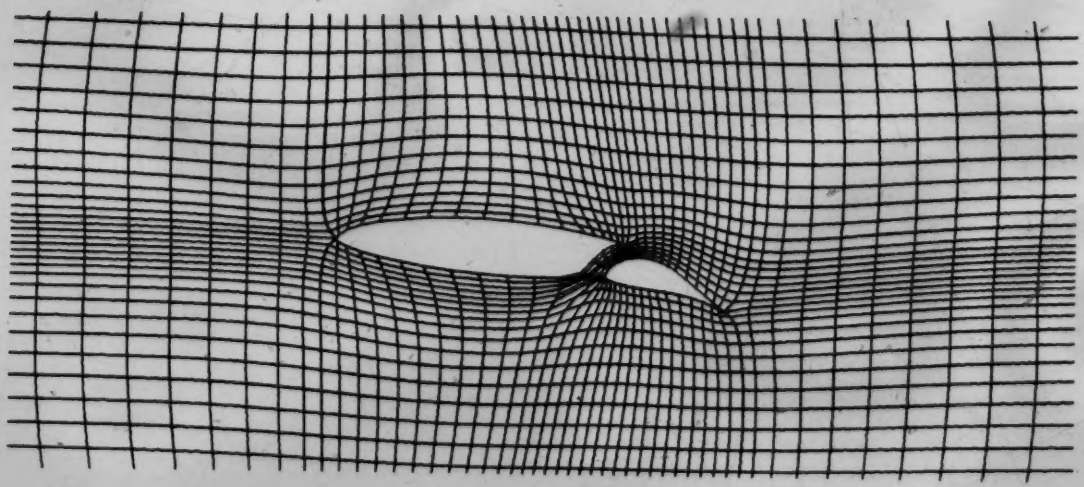

b) airfoil detail

Figure 13 2S-Type Grid - Wind Tunnel Geometry

and Q.

Boundary Point Distribution

The over-all accuracy is dependent on the chosen distribution of points on the boundary contours. It is desirable to use as few points as possible, consistent with desired accuracy, in order to reduce required computer time. Critical regions of the flow are near the section leading edge where the flow curvature is high, and the trailing edge where the Kutta condition is implemented. Thompson [24] showed that for the O-type grids accuracy was improved more by concentration of points near the trailing edge than near the leading edge. In the present work this was also found to be the case for the other grid types.

The airfoil boundary points were specified using the distribution:

$$x_i = \frac{1}{2}(1 - \cos\phi_i)$$

where

$$\phi_i = \frac{i-1}{NF-1}\phi_{NF} \quad , \quad i = 1 \ , \ NF$$

$$\phi_i = \phi_{NF} + \frac{i-NF-1}{NA-1}(\pi-\phi_{NF}) \quad , \quad i = NF+1 \ , \ NF+NA$$

giving NF points distributed between the leading edge (with slight concentration) and the point corresponding to ϕ_{NF}, usually 120 degrees, and NA points between ϕ_{NF} and the

trailing edge. With these x coordinates, the corresponding y coordinates of the surface were found using a cubic spline interpolation routine, following the procedure of Kennedy [13], using the section input coordinates. A typical point distribution is shown in Figure 14 for a 20% thick symmetrical Joukowski airfoil, using NF=NA=15.

The outer boundary point distribution scheme was identical for each of the four grid types investigated. The cross stream boundary points were equally spaced along the tunnel inlet and exit planes, while the wall point spacing increased from the region of the model to the end lines.

Grid Control Functions

In order to optimize the grid within the field, a high degree of control is possible using the inhomogeneous functions P and Q in the grid generators. By setting the magnitude and sign of the functions P and Q at each point, the generated grid can be tailored to the problem at hand. The form of the control functions used in the present work is the same as that of Thompson [21]. The functions are evaluated at each point in the transformed plane as sums of decaying exponentials, where the magnitude and sign of each term are arranged to attract or repel grid lines from specified locations. The strength of the attraction and eventual clustering of cells is determined by the magnitude of the function, while the sign determines the direction of attraction of the coordinate lines in the physical plane.

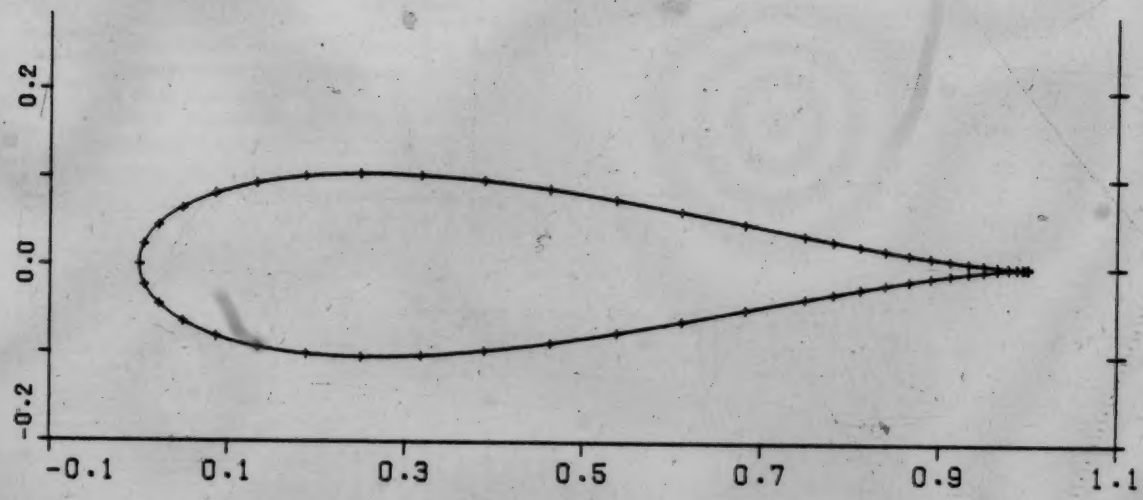

Figure 14 Airfoil Boundary Point Distribution

The functional forms of P and Q are:

$$Q(\xi,\eta) = -\sum_{i=1}^{n} a_i \, \mathrm{sgn}(\eta-\eta_i) \exp\left[-c_i|\eta-\eta_i|\right]$$

$$-\sum_{j=1}^{m} b_j \, \mathrm{sgn}(\eta-\eta_j) \exp\left[-d_j R_j\right] \qquad (24a)$$

$$P(\xi,\eta) = -\sum_{i=1}^{n} a_i \, \mathrm{sgn}(\xi-\xi_i) \exp\left[-c_i|\xi-\xi_i|\right]$$

$$-\sum_{j=1}^{m} b_j \, \mathrm{sgn}(\xi-\xi_j) \exp\left[-d_j R_j\right] \qquad (24b)$$

where

$$R_j = \left[(\xi-\xi_j)^2 + (\eta-\eta_j)^2\right]^{1/2}$$

The number of terms in each summation is determined by the desired complexity of the grid control desired. The a_i, b_j and c_i, d_j are positive amplitude and decay factors, respectively, which are not necessarily the same for both functions. The presence of the "sgn" function in (24a) and (24b) allows the sign of the control function to change on either side of the desired location of concentration. Positive values for P and Q tend to move grid lines towards higher values of ξ and η, respectively, and vice versa. Thus, the first summation in equation (24a) results in attraction of η-coordinate lines toward the given η_i line in the physical plane while the second summation causes attraction of η lines to a specific point (ξ_j, η_j). Similar

results are obtained with equation (24b), where now the ξ lines are affected. Examples of grid control using the weighting functions are shown in Figures 15 to 18, using the same boundary point distributions as Figures 9 to 13. Overall grid size and control amplitudes and decay factors used are indicated below each figure. In Figure 15, η lines have been concentrated near both the outer boundary and the airfoil surface by using the line attraction form of the Q control function, the first term in (24a), to attract lines to both the upper and the lower boundary of an O-type grid. In Figure 16, the P function has been used to attract ξ lines toward the leading and trailing edge points, the second term in (24b), using an S-type grid. For the S-type grids in the wind tunnel geometry, it was found to be necessary to use a two-step decay function to prevent the ξ lines near the tunnel end lines from responding to the high control values required near the leading and trailing edges, as shown upstream of the model in Figure 16b. An example of a 2S-type grid generated with and without extreme grid control is shown in Figures 17 and 18. In Figure 18, both line and point attractions for P and Q were necessary, using several terms in the summations of equations (24a) and (24b), to obtain an adequate grid distribution near the model.

Guidelines for the use of grid control may be deduced from the tendency for the Laplacian operator used to generate the grids to distribute the grid points evenly in

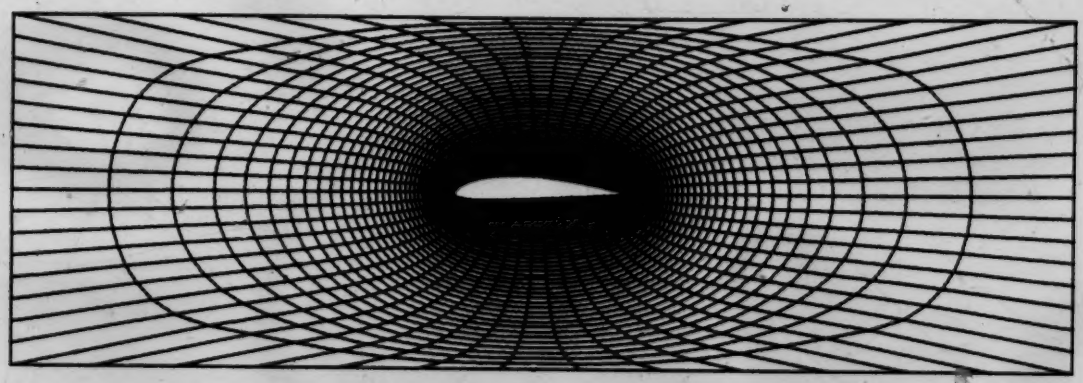

a) no grid control

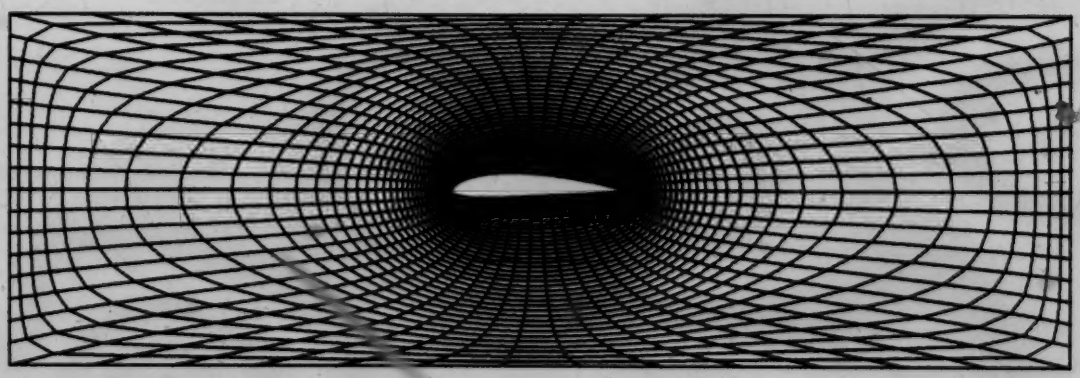

b) with grid control

η-line attraction to inner and outer boundaries

amplitude=200.0 decay rate=0.5

Figure 15 Grid Control - O-Type Grid with Q Control

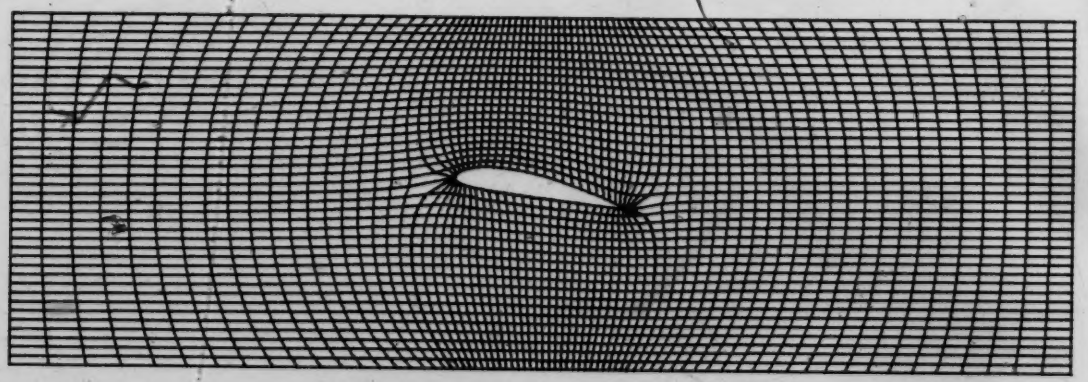

a) no grid control

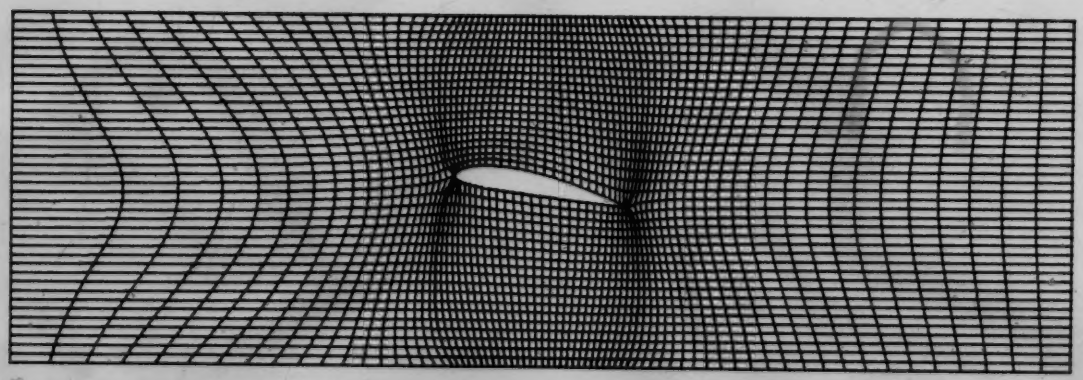

b) with grid control

point attraction of ξ-lines to airfoil LE and TE

amplitude=300.0 decay rate=0.35

Figure 16 Grid Control - S-Type Grid with P Control

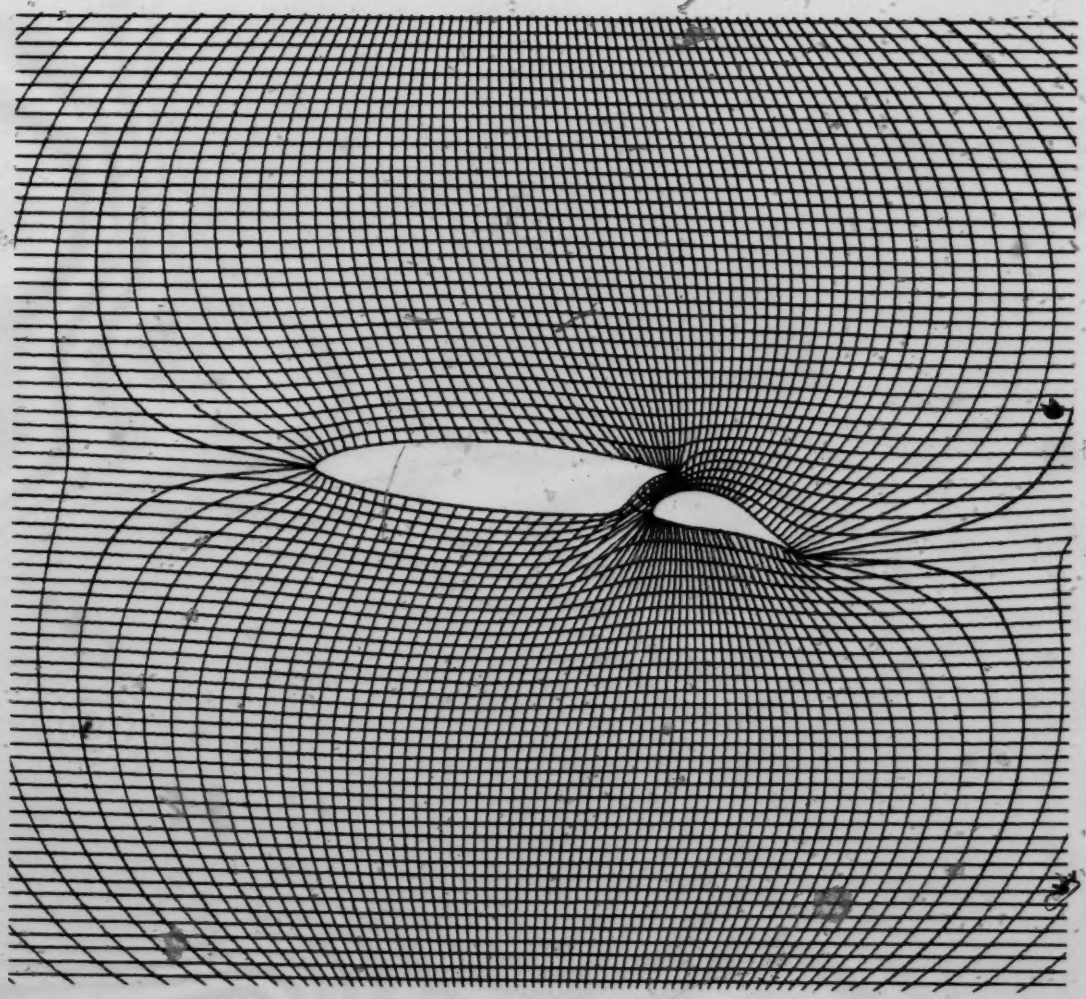

Figure 17 2S-Type Grid - Airfoil Detail - No Grid Control

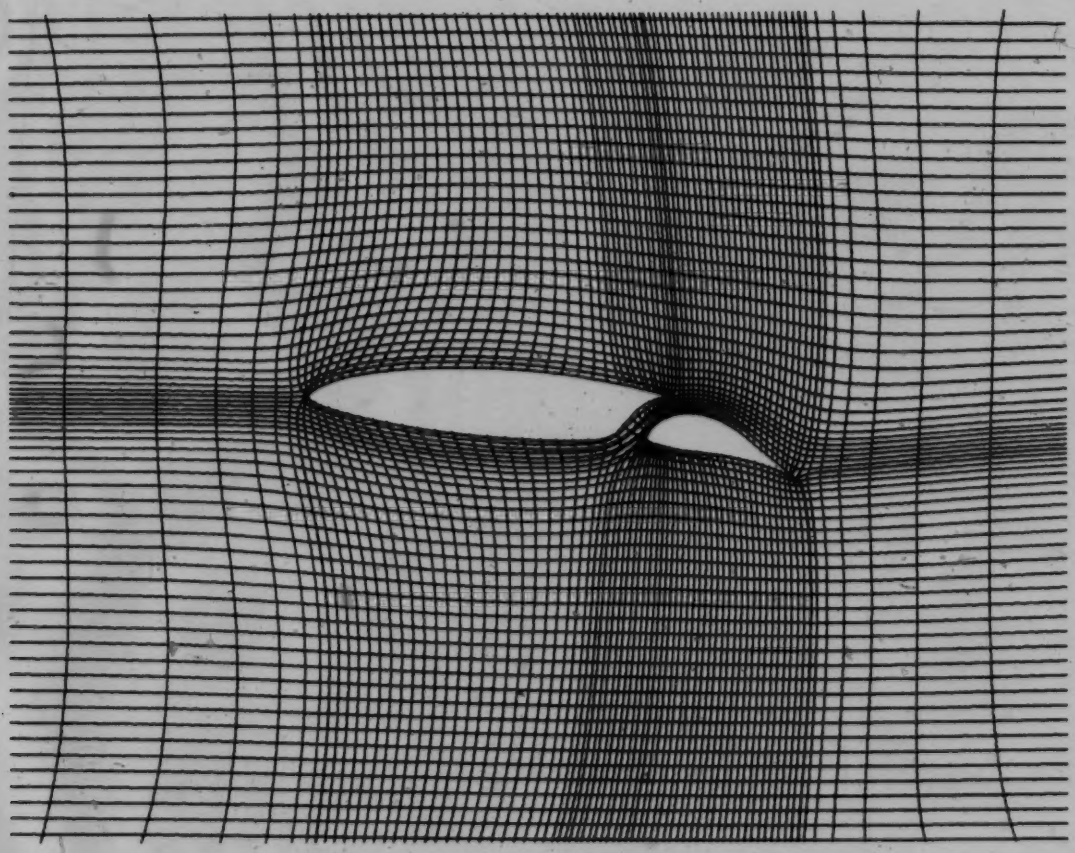

function	attraction type	attraction location	amplitude	decay rate
Q	line	main slit	1875	0.5
Q	line	flap slit	1875	0.5
Q	point	main LE	1875	0.5
Q	point	main TE	1875	0.5
Q	point	flap LE	750	0.5
Q	point	flap TE	1875	0.5
P	line	main LE	1875	1.0
P	line	flap TE	3750	1.0

Figure 18 2S-Type Grid - Airfoil Detail - Strong P and Q Grid Control

the field and to avoid concave boundaries and move toward convex boundaries. In order to maintain the desired grid properties extensive use of the grid control functions is mandatory to achieve accurate results for the flow solution, especially for the slit geometries. Some very interesting work is being done in this area, see for example Brackbill [25] or Anderson and Rai [26], where the grid control is implemented to minimize some form of a penalty function, for example the non-orthogonality of the grid, or to respond to high gradients in the flow solution. These are termed adaptive grid methods. For the present, the optimal grid control parameters were determined by trial and error and were fixed throughout the solution. These parameters depend primarily on the grid type and size. For the grids used in the present work (normally 100 X 80), amplitudes ranged from 100 to 600, and decay factors ranged from 0.1 to 0.5.

B. Potential Flow Solution

The stream function for the two dimensional, inviscid, incompressible flow satisfies Laplace's equation

$$\nabla^2\psi = \psi_{xx} + \psi_{yy} = 0 \qquad (25)$$

with Ψ having constant values on solid boundaries (i.e. these boundaries must be streamlines), and

$$\psi = y\cos\theta - x\sin\theta$$

at a large distance from a body immersed in a uniform flow at angle θ to the x-axis. When transformed to the computational plane, equation (25) becomes

$$\alpha\psi_{\xi\xi} - 2\beta\psi_{\xi\eta} + \gamma\psi_{\eta\eta} = -J^2[P\psi_{\xi} + Q\psi_{\eta}] \qquad (26)$$

where α, β, γ, and J are the transformation metrics obtained during the grid generation and P and Q are the grid control functions. The boundary conditions in the computational grid are specified along lines corresponding to the body contours and the outer boundary of the flow field. In the present case, these boundaries are either streamlines of the flow (Ψ =constant), or occur perpendicular to the flow direction (Ψ a linear function of position).

Considering first a single element section, since the Laplace equation is linear, the total flow may be separated into three parts: ψ^1 due to a uniform onset flow at zero degrees, ψ^2 due to uniform onset flow at ninety degrees, and ψ^3 for circulatory flow with zero onset velocity. These basic solutions are found individually by solving equation (26) with the boundary conditions shown in Table 1.

The total flow is then found by superposition of the three base solutions:

Table 1 Boundary Conditions for Single Element Potential Flow

Basic Solution	Unbounded Flow		Wind Tunnel Flow	
	airfoil	outer boundary	airfoil	outer boundary
1. Uniform stream at Zero Degrees	0	y	0	y
2. Uniform stream at Ninety Degrees	0	-x	---	---
3. Circulatory Flow	1	0	1	0

$$\psi^T = \psi^1 \cos\theta + \psi^2 \sin\theta + \lambda\psi^3 \qquad (27)$$

where θ is the desired angle of the onset flow, and λ is to be determined for a given θ by the Kutta condition. For the general problem, the three basic solutions need to be calculated only once. Thereafter, the total stream function at any angle may be found by finding the appropriate λ, as discussed in the following section.

For the two element case, the total flow is separated into four solutions: ψ^1 and ψ^2 as before, ψ^3 for circulatory flow about the main section, and ψ^4 for circulatory flow about the flap. Again, these solutions of the Laplace equation are found separately using the boundary conditions given in Table 2. The total flow is then given by

$$\psi^T = \psi^1 \cos\theta + \psi^2 \sin\theta + \lambda_1\psi^3 + \lambda_2\psi^4 \qquad (28)$$

where θ is the angle of the onset flow, and λ_1 and λ_2 are determined by the satisfaction of the Kutta condition on the two components of the section. This involves the simultaneous solution of two linear algebraic equations for each angle of attack, as discussed in the following section.

For the present problem, the onset flow and tunnel walls are parallel, and the model incidence is set by rotating the model coordinates about a given point on the chord line. Hence, $\theta=0$, and the ψ^2 term vanishes from

Table 2 Boundary Conditions for Two Element Potential Flow

Basic Solution	Unbounded Flow			Wind Tunnel Flow		
	main	flap	outer boundary	main	flap	outer boundary
1. Uniform Stream at Zero Degrees	0	0	y	0	0	y
2. Uniform Stream at Ninety Degrees	0	0	-x	---	---	---
3. Circulatory Flow (main)	1	0	0	1	0	0
4. Circulatory Flow (flap)	0	1	0	0	1	0

the total flow. For the single element section this leaves just two basic flow solutions to be found to give the total flow by

$$\psi^T = \psi^1 + \lambda\psi^3 \tag{29}$$

while three basic solutions are required for two element sections, where the total flow is given by

$$\psi^T = \psi^1 + \lambda_1\psi^3 + \lambda_2\psi^4 \tag{30}$$

Boundary conditions for these basic solutions in the wind tunnel geometry are also given in Tables 1 and 2. For each new geometric angle of attack of the section in the wind tunnel, a new grid must be generated, and new basic solutions found, which involves a great deal of extra computation. If the change in angle of attack is not large, the basic solutions are very similar, so that the solution for one angle may be used as input to the iterative solution at the new angle.

Evaluation of Velocities and Surface Pressures

Velocity components of the total flow solution may be found by evaluating

$$u = \psi_y^T \quad , \quad v = -\psi_x^T$$

which in the computational grid take the form (omitting the superscript "T" for clarity)

$$u = \frac{1}{J}\left[x_\xi \psi_\eta - x_\eta \psi_\xi\right] \tag{31a}$$

$$v = \frac{1}{J}\left[y_\xi \psi_\eta - y_\eta \psi_\xi\right] \tag{31b}$$

In the field, these derivatives are found using second order central difference formulae. On the boundaries, second order one-sided expressions are used for the derivatives normal to the boundary. Velocity components on solid boundaries (ψ =constant), which here correspond to lines of constant are given by (since $\psi_\xi = 0$)

$$u = \frac{x_\xi \psi_\eta}{J} \tag{32a}$$

$$v = \frac{y_\xi \psi_\eta}{J} \tag{32b}$$

On the surface, the tangential velocity is therefore given by

$$V = (u^2+v^2)^{1/2} = \frac{\gamma^{1/2}\psi_\eta}{J}$$

The pressure coefficient, either in the field or on the boundary is given by

$$C_p = 1 - V^2$$

In the field, then, the pressure coefficient is given by

$$C_p = 1 - \frac{1}{J^2}\left[\alpha(\psi_\xi)^2 - 2\beta\psi_\xi\psi_\eta + \gamma(\psi_\eta)^2\right] \qquad (33a)$$

while on the solid boundaries

$$C_p = 1 - \frac{\gamma(\psi_\eta)^2}{J^2} \qquad (33b)$$

Kutta Condition Implementation

The amount of circulation generated by a lifting airfoil in an inviscid fluid is determined by the condition that the flow leave the trailing edge smoothly, commonly referred to as the Kutta condition. Historically, this condition has been implemented in several ways. In conformal transformation methods, the circulation is given around the cylinder in the transformed plane by requiring that the rear stagnation point map onto the airfoil trailing edge. In the singularity techniques, the Kutta condition has been implemented in terms of velocities or flow direction. The velocity condition takes two forms: equal velocity on the upper and lower surface at the trailing edge, or zero velocity. A less restrictive (and physically more reasonable) implementation is specification of the flow direction at the trailing edge. This is accomplished (see Kennedy [13]) by placing a control point on the trailing edge bisector at a very short distance behind the trailing edge and requiring the stream function at the control point to coincide with the value on the airfoil surface. An

alternative implementation of the trailing point condition is the requirement that the velocity vector at the trailing edge be in the direction of the trailing edge bisector. For the singularity techniques, Kennedy showed the trailing point Kutta condition to be superior to the velocity methods by allowing a reduction in the number of airfoil surface elements.

Both the velocity and trailing streamline conditions were investigated for each grid type in the present numerical scheme.

The equal velocity condition is implemented as follows for a single element section. The velocity at a point on the surface of a single element section is given by

$$V = \frac{\gamma^{1/2}\psi_\eta^T}{J} = \frac{\gamma^{1/2}}{J}\left[\psi_\eta^1 \cos\theta + \psi_\eta^2 \sin\theta + \lambda\psi_\eta^3\right] \qquad (34)$$

where the ψ_η^i are found using one sided second order finite difference formula. Expressions for V, containing the parameter λ are found for points near the trailing edge on the upper and lower surface. Using one, two, or three neighbouring points, an extrapolation is made on each surface to obtain an expression for the velocity at the trailing edge. As the extrapolated trailing edge velocity is to be the same for both the upper and lower surface, an equation results which gives λ explicitly in terms of the base solution derivatives and θ . The extrapolation formula

takes one of the forms (Thompson [24])

$$V^{TE-1} = V^{TE} = V^{TE+1} \tag{35a}$$

$$2V^{TE-1} - V^{TE-2} = V^{TE} = 2V^{TE+1} - V^{TE+2} \tag{35b}$$

$$3V^{TE-1} - 3V^{TE-2} + V^{TE-3} = V^{TE} = 3V^{TE+1} - 3V^{TE+2} + V^{TE+3} \tag{35c}$$

where the superscripts indicate the position relative to the trailing edge as shown in Figure 19. The first condition, equation (35a), results in a stagnation point at the trailing edge, the zero velocity condition. The second condition, equation (35b), represents a linear extrapolation to the trailing edge velocity, while the third expression, (35c), results from a quadratic extrapolation. Thompson found a slight improvement in accuracy for O-type grids using the quadratic scheme. A similar result occurs for the C-type grids due to the identical nature of the grid near the trailing edge for these two mappings. For the S-type grids, it was necessary to re-examine this problem, where a similar improvement was found.

For the 2S-type grids the parameters λ_1 and λ_2 are found by extrapolations to the two trailing edge velocities on the two components. This results in equations of the form

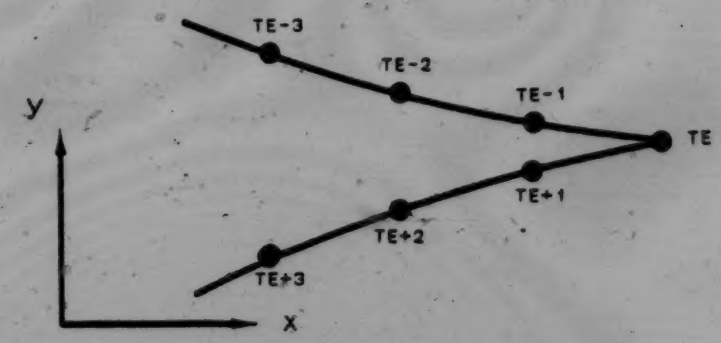

a) physical plane

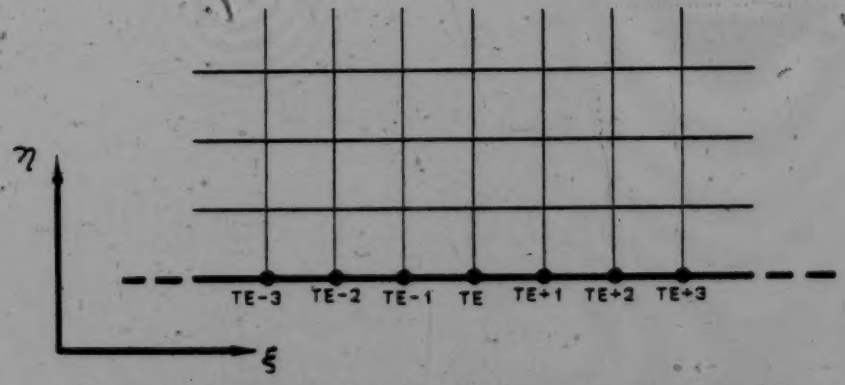

b) transformed plane: O-type, C-type grids

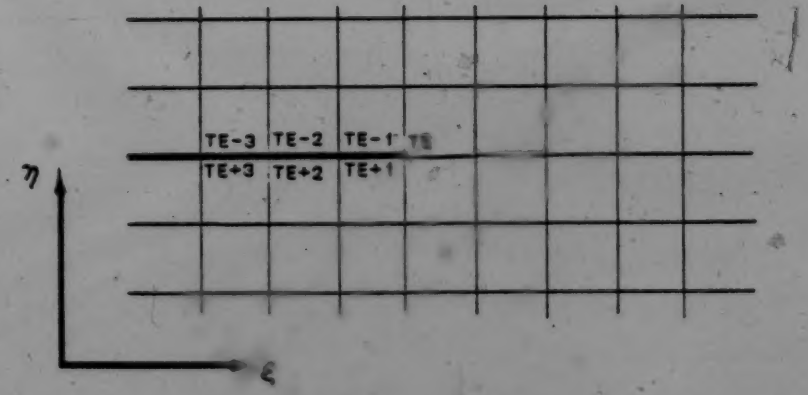

c) transformed plane: S-type grids

Figure 19 Trailing Edge Points For Velocity Kutta Condition

$$C_1^M \lambda_1 + C_2^M \lambda_2 = C_3^M \tag{36a}$$

$$C_1^F \lambda_1 + C_2^F \lambda_2 = C_3^F \tag{36b}$$

where the C_i^M and C_i^F refer to main and flap sections, and are formed from the derivatives of the basic solutions ψ^1, ψ^3, and ψ^4 at the extrapolation points and the desired flow angle θ.

The trailing streamline condition was implemented only for the O- and C-type grids. The velocity vector at a computational node (eg. the trailing edge) is given by

$$\bar{V} = u\bar{i} + v\bar{j}$$

and the bisector at the trailing edge is given by

$$\bar{b} = b_1\bar{i} + b_2\bar{j}$$

If the velocity vector and bisector coincide, then

$$\bar{V} \times \bar{b} = 0$$

hence

$$ub_2 - vb_1 = 0 \tag{37}$$

For the O- and C-type grids, on the airfoil surface $\psi_\xi = 0$ and

the velocity components are given by equation (32). Using the full expression, equation (27), for ψ^T, equation (37) reduces to

$$\lambda = - \frac{\psi_\eta^1 \cos\theta + \psi_\eta^2 \sin\theta}{\psi_\eta^3} \qquad (38)$$

This is a much simpler expression than the equal velocities method, as only three finite difference derivatives need to be evaluated at the trailing edge. Moreover, the grid is most dense at the trailing edge, so that accuracy is maintained. For the S-type grids a similar expression does not result, due to the multi-valued coordinate mapping on the slit at the trailing edge, and recourse must be made to the velocity condition.

The implementation of the Kutta condition was found to be the most critical aspect of the present work. None of the methods described above were found to be applicable on all four grid types. In general, the velocity conditions worked best in the S- and 2S-type grids, while the trailing point condition worked best for the O- and C-type grids.

Lift and Moment Calculations

The force system on the airfoil is shown in Figure 20. The chordwise force coefficient C_x is negative for positive angles of attack in an unbounded, inviscid flow so that the

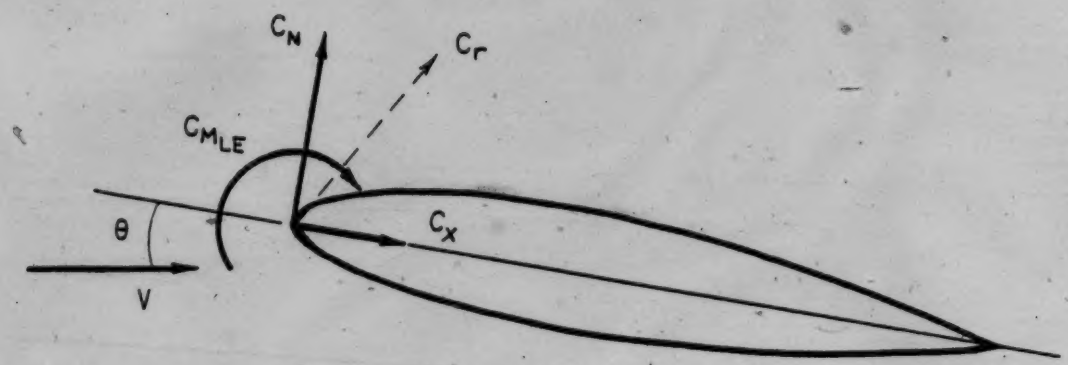

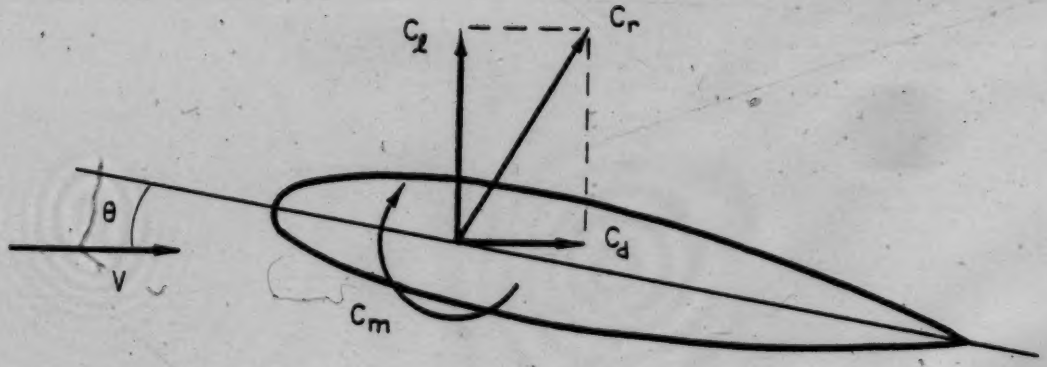

Figure 20 Airfoil Force System

resultant force, C_r , is perpendicular to the free stream. The force and pitching moment coefficients are found by integration of the pressure distribution, which can be done in several ways. In the present work, these integrations were performed in the physical plane using the relations (see Houghton and Brock [27])

$$C_N = \int_0^1 \left[C_{P_\ell} - C_{P_u} \right] dx \tag{39a}$$

$$C_X = \int_{y_{min}}^{y_{max}} \left[C_{P_f} - C_{P_a} \right] dy \tag{39b}$$

$$C_{M_{LE}} = \int_0^1 \left[C_{P_e} - C_{P_u} \right] x \, dx \tag{39c}$$

to obtain normal and chordwise force coefficients, and the leading edge pitching moment coefficient. The contribution to the leading edge pitching moment due to chordwise forces was ignored, as it is very small. The integrations were carried out using the trapezoidal rule. The force components were resolved to give the lift, drag, and quarter chord pitching moment coefficients using

$$C_\ell = C_N \cos\theta - C_X \sin\theta \tag{40a}$$

$$C_d = C_N \sin\theta + C_\chi \cos\theta \tag{40b}$$

$$C_m = C_{M_{LE}} + \frac{C_N}{4} \tag{40c}$$

These coefficients may also be evaluated directly in the transformed plane using the expressions

$$C_\ell = -\int_1^N C_p \left[x_\xi \cos\theta + y_\xi \sin\theta \right] d\xi \tag{41a}$$

$$C_d = \int_1^N C_p \left[y_\xi \cos\theta - x_\xi \sin\theta \right] d\xi \tag{41b}$$

where the integrals may be easily evaluated using either the trapezoidal or Simpson's rule over the N coordinate points which define the airfoil surface. Thompson [24] used this procedure for O-type grids, noting that accuracy deteriorated using Simpson's rule.

The resultant force coefficient may be obtained by the calculation of the circulation, Γ , around the section which is defined by

$$\Gamma = -\oint \bar{V} \cdot d\bar{s}$$

where the circulation has been normalized with respect to

V_c . For the O-type grid the line integral is evaluated in the transformed plane on a line of constant η which is the map of a closed curve in the physical plane. The integral becomes

$$\oint \bar{V} \cdot d\bar{s} = - \int_1^N \frac{1}{J} \left[\gamma \psi_\eta - \beta \psi_\xi \right] d\xi \qquad (42)$$

All derivatives in the integrand are evaluated by second order central difference expressions on the η -line nearest the airfoil surface and the integral is evaluated with the trapezoidal rule using Romberg improvement. Other integration schemes (Simpson's rule and spline integration) were investigated, with no appreciable improvement in accuracy. The force coefficient, C_r , is found using

$$C_r = - 2 \oint \bar{V} \cdot d\bar{s} \qquad (43)$$

This procedure provides another check on the lift calculation, but was not implemented in the C- or S-type grids.

Both the force and pitching moment coefficients for the bounded flow solution are then compared with the free field solution to obtain the necessary tunnel corrections ΔC_ℓ, and ΔC_m . The calculated drag coefficient should be zero, since inviscid flow is assumed, and serves as an accuracy check on the numerical procedures. In the present work, the free stream values were obtained using the singularity method of Kennedy [13] for the calculation of the surface pressure

distribution, which was then integrated in the same manner as the present numerical scheme. Kennedy's method was used to obtain free field values because the present numerical results were limited by the maximum grid size which could be accomodated in the computer memory, thus limiting the distance to the outer boundary, and making it difficult to implement truly unbounded flow conditions.

C. Numerical Implementation

The grid generation and potential flow solutions were accomplished by iteration using successive over-relaxation (SOR). All partial differential equations were discretized using second order central difference expressions throughout the solution. Initial values for the solutions were supplied by linear interpolation along constant coordinate lines between known boundary values. Optimum relaxation values, which depended on several factors, were determined empirically by observation of convergence rates as shown in Figure 21 or Figure 22. For each grid type, optimum relaxation parameters were found for a variety of grid sizes, geometries, boundary point distributions, and grid control amplitude. Typical values, shown in Table 3, are slightly conservative but are applicable to a widerange of grids of each type. Thompson [21] gives an algorithm for optimally varying the relaxation over the grid. This algorithm was not used in the present work, due to the capacity of the computer used, and a constant relaxation

Table 3 Relaxation Parameters for Optimum Convergence

Grid Type	Size	Relaxation Factor, W
O	61 X 60	1.92
	100 X 100	1.94
C	100 X 30	1.50
S	139 X 75	1.87
2S	99 X 80	1.70

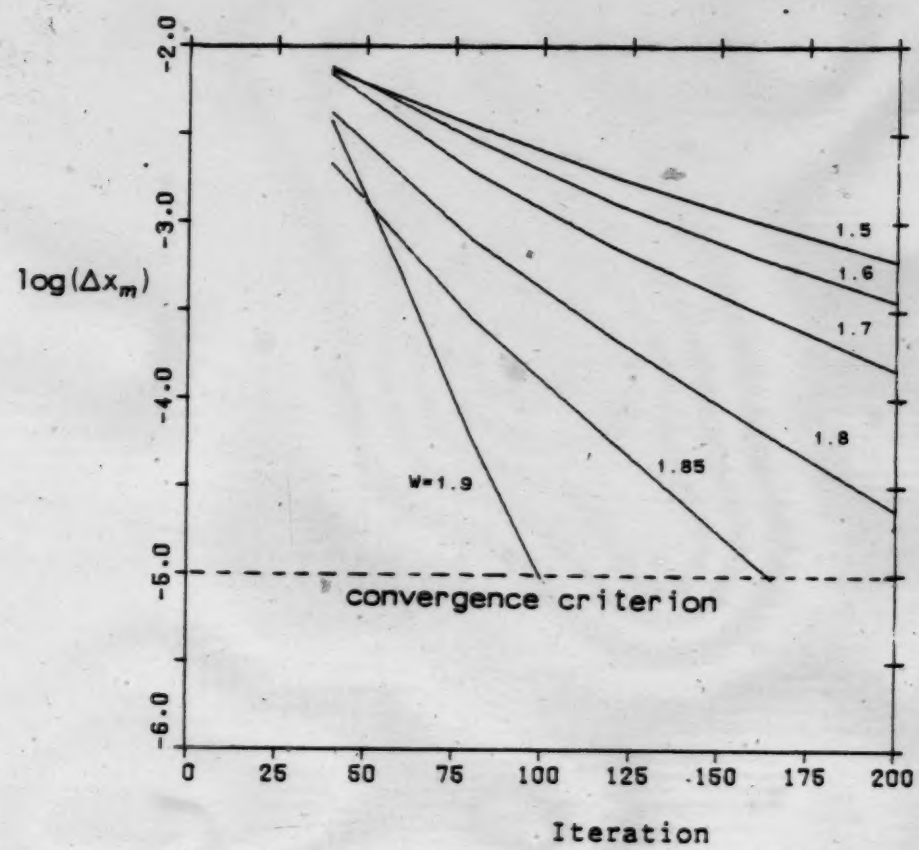

Δx_m = largest change on grid between iterations

Figure 21 Effect of Relaxation Parameter on Convergence Rates for an O-Type Grid

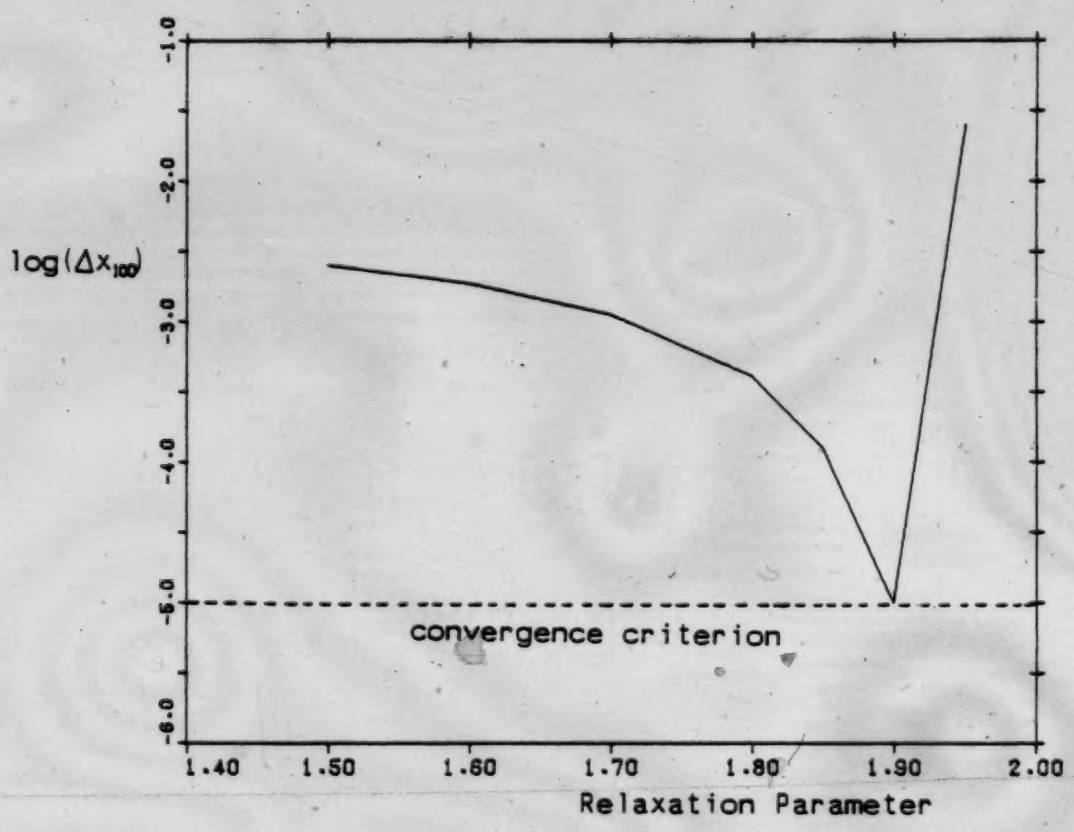

Δx_{100} = largest change on grid at 100 iterations

Figure 22 Determination of Optimum Relaxation Parameter for an O-Type Grid

factor was used throughout the grid. Convergence was assumed when the maximimum change of the solution on the grid was less than some prescribed value. Thompson [24] showed that for O-type grids, force coefficients within 1% accuracy were obtained using convergence criteria of 10^{-4} for grid generation and 10^{-5} for potential flow solutions. In the present work, these criteria were decreased an order of magnitude. This did not involve a substantial increase in computer time, as seen in Figure 21. However it was determined that for large grids (in the physical space) the single precision round-off error during grid generation was near $5*10^{-4}$, and the convergence criterion was adjusted accordingly. Moreover, the largest change on the grid at convergence occurs where the grid is coarsest, so the relative error remained small.

The boundary conditions for the C- and S-type grids lend themselves to solution by line successive over-relaxation (LSOR). This is a semi-implicit method which generates improved solution values along an entire η line in the computational grid by the solution of a tri-diagonal matrix. This is similar to the alternating direction implicit method (ADI), and an attempt was made to utilize the complete ADI method in the solutions. However, the presence of the cross-derivative term in the partial differential equations was a complicating factor: the standard sequences of acceleration parameters associated with ADI solutions of elliptic equations failed to perform

as expected. Although convergence was initially accelerated in certain test cases, the performance of the algorithm did not justify the additional programming effort. Use of LSOR for the same test cases with the cross-derivative terms showed substantial reductions in computer time and iterations to convergence compared to SOR. Henceforth, all S-type grid solutions were performed using LSOR.

Some difficulty was encountered in the numerical solutions when a high degree of grid control was used. This was likely due to the large error which was sometimes present in the initial solution values. During the initial iterations, the grid adjustments were so large that the grid would fold back on itself and the ensuing calculations would fail. It was determined that the most reliable method of grid generation was then obtained when both the relaxation parameter and grid control amplitude were initially set low (W=1.3 and amplitude zero) and subsequently increased in steps as the solution progressed. These adjustments were made automatically when the largest change on the grid was less than some value, usually 10^{-1} . Once the final values for relaxation and grid control were reached the solution continued until convergence was obtained.

It is customary in numerical work to report such statistics as computer time. The University of Alberta Department of Computing Services currently (spring, 1982) operates an Amdahl 470/V8 mainframe on a time sharing basis using the Michigan Terminal System (MTS). The numerical

solutions were performed on a Floating Point Systems AP-190L array processor, hosted by the Amdahl. Exact timing statistics are meaningless unless accompanied by a lengthy discussion of the architecture and operating systems of the two machines, and the details of the object code implementation. As a rough guideline, the Amdahl execution speed is approximately 6.5 million instructions per second, while the array processor, in the configuration used, is slightly slower. Typical execution times were several minutes on the array processor and several seconds on the host Amdahl. A large portion of the host CPU time was used for disk I/O activity. The somewhat slower array processor was used because of the lower cost involved, a factor of 40 less than the Amdahl. The array processor performed only the numerical solutions, while all the auxiliary calculations, plotting, and execution-time adjustments were performed by the Amdahl. Some of the O-type and C-type grid solutions could not be implemented efficiently due to difficulties in operating the array processor, which was under development at the time.

D. Data Interpretation

In the words of Hamming [28], "The purpose of computing is insight, not numbers." In the present work, where a typical grid contained over five thousand computational nodes, with up to fourteen variables defined at each node, data analysis and interpretation was possible only by means

of the extensive graphics capability of the computing system. Roughly half the host computer time was used in the generation of graphic displays of the data. The solutions sought here are smooth, due to the nature of the Laplace equation, and discontinuities in any part of the solution became quickly evident when displayed graphically. Suitable adjustments (eg. the boundary point distribution and implementation of more grid control) could then be made to increase the overall suitability of the grid, and accuracy of the solution.

For the grid generation, it was generally possible to determine when an adequate grid was obtained by merely plotting it, although some very good looking grids sometimes provided extremely poor results. A more quantitative approach, as suggested by Kerlick and Klopfer [22], involves re-arranging the metrics into the physically more meaningful parameters representing cell orientation, orthogonality, cell aspect ratio, and cell size. The cell orientation in the physical plane, for example, the rotation of the tangent to an η line from the x axis, is given by the angle δ where

$$\cos\delta = \frac{x_\xi}{(x_\xi^2 + y_\xi^2)^{1/2}} = \frac{x_\xi}{\gamma^{1/2}}$$

The orthogonality (or lack thereof) of the grid is characterized by the angle Θ between the ξ and η grid lines, where

$$\cos\theta = \frac{\beta}{(\alpha\gamma)^{1/2}}$$

The cell aspect ratio, a, is the ratio of the magnitudes of the tangent vectors to the ξ and η lines at each grid node:

$$a = \left(\frac{\alpha}{\gamma}\right)^{1/2}$$

Finally, the Jacobian represents the area in the physical space of a single cell in the computational space. One way to observe these properties is to plot perspective surface drawings for the metrics and grid properties as shown in Figures 23 to 28 for the S-type grid shown in Figure 16b. In these plots it is very easy to observe areas of the grid where the properties vary rapidly and to make adjustments to the grid accordingly. Particular areas of importance are near the section leading and trailing edges. Figures 23 and 24 indicate rather extreme grid behavior at the section leading and trailing edges. Figure 26 illustrates the smoothness of cell size variation near the model. Figure 27 indicates the maximum non-orthogonality (less than 1 degree from orthogonality) occurs well upstream of the model, and that near the model the orthogonality is quite uniform. Finally, Figure 28 shows that the η -line spacing is approximately 3 times the ξ -line spacing near the airfoil leading and trailing edges.

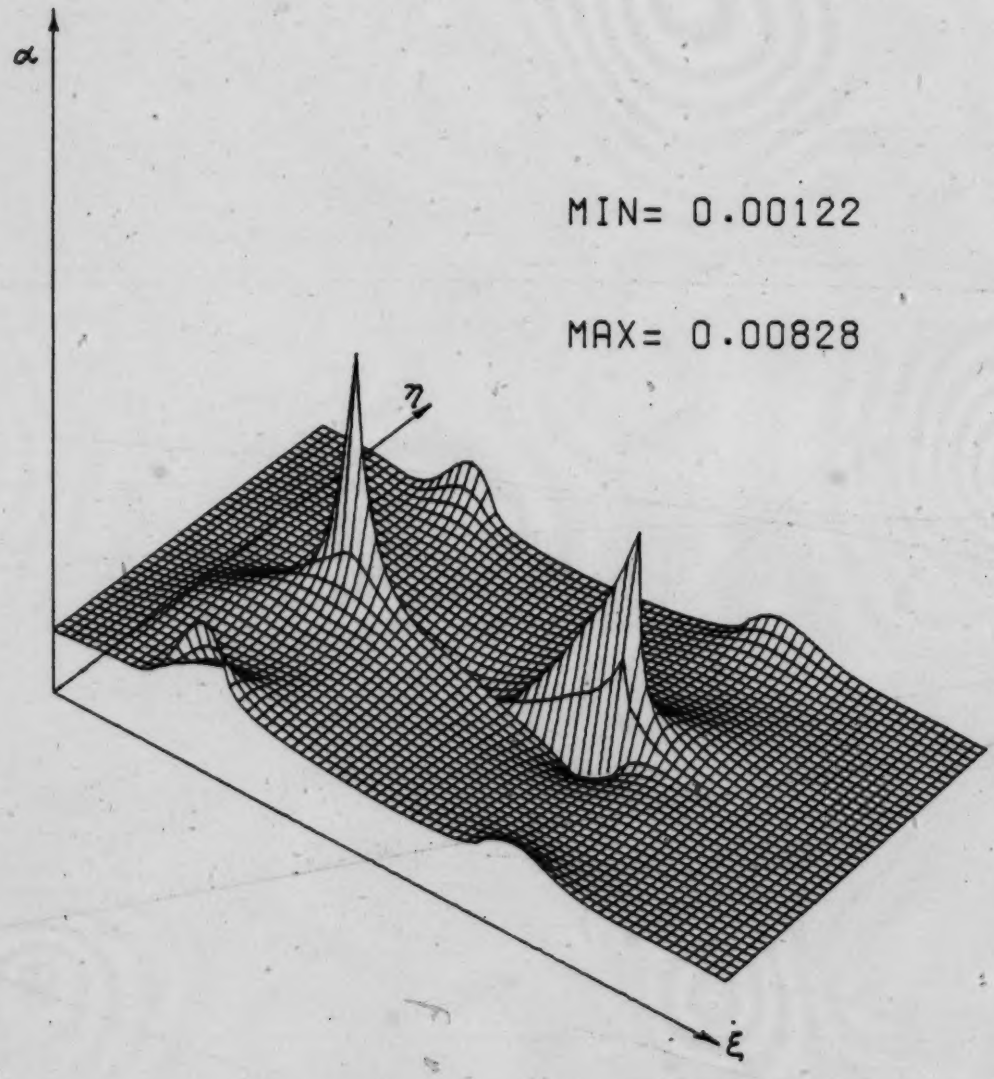

Figure 23 S-Type Grid Alpha Surface Plot

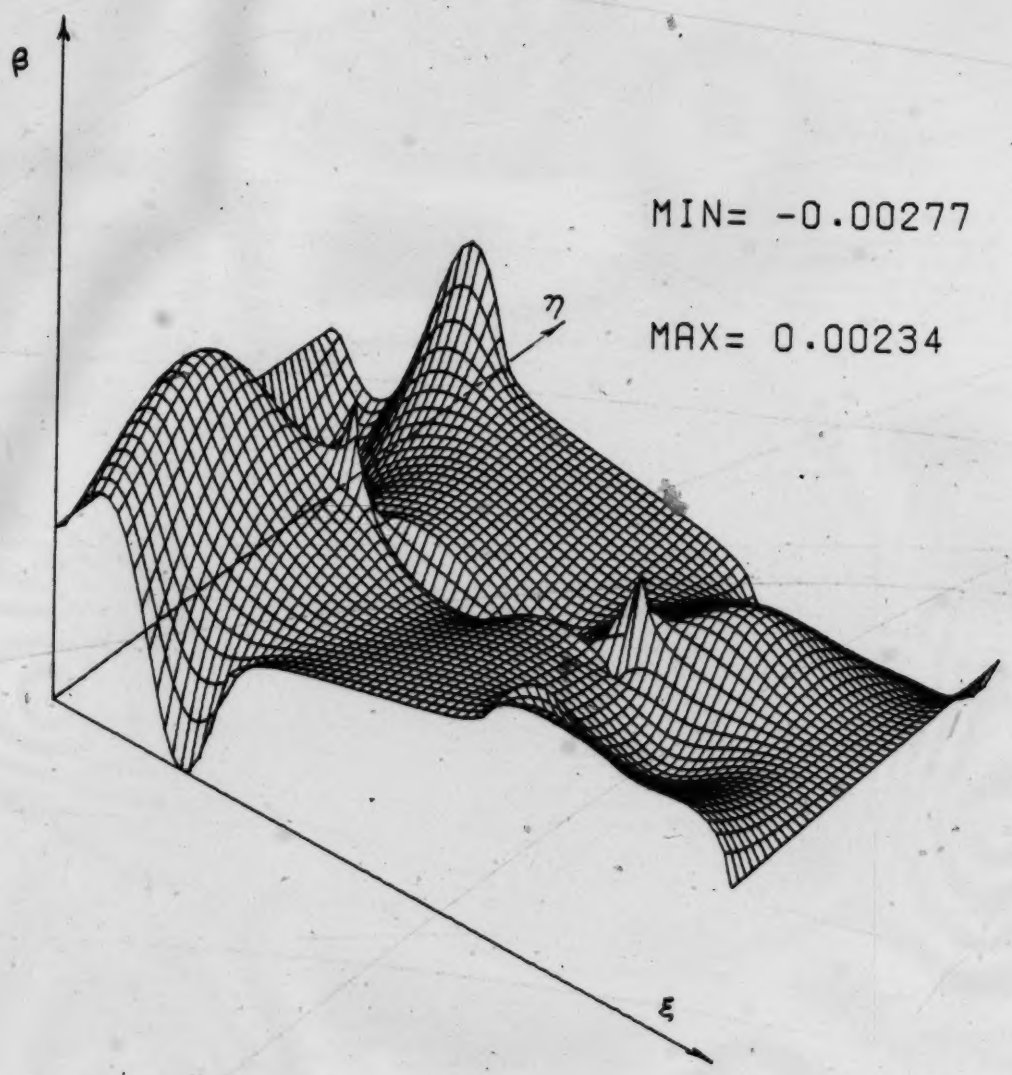

Figure 24 S-Type Grid Beta Surface Plot

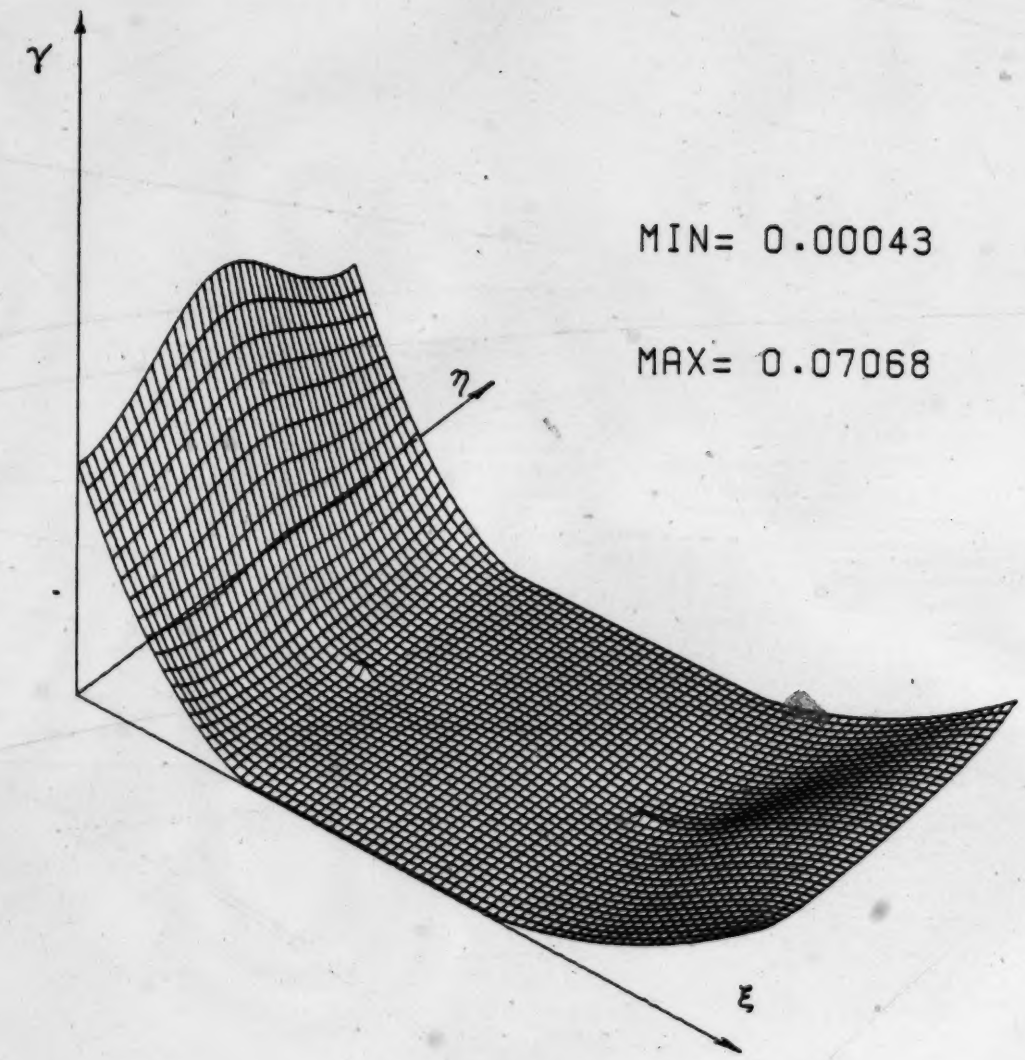

Figure 25 S-Type Grid Gamma Surface Plot

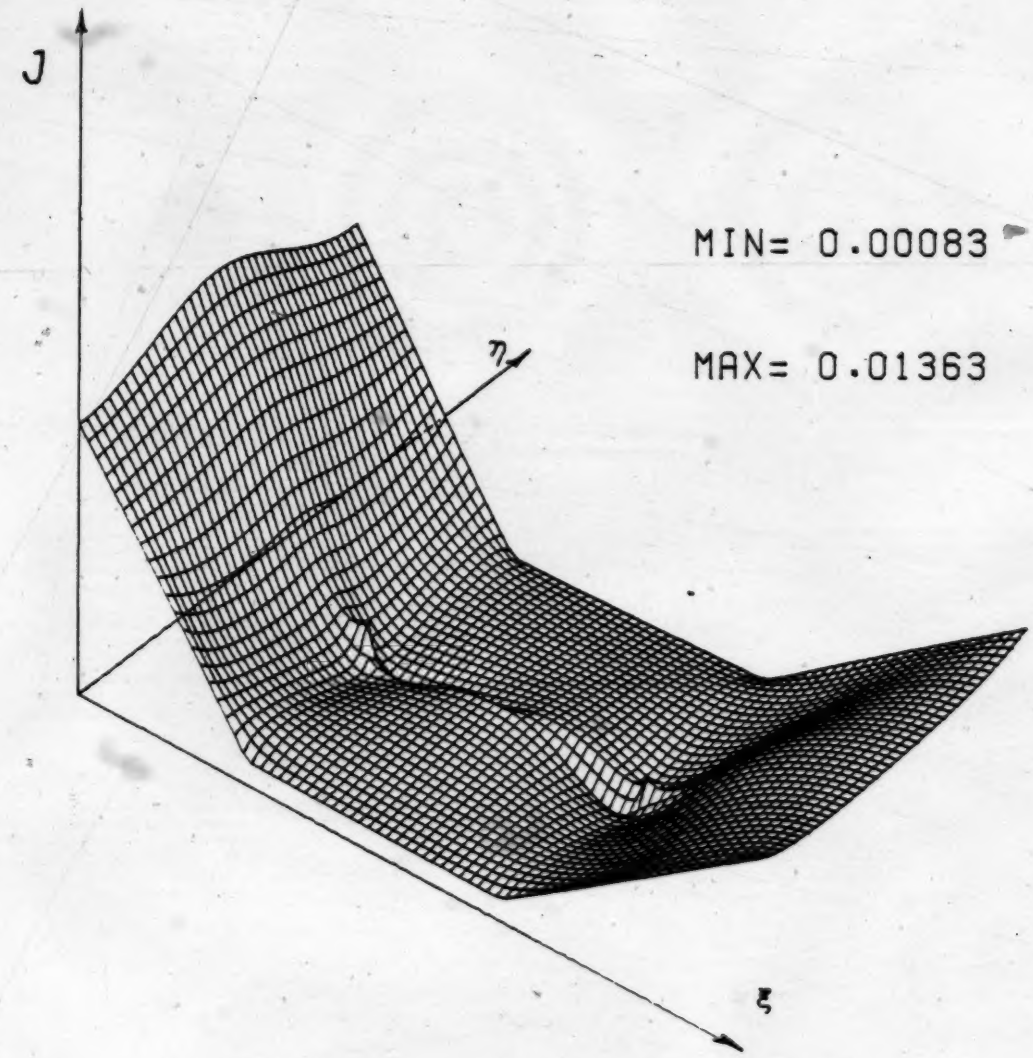

Figure 26 S-Type Grid Jacobian Surface Plot

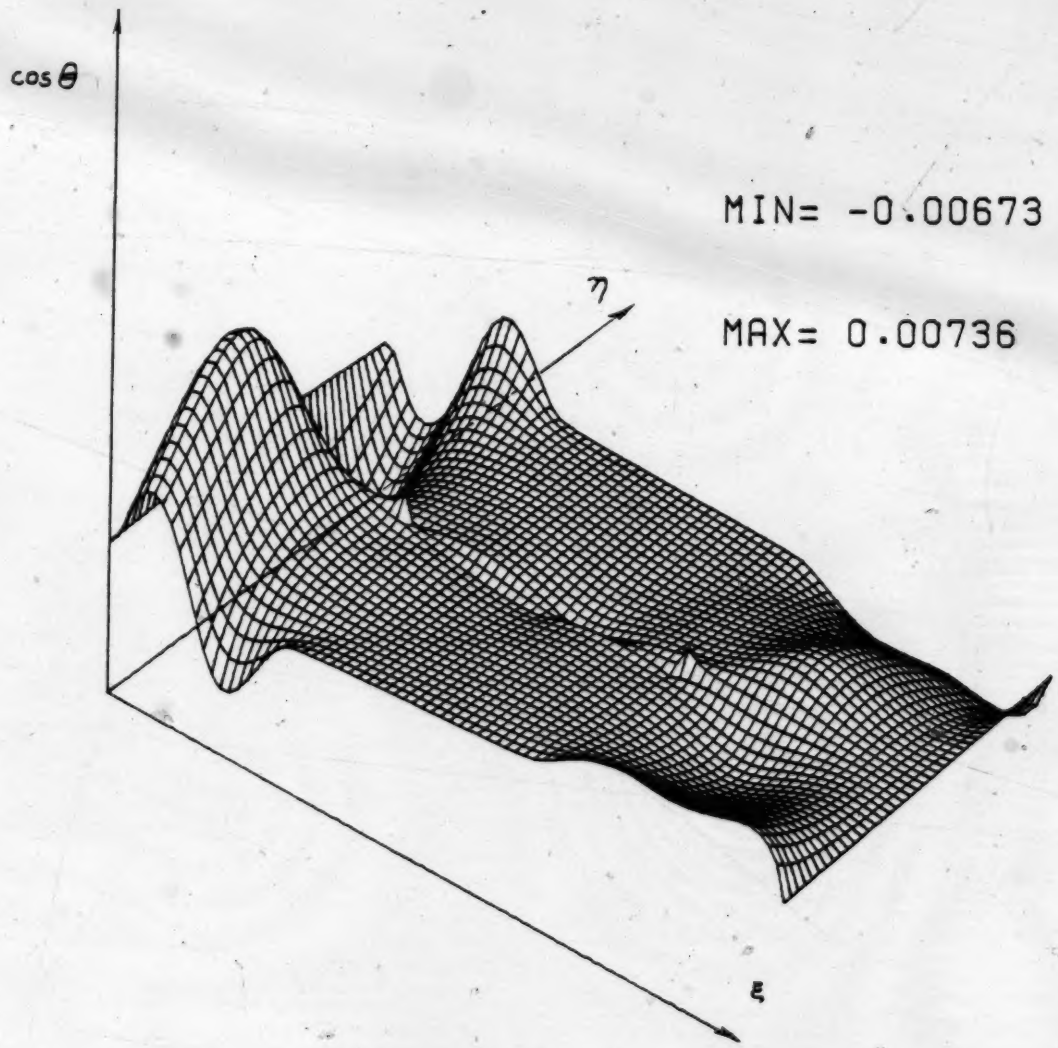

Figure 27 S-Type Grid Orthogonality Surface Plot

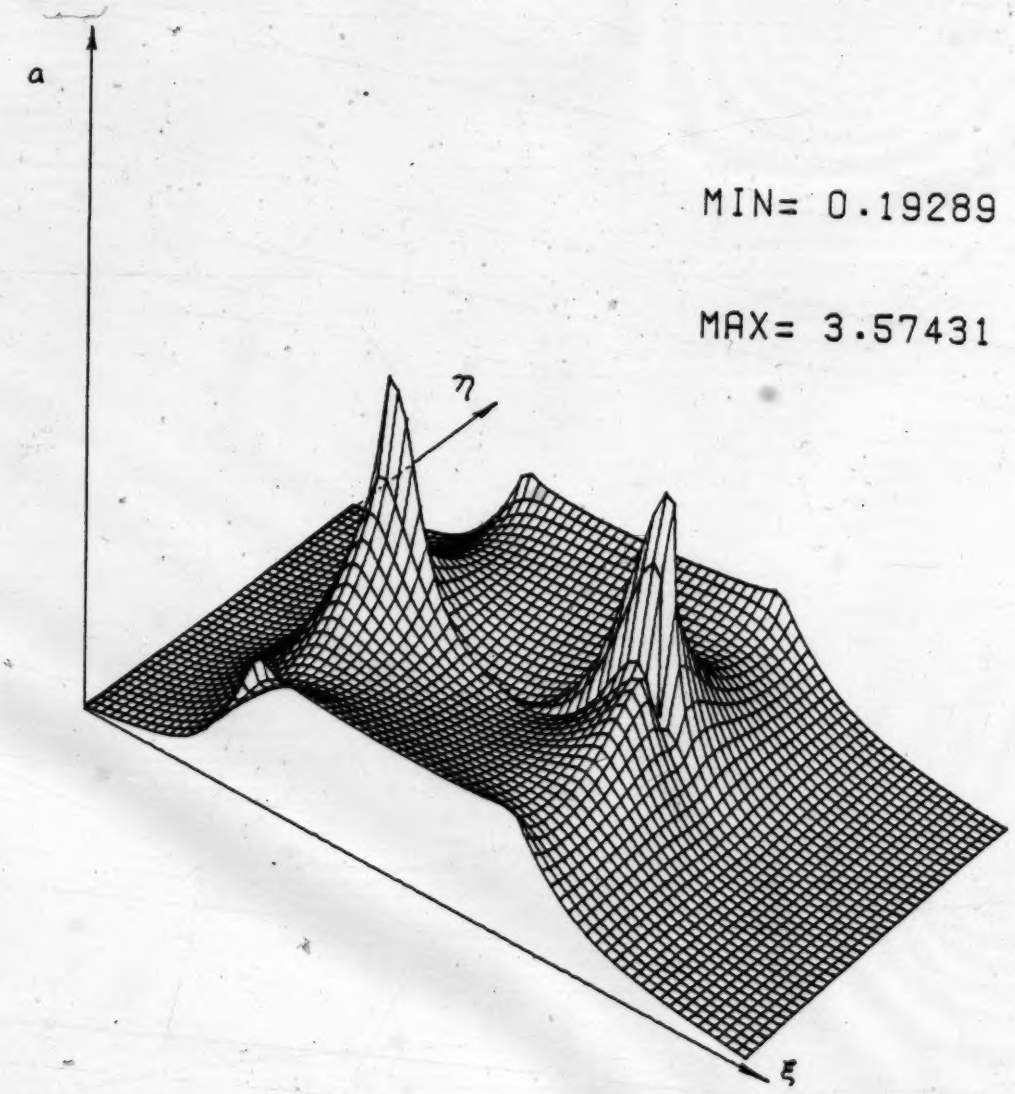

Figure 28 S-Type Grid Aspect Ratio Surface Plot

Other graphical procedures involved the contour plotting of the solutions in the physical plane. For the stream function, these contours are the flow streamlines. Examples are shown in Figures 29 to 31 of the three basic solutions for a single element section, with the total flow shown in Figure 32. Only part of the solution field is shown in these Figures: the outer boundary was five chord lengths away. These Figures were generated using an O-type grid and the position of the re-entrant line is indicated, showing the solution continuity across this line.

Other data may be extracted from the solutions. Figure 33 shows the pressure coefficient contours through a wind tunnel contraction, constructed using two cubic profiles (a standard contraction shape), which clearly shows a velocity defect near the tunnel centre line at the test section entrance. Such data could be useful in contraction design. These examples show only a sample of the types of data which may be extracted from the potential flow solution using field techniques.

E. Accuracy of BFC Solutions

The O-type grid is most suited to geometries where the outer boundary is a large distance away from the inner boundary. For the wind tunnel geometry, where the solution domain is long and thin, the O-type grid is very coarse and highly skewed near the upstream and downstream boundaries.

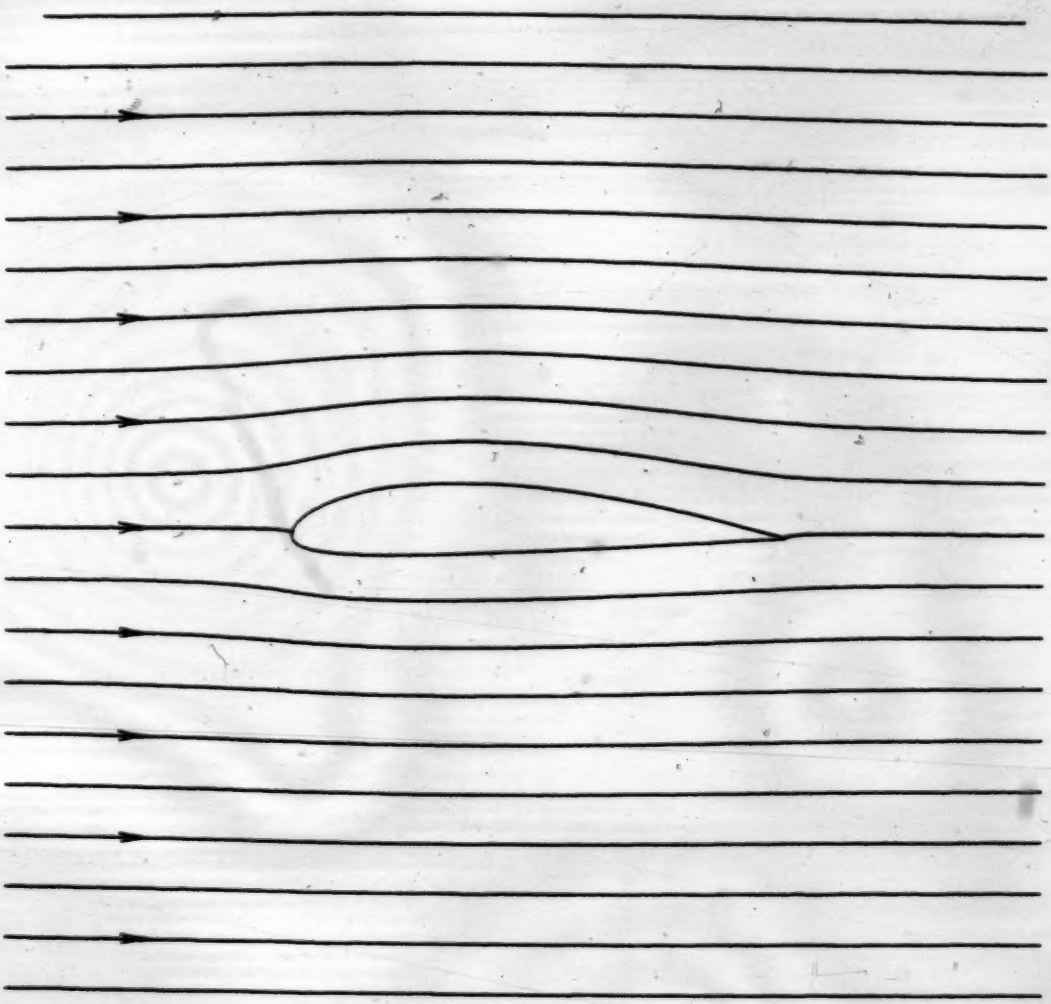

Figure 29 Stream Function Contours - Uniform Stream at Zero Degrees (No Circulation)

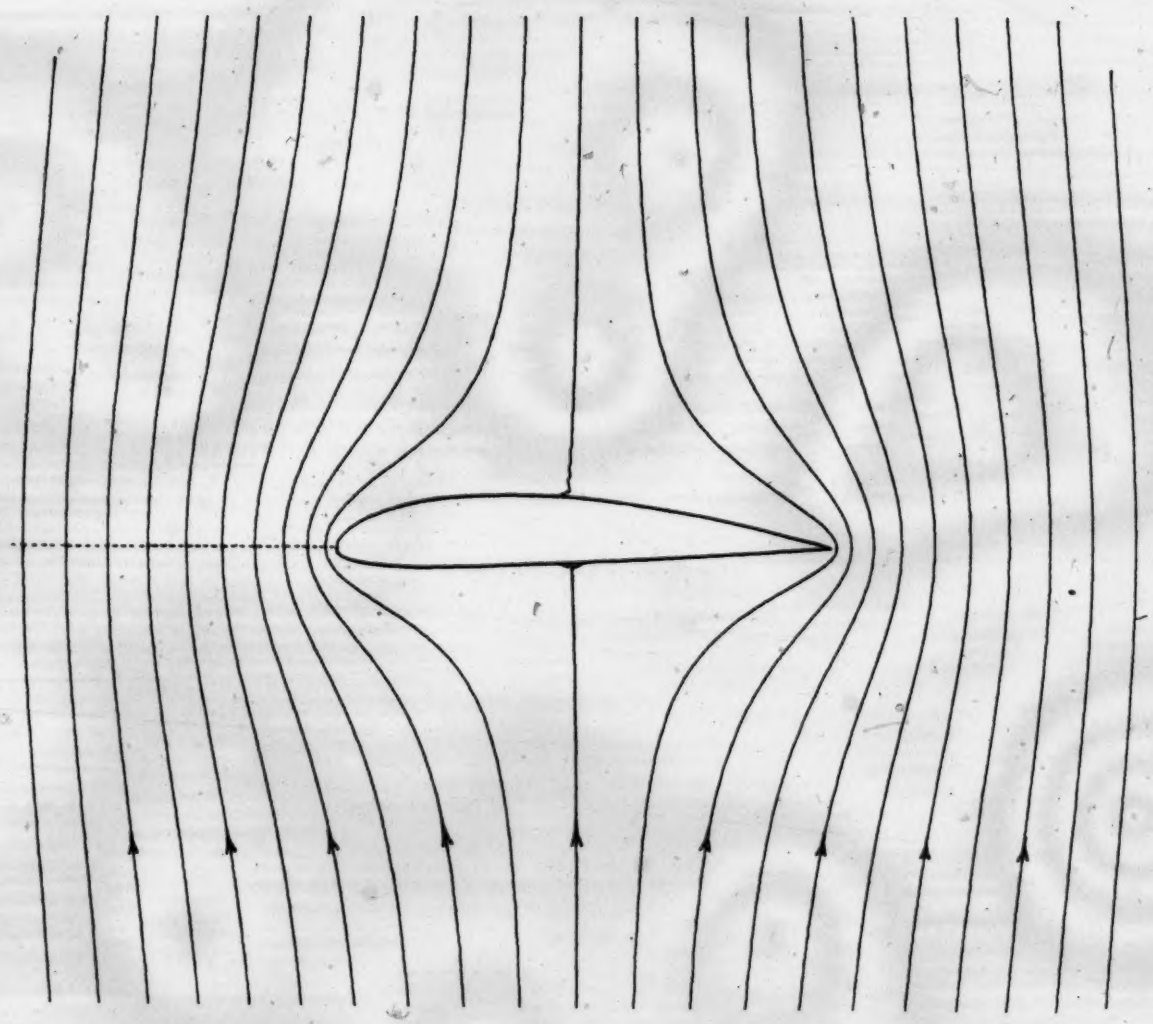

..... Re-entrant line

Figure 30 Stream Function Contours - Uniform Stream at Ninety Degrees (No Circulation)

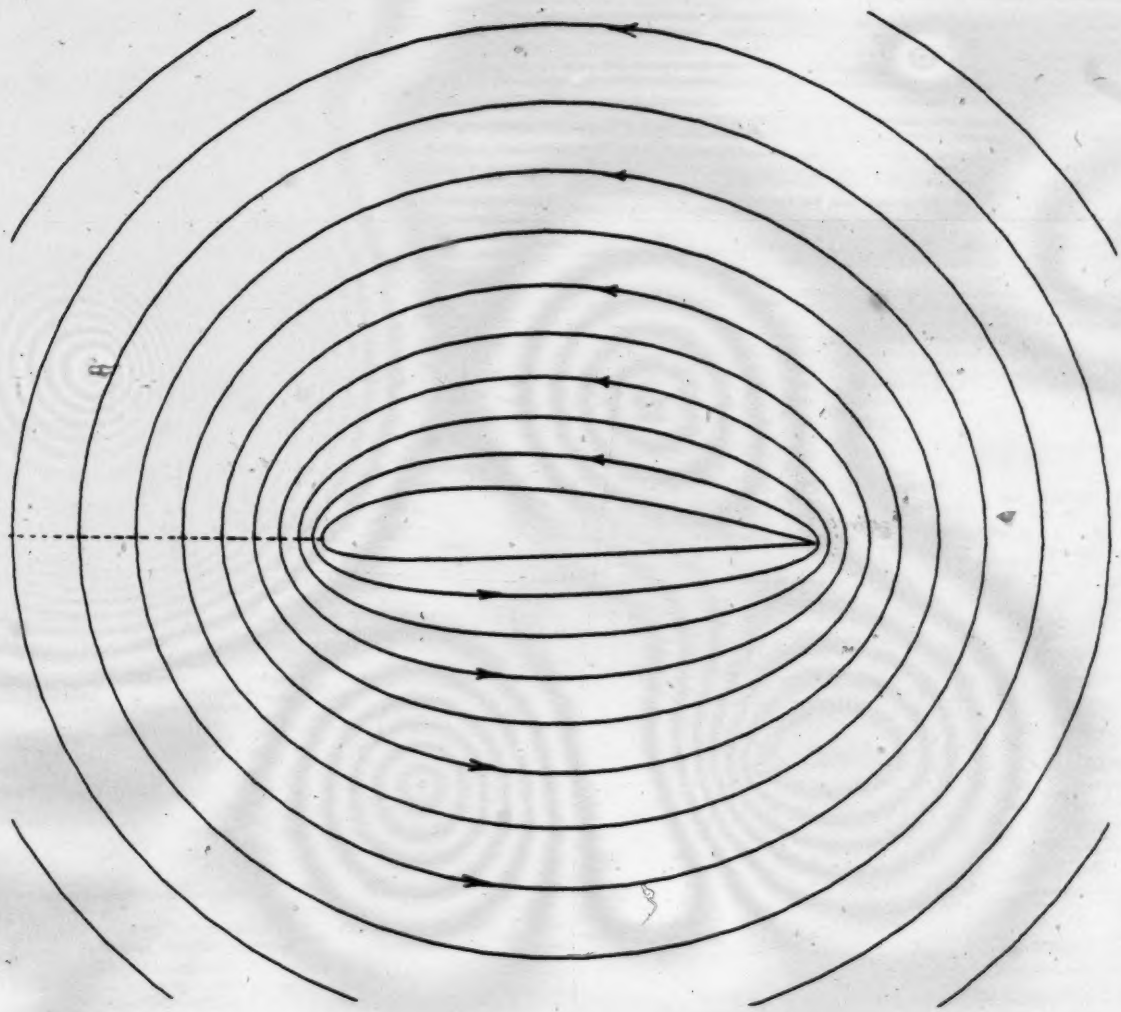

-------- Re-entrant line

Figure 31 Stream Function Contours - Circulatory Flow

--------- Re-entrant line

Figure 32 Stream Function Contours - Total Flow at 20 Degrees Incidence

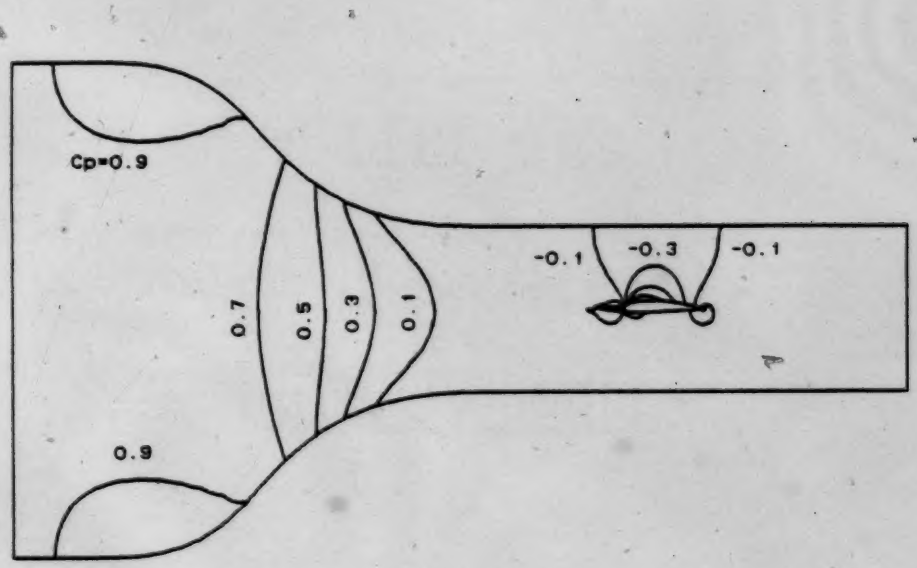

Figure 33 Pressure Coefficient Contours through a Contraction Using a C-Type Grid

The C-type grid, although adequate upstream of the model, is equally unacceptable downstream. Solutions were obtained, however, using the O-type grid for the case of distant boundaries, to test the validity of the trailing point Kutta condition, equation (38) and the integration routines for the calculation of the aerodynamic coefficients from the pressure distribution.

Thompson [24] has investigated the use of the O-type grid for potential flow solutions for two Karman-Trefftz sections. His investigation included the effects of the required distance to "infinity", the boundary point distribution, and use of grid control, and utilized the velocity Kutta condition only. However, in the present work, it was found impossible to implement the velocity condition for a section with a sharp trailing edge, whether cusped or wedge shaped, using the O-type grid. This is thought to be due to the extreme distortion of the grid at the trailing edge, as shown in Figure 34a. Careful examination of the sections used by Thompson in [24] revealed that the sections were modified to give a rounded trailing edge, by increasing slightly the radius of the circle used to generate the sections. The grid around the modified trailing edge, shown in Figure 34b, is much more suitable for calculation of the surface derivatives necessary for the velocity condition implementation, and explains the success of Thompson's calculations. Since the airfoil camber does not change by using the enlarged circle, the developed lift is the same.

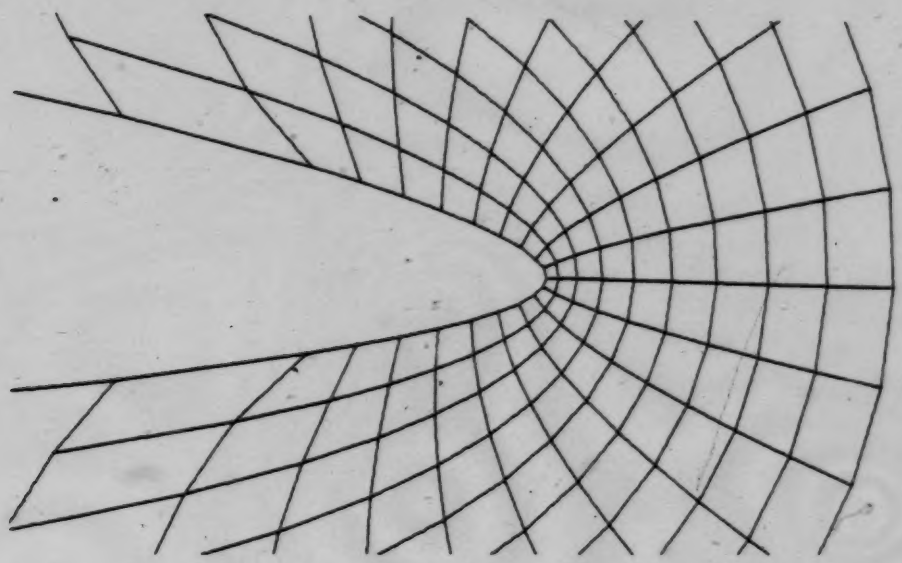

b) rounded trailing edge of Thompson, [24]

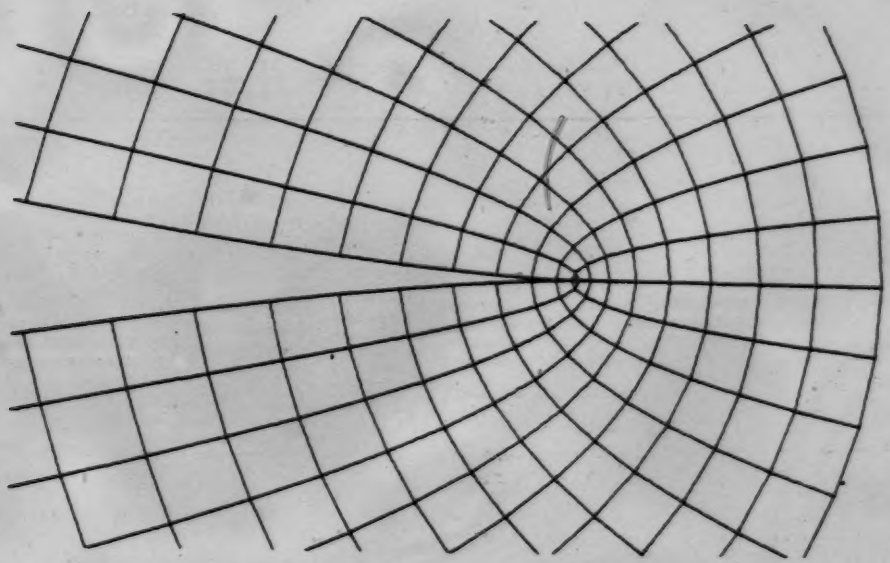

a) sharp trailing edge

Figure 34 O-Type Grid Trailing Edge Details

Thompson indicates that results within 1% of the analytical solution are readily obtained.

The procedure of artificially rounding the trailing edge is unsuitable for the present case, where the section shape is specified. Calculation of the circulation using the trailing Kutta condition proved to be a satisfactory alternative for these sharp trailing edge sections in an O-type Grid. Using a Joukowski section, a comparison was made using the present method with the trailing condition and the singularity method of Kennedy. This was an extreme case, as the Joukowski section was cusped. The same number of surface points were specified for both calculations, results of which are given in Table 4, along with the theoretical values. It is observed that the present method and the singularity method under-predict the lift at high angle of attack. In the range for which unseparated flow might be expected to occur, the lift coefficients obtained using the two methods differ by less than 1%, although the absolute error from the analytic solution is nearly 4%.

It was difficult to assess the accuracy of the solutions using the S-type grids. These results might be expected to be most accurate when the grid is dense and uniform near the model. Since the maximum grid size was limited by computer resources, this fine packing of the grid was accomplished best by bringing the outer boundary towards the model. This meant implementation of the far-field boundary conditions uncomfortably close to the model, and in

Table 4 Comparison of Numerical Solution with Singularity Solution of Kennedy [13]

Section: Joukowski 30% thick, symmetrical

30 points each surface

numerical "infinity" at 25 chord lengths from section mid-chord

Angle of Attack (degrees)	Analytic solution	Singularity solution (Kennedy)	Numerical solution
0	0.0	0.0	0.0012
2	0.2699	0.2603	0.2616
4	0.5395	0.5203	0.5217
6	0.8085	0.7797	0.7811
8	1.0764	1.0382	1.0396
10	1.3431	1.2953	1.2969
12	1.6081	1.5509	1.5525

fact represents the wind tunnel problem itself, for which there are few exact solutions. The exact solution of Tomotika for a flat plate in a wind tunnel, mentioned by Garner [1], would not include the blockage effect, which is known to interact with the lift interference. The results of de Vries and Schipholt [15] could not be checked, as the two element section profile used in [15] was not specified. The results of Williams and Parkinson [2], which utilized a singularity method for the wind tunnel problem, were available for comparison with the S-type grid results. Using a 14% Clark-Y airfoil zero incidence, the lift was calculated for a range of tunnel heights. The results, Figure 35, indicate comparable accuracy of the finite difference solution with the singularity method used in [2].

For the wind tunnel problem, solution accuracy was dependent on the extent of grid control. The O-type solutions were much more sensitive in this respect than the S-type grids and for the tunnel geometries the S-type grids were used exclusively. With experience, the degree of grid control necessary for an accurate solution, which depended on several parameters (grid size, tunnel geometry, section profile, etc.), was determined by trial and error, using the metric plots described previously.

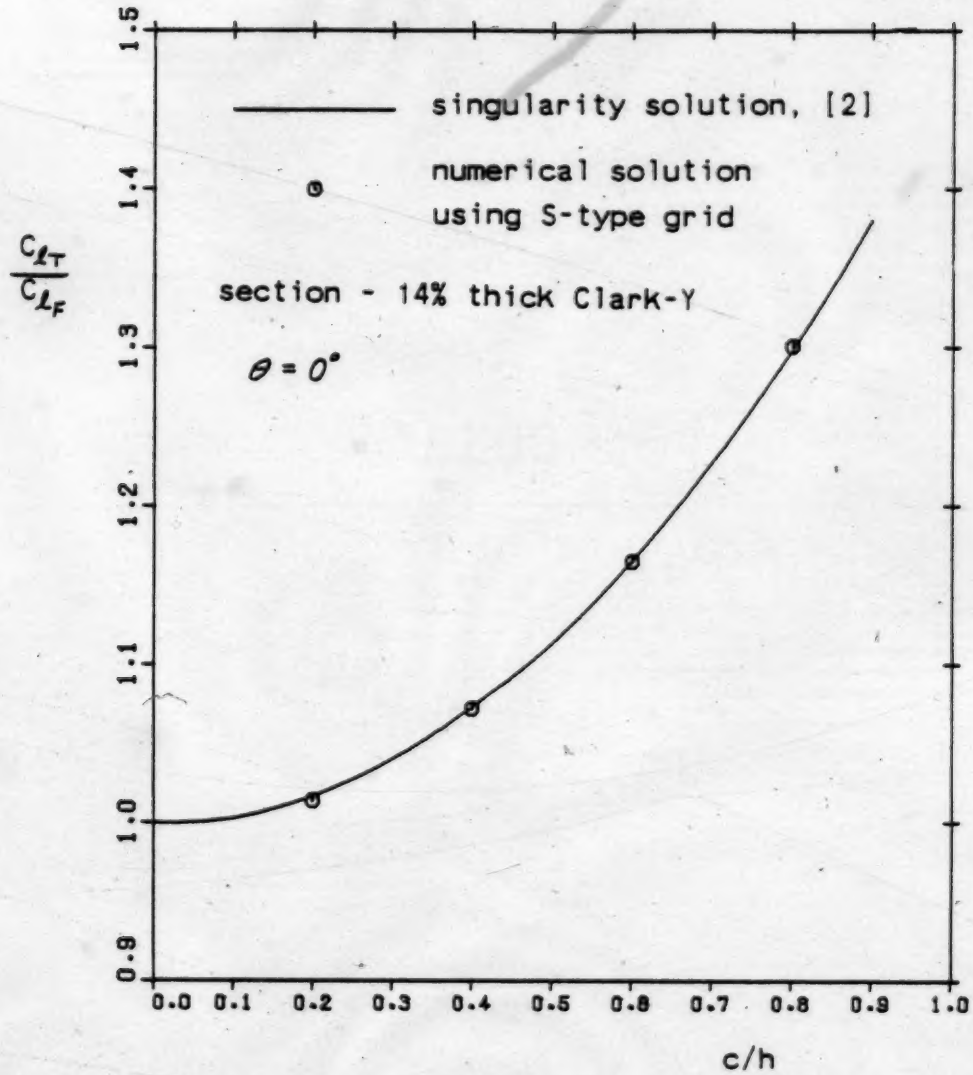

Figure 35 Comparison of S-Type Solution With Singularity Solution for a Wind Tunnel Geometry

F. Conclusion

For the present application to the calculation of wind tunnel corrections, the overall method is quite extravagent in terms of computational effort. One of the purposes of the present work is to assess the accuracy of the method of boundary fitted coordinates. Application to the real problem of determining the high blockage tunnel corrections provides a suitable and practical test case. Obviously, as with most extensive computational efforts, the immediate application of the algorithm by other users cannot be expected (a manifestation of the "not invented here" syndrome). The computational program is quite large and expensive to run. Extensive use of the present procedures would result in a series of charts, tables, or correction relations which would be of more immediate practical use at other test installations. This data base would be quite extensive, because of the number of parameters involved. The generation of this extended data base was not a feasible undertaking due to time and fiscal constraints.

IV. Experiments

To investigate the applicability of the proposed wall interference corrections calculated using the methods of Chapter III, experiments were carried out in the University of Alberta low speed wind tunnel on several models using different tunnel geometries. All tests were performed at a chord Reynolds number of 10^6 . Two single element airfoils and one two element airfoil were tested. The tunnel height could be adjusted by the movement of two parallel interior wall inserts, one on each side of the two dimensional models. Pressure data was acquired using several high sensitivity differential pressure transducers and a computer controlled data acquisition system. Pressure distributions were integrated using the trapezoidal rule to give the uncorrected force and moment coefficients.

Free field experimental data for all three models was obtained using the standard low blockage corrections described in Chapter II on data obtained with the inserts removed, giving a chord-to-height ratio of 0.41. For these tests, the section drag coefficient was obtained using a wake rake.

The interference tests involved several wall positions yielding a broad range of chord-to-height ratios. The tunnel wall pressure distribution was measured for comparison with the inviscid theory. Due to physical constraints, no

provision was made for drag measurements during the blockage tests.

Data for each tunnel configuration was obtained for a range of angles of attack where attached flow on the sections was maintained since the present potential flow theory is based on the assumption that viscous effects are neglected. The final data for the interference tests was then reduced using both the present corrections and the standard constant incidence corrections for comparison with the free field tests.

A. Test Equipment, Procedure, and Data Reduction

Tunnel Calibration

The University of Alberta Department of Mechanical Engineering operates a closed circuit, single return, low speed wind tunnel with a test section 1.2m high, 2.4m wide and 11.0m in length. The tunnel can be operated as a low speed boundary layer tunnel or high speed aerodynamic tunnel, with precise speed control. For aerodynamic testing, the maximum unit Reynolds number is $2.0*10^6$ per meter, depending on the tunnel temperature, atmospheric pressure, and the presence of filters upstream of the settling chamber. A turbulence level in the test section of less than 0.1% is obtained using three fine mesh screens at the entrance to the 6.2:1 contraction. Two dimensional models, usually of one meter chord, are mounted vertically in the test section, having therefore a span of 1.2 meters.

The tunnel airspeed was determined using the procedure described in Pope and Harper [5]. The change in static pressure between the settling chamber and a location approximately three-quarters of the length through the contraction was measured. This was calibrated against the test section dynamic pressure at the model location in the empty tunnel obtained using a standard pitot-static probe, corrected for stem and tip error. This procedure was adopted when preliminary tests indicated that the static pressure field generated by the large models extended quite far upstream, making local measurement of the tunnel free stream static pressure unreliable. The final airspeed calibration was insensitive to model orientation.

For the blockage tests, the test section dynamic pressure was determined by a pitot-static probe mounted between the wall inserts, approximately two chord lengths upstream from the model leading edge. Tunnel speed was set for a low angle of attack for which the upstream influence of the model is small, after which the probe was removed from the flow. The precise speed control of the tunnel drive was thereafter able to maintain the tunnel speed within 1%, as monitored by the differential pressure through the contraction, provided that flow separation on the model was avoided, which would increase the total tunnel loss coefficient and retard the flow. This procedure was necessary since the models used were extremely sensitive to wake turbulence produced by the probe. Subsequently, the

test section free stream static pressure was determined from measurements near the leading edge of the wall inserts, where the indicated pressure was observed to be the same on both walls.

Models

To ensure the coverage of a wide range of test geometries, three airfoil sections were tested. Section profiles for the three models are shown in Figure 36.

The first model was a single element high performance section which had been designed for very low drag (Cd=.007) at the test Reynolds number. This minimized the wake blockage and boundary layer displacement effects, allowing closer matching of the real flow with the theoretical flow, so long as separation was avoided.

The second model, also a single element section, was chosen for its very thick cross-section and high camber. This section, designed by Kennedy [13], develops the highest lift coefficient for a single element section known to the present author. Unfortunately, as opposed to the first model, the viscous effects are very large and the boundary layer and wake effects are not negligible. At a Reynolds number of 10^6 , Kennedy found that the combined displacement thicknesses of the upper and lower surface boundary layers at the trailing edge was 23mm for the design angle of 15

degrees. The drag coefficient was correspondingly high, Cd=0.0284, and the maximum lift obtained was significantly less than the potential flow value. Nevertheless, the lift/drag ratio was still quite high, and the lift interference and solid blockage corrections predominated.

The third section tested was a two element section based on model #1 with a 35% chord slotted flap, deflected 20 degrees. This section develops quite high lift/drag ratios, and again allows the real flow to correspond closely to the inviscid theory.

The boundary layer structure on each of these three models was relatively insensitive to changes in the pressure distributions caused by incidence changes when operated within the laminar drag bucket. Pope and Harper [5] suggest that changes in boundary layer structure caused by distortion of the pressure distribution becomes important only for very high c/h ratios. It was expected, then, that distortion of the pressure distributions during the blockage tests would not produce large changes in the section performance. This was subsequently confirmed for moderate blockage values. For the tests at the highest blockage values, the effect of the wall-induced pressure distribution distortion became quite pronounced. Each of the single element sections utilizes a Stratford-type turbulent boundary layer pressure recovery, which allows maximum pressure recovery with minimum drag. The Stratford boundary layer develops with a constant shape factor just on the

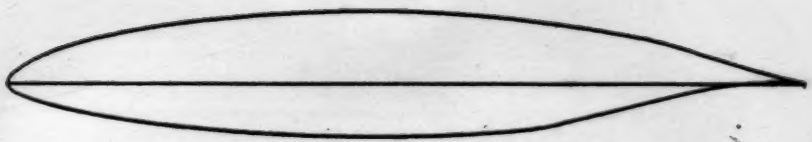

a) Model #1

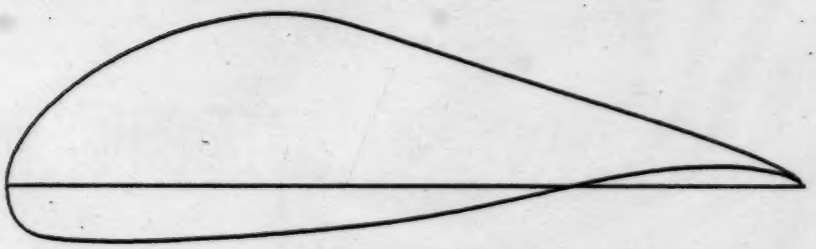

b) Model #2

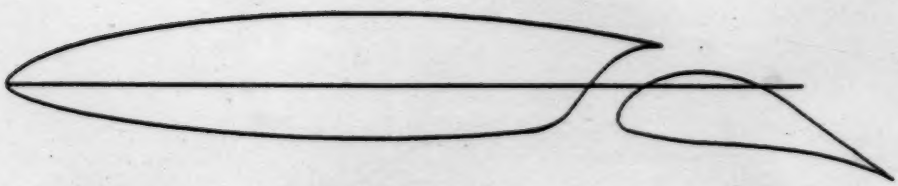

c) Model #3

Figure 36 Profiles of Models Tested

point of separation. At high blockage, the distortion of the pressure distribution disrupted this recovery, resulting in changes in the section performance. Particularly, for model #2, the maximum lift was affected, as well as performance of the section leading up to stall.

All models were fitted with 0.5mm diameter static pressure taps around the section on the model centre-line, concentrated in regions of high pressure gradients. Static pressure tubes were led out of the tunnel through the model interior and connected to a multi-tube scanivalve which sequentially connected each tube to a sensitive pressure transducer.

The models were mounted on 3/16" thick aluminum endplates, equipped with boundary layer suction holes adjacent to the model surface in regions of adverse pressure gradients. The model and endplates were then mounted on circular turntables in the tunnel ceiling and floor which could be rotated to give the desired angle of attack. Each turntable was fitted with externally mounted suction plenum chambers, which were connected to a large centrifugal fan through 6" diameter rigid plastic pipe. The plenum pressure was maintained at 2.8kPa below atmospheric pressure (Cp=-10). The purpose of the boundary layer suction was to remove portions of the thick boundary layer on the wind tunnel floor and ceiling. In the presence of adverse pressure gradients generated by the model, separation of these boundary layers would seriously degrade the two

dimensional character of the flow by allowing formation of strong trailing vortices.

Wall Inserts

The wall inserts were made up of 3/4" plywood sheets. Initial tests were carried out on the low drag section (#1) with the inserts extending 2.44 chord lengths fore and aft of the model mid-chord. This was subsequently increased to 3.05 chord lengths, for a total extent of the inserts of 6.10 meters. The inserts extended forward to the tunnel contraction exit plane. Each insert panel was fitted with 24 1/8" diameter static pressure taps at a spacing of 6" near the model and 12" at the extremities. The total extent of the wall pressure tap coverage was 4.42 chord lengths. Each tap was carefully flush mounted and counter-sunk to ensure accurate static pressure measurements. The inserts were attached to the floor and ceiling of the tunnel, and were kept parallel within +/- 3mm over the entire length. At the low dynamic pressure of the tests, deflection of the inserts was negligible. The leading edge of the inserts was rounded to ensure smooth entry of the flow into the reduced test section. During preliminary runs, vertical wires with numerous 6" tufts were placed upstream of each leading edge to observe any unwanted flow curvature. No serious flow irregularities were observed and the wires were later

removed.

The test geometry for the free field tests is shown in Figure 37. The wake rake apparatus is shown downstream of the model. Figure 38 shows the same model with the wall inserts in place at a chord to height ratio of 0.93, the maximum possible due to overlapping of the inserts with the model turntables.

Pressure Measurements - Transducers and Calibrations

Differential pressures were measured using several Validyne pressure transducers, all supplied with the tunnel stagnation pressure as reference. The transducers were equipped with appropriate diaphragms (1" water, 0.1 psi or 0.2 psi) and calibrated against an accurate inclined manometer. All calibrations were linear, and were re-checked approximately every 10 hours of running time. The maximum drift observed in the sensitivity of the transducers was less than 0.5%. The data acquisition system automatically checked and adjusted the calibration zeros at the start of the data acquisition sequence, when all transducers were supplied with zero pressure differential. To diminish the effect of random pressure fluctuations, each measurement was repeated three to five times and averaged. In addition, when using the wake rake for drag measurements, the wake pressure transducer output signal was sent through a low pass filter (cut off 0.3 hz.), to smooth out fluctuations due to wake turbulence. During the data sequence, the scanivalve

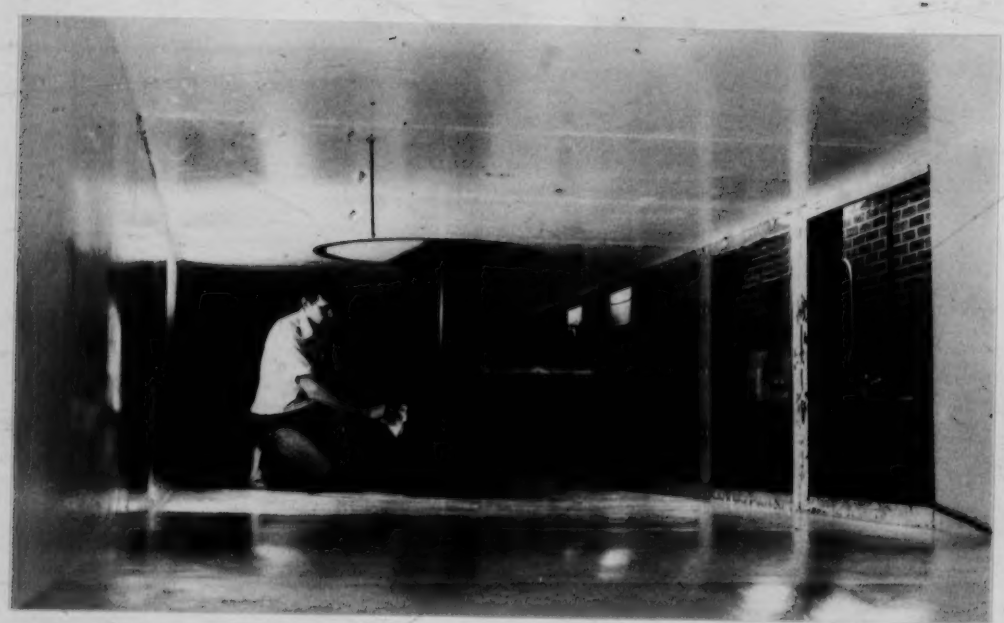

Figure 37 Tunnel Geometry for Free Field Tests

Figure 38 Tunnel Geometry for Blockage Tests

pressure transducers were allowed to stabilize for 1/2 second before readings were taken.

Data Acquisition and Reduction

The large extent of these experimental investigations would not have been possible without automated data acquisition and reduction. The system configuration is shown in Figure 39. During the acquisition phase, under control of the central computer (Hewlett-Packard HP-85), the scanner would route the desired pressure transducer signal to the digital voltmeter. Voltage readings were returned to the computer and converted to pressures using the appropriate calibration. The scanivalves would then be stepped to the next location and measurements repeated until all pressure taps had been monitored. The resulting pressure distributions were then integrated using the trapezoidal rule to obtain the model force and moment coefficients. Finally, the pressure distributions could be plotted, either in soft copy on the computer screen, or in hard copy on the plotter. All pressure data was stored on magnetic tape cartridges for later retrieval and further analysis on the University main computer, if desired. The entire data acquisition/reduction sequence for a single angle of attack could be accomplished in under three minutes with all options in effect. For the free field tests, the standard corrections were incorporated in the system program. At the conclusion of a run, a lift curve (and drag polar for free

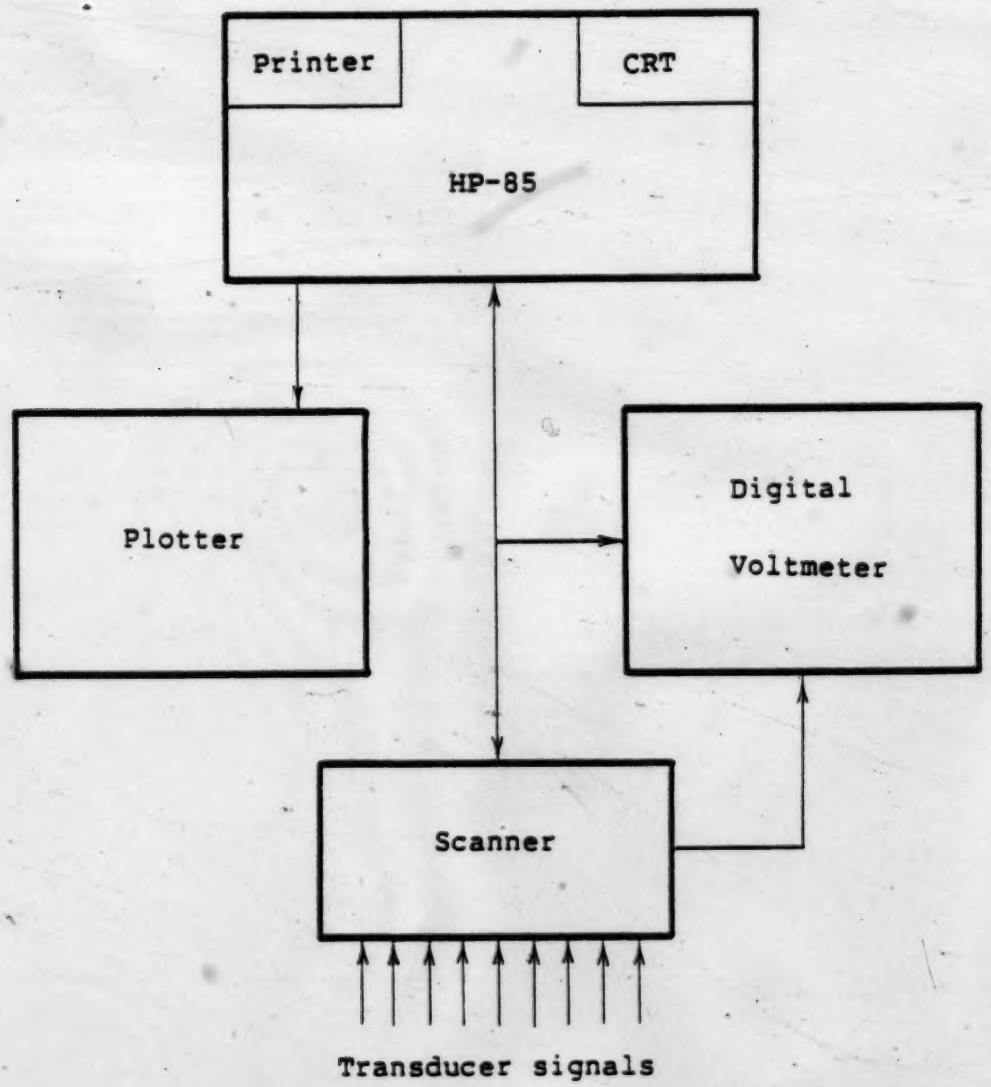

Figure 39 Data Acquisition Schematic

field tests) was automatically produced.

Free Field Drag Calculation

One of the most difficult quantities to measure is the section profile drag. The procedure adopted here is based on the Jones formula (Schlicting [29]) for the determination of the profile drag when the static pressure at the wake measurement location is unequal to the free stream static pressure. It was assumed that the stagnation pressure outside the wake was the same as the stagnation pressure ahead of the model, and that the static pressure was constant through the wake. The resulting formula is

$$C_d = 2 \int \sqrt{\frac{q_2 - \Delta p}{q_1}} \left(1 - \sqrt{1 - \frac{\Delta p}{q_1}}\right) dy \qquad (44)$$

where q_1 is the main tunnel dynamic pressure, calculated from the tunnel contraction, q_2 is the dynamic pressure outside the wake, and Δp is the drop in stagnation pressure within the wake as measured by the transducer. The integral was evaluated using the trapezoidal rule across the width of the wake.

B. Free Field Results

The raw and corrected experimental results for the three models are shown in Figures 40 to 42 for the lowest c/h ratio of the tests (c/h=0.41). Both the first and second

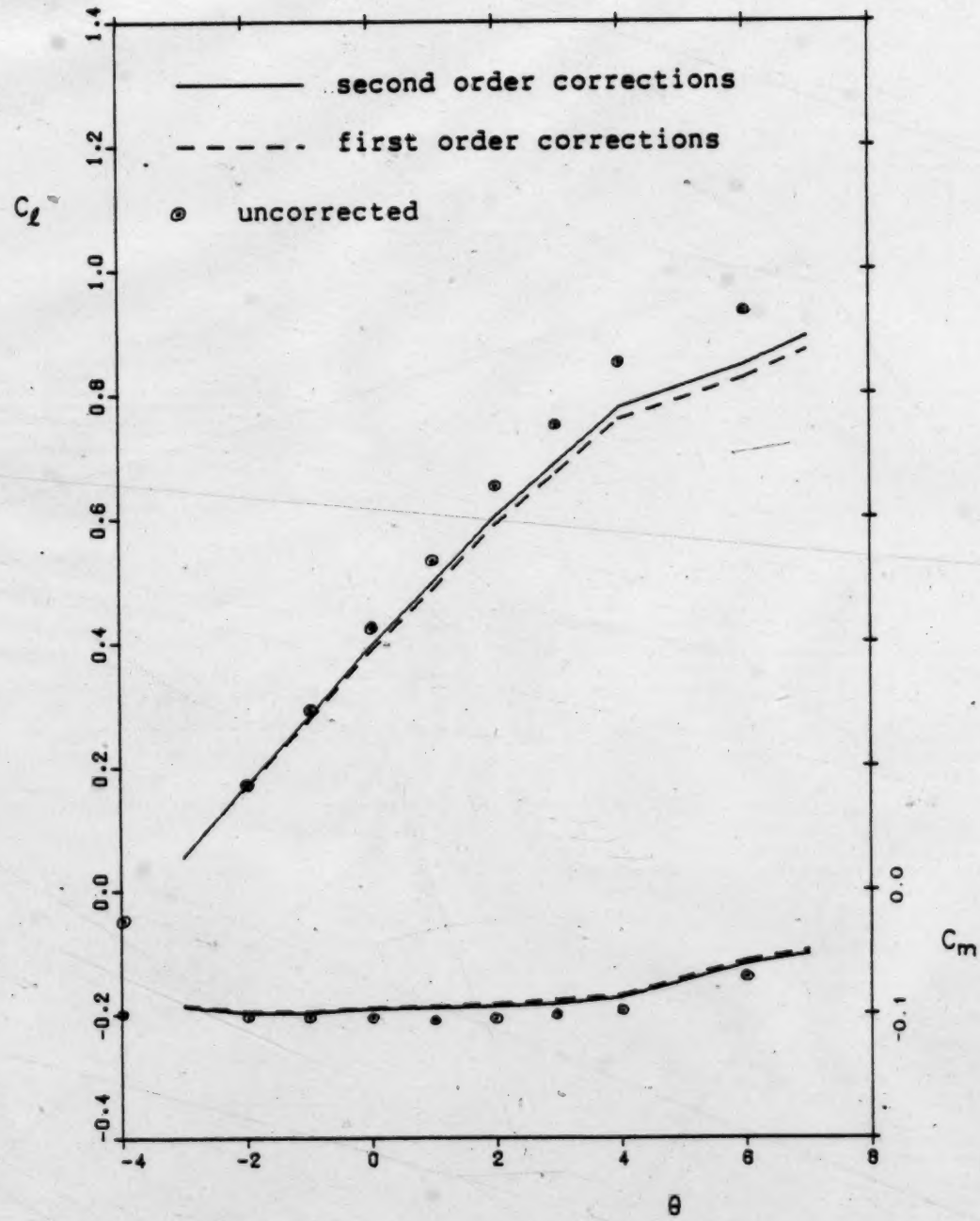

Figure 40 Model #1 - Free Field Lift and Moment Coefficients

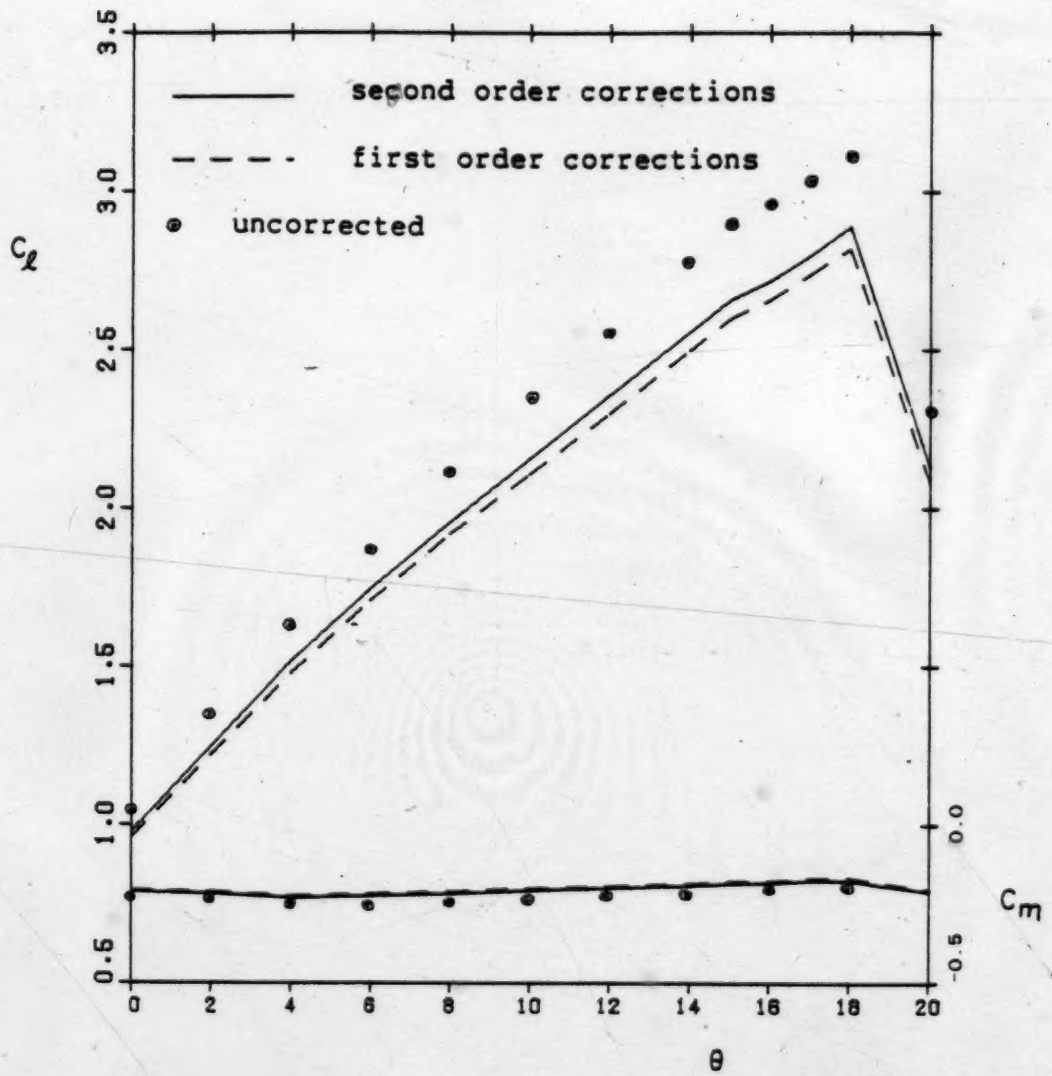

Figure 41 Model #2 - Free Field Lift and Moment Coefficients

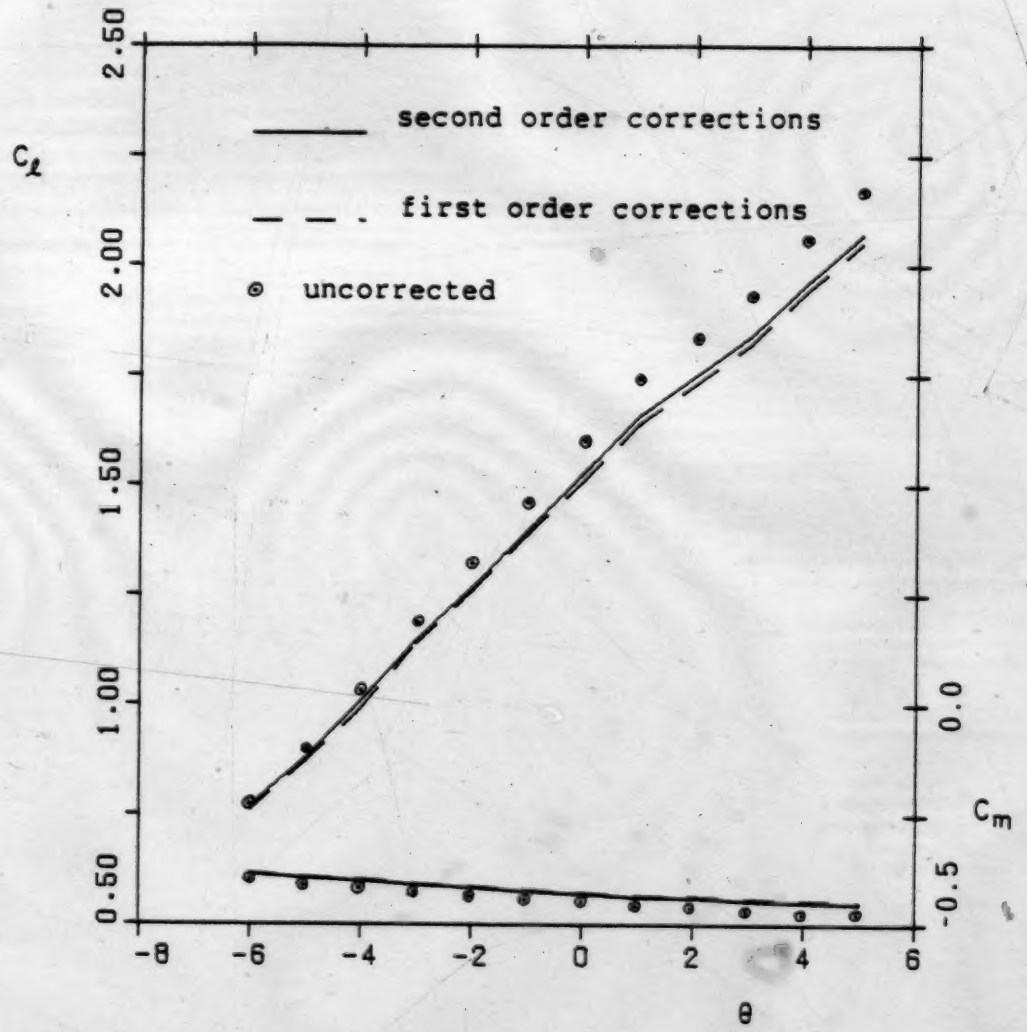

Figure 42 Model #3 - Free Field Lift and Moment Coefficients

order corrections were made, using the constant incidence forms, equations (20) and (21). The lift curve slope used in the constant incidence corrections was evaluated using the corrected data in each case using the iterative procedure described previously. Both corrections yield similar results, with the first order lift corrections being slightly larger than the second order forms. The two forms for the moment corrections yield practically identical results. For this c/h ratio, the first order corrections are probably inappropriate and it was assumed, therefore, that the results obtained using the second order forms represent true free field values.

Figures 43 to 45 show the contributions of wake blockage, solid blockage, and lift interference to the total lift correction for each model for these free field results. The wake blockage correction is a minor portion of the total (typically less than 10%) and for the wall interference tests was therefore ignored.

C. High Blockage Results

The effect of the wall position on the uncorrected data is shown in Figures 46 to 48 for the three models. The free field results are also included in these figures and it is observed that at high blockage and lift coefficient, the lift correction approaches 30% of the experimental value.

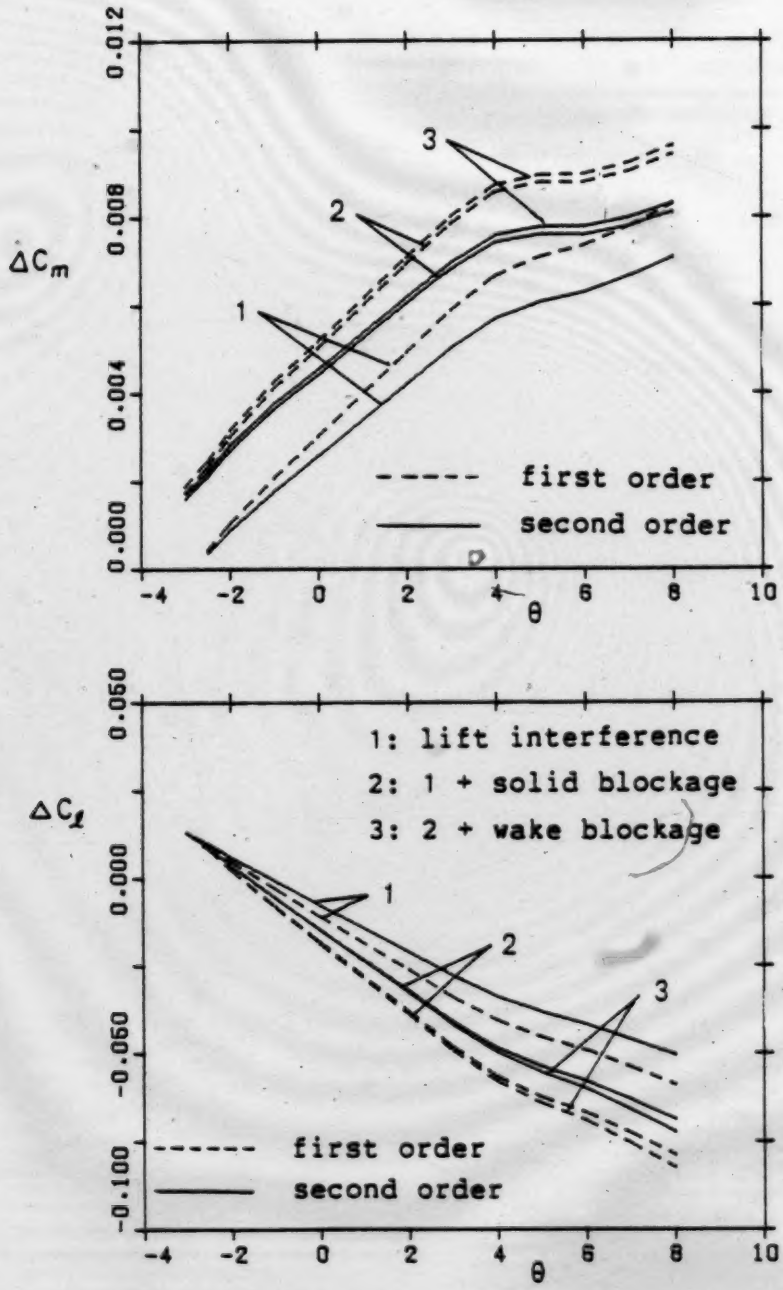

Figure 43 Contributions of Corrections - Model #1, Free Field

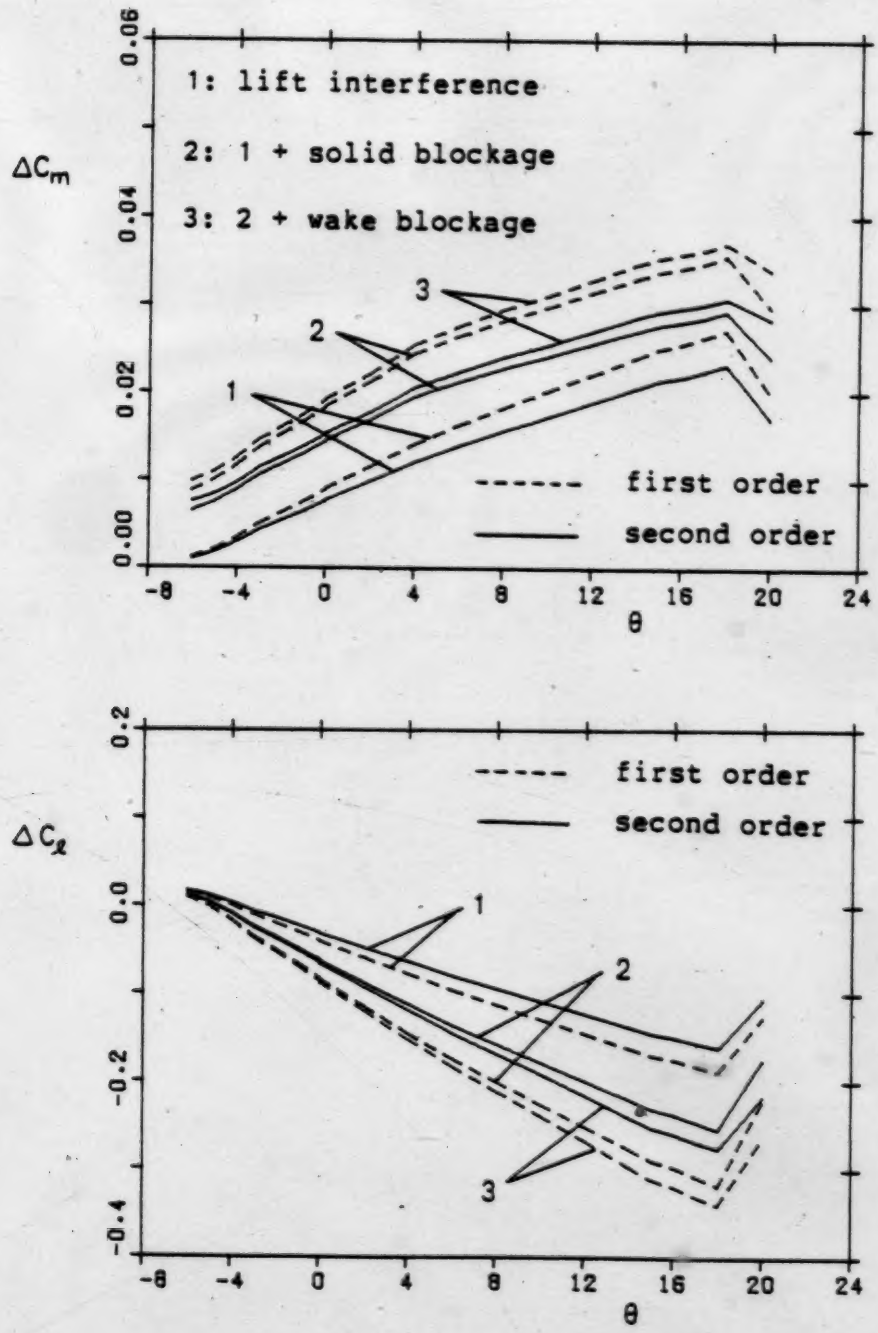

Figure 44 Contributions of Corrections - Model #2, Free Field

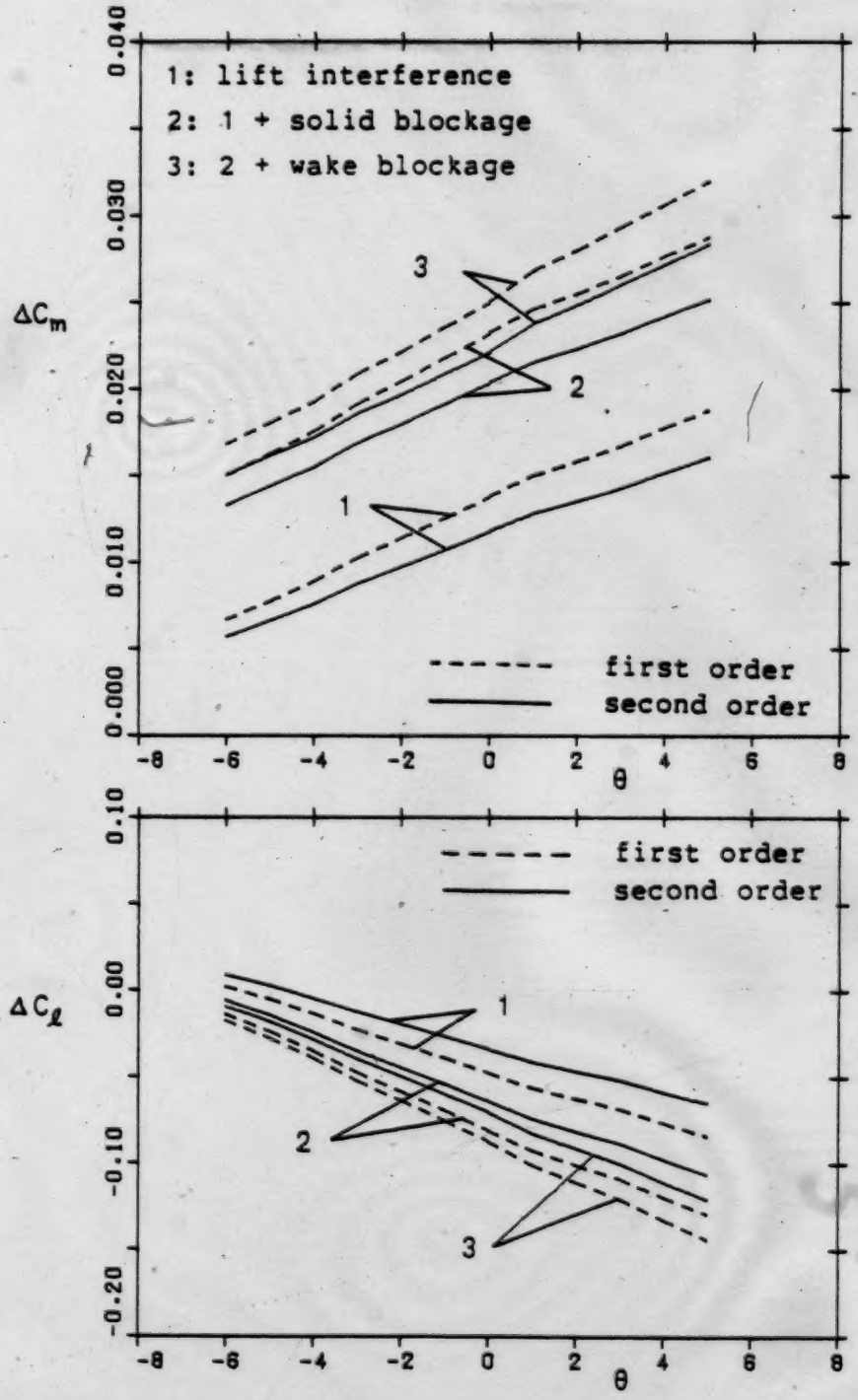

Figure 45 Contributions of Corrections - Model #3, Free Field

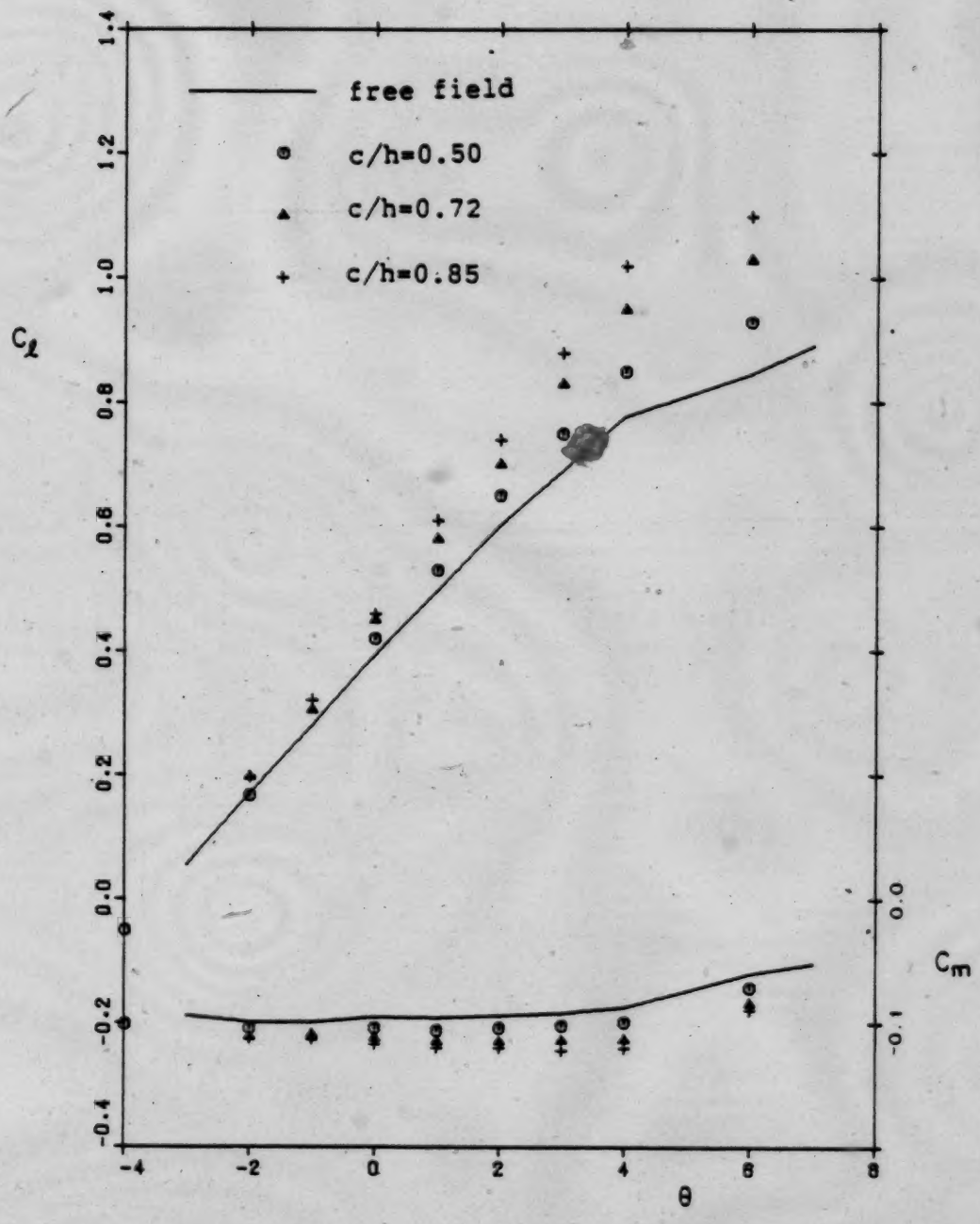

Figure 46 Model #1 - Effect of Wall Position on Uncorrected Data

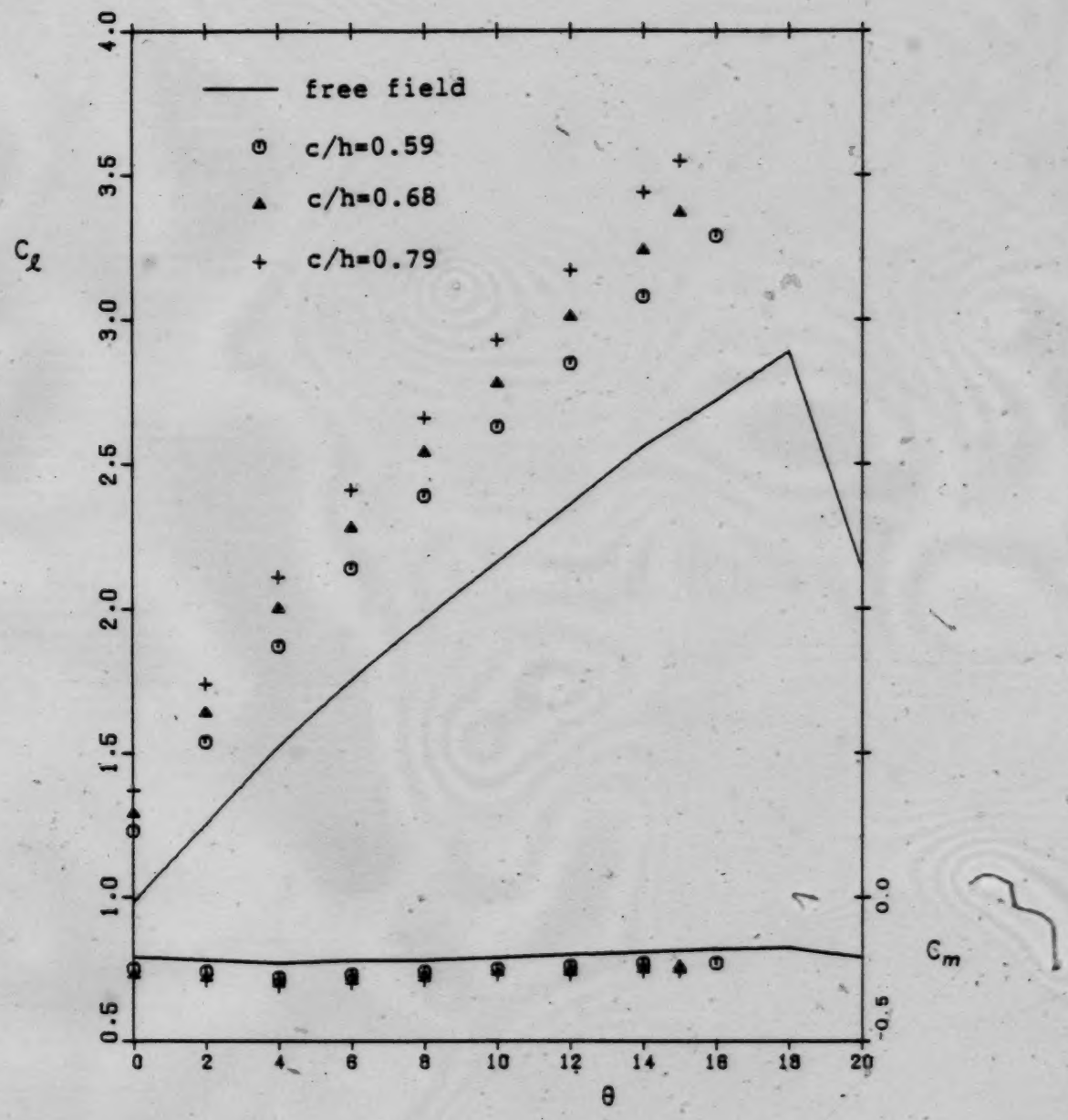

Figure 47 Model #2 - Effect of Wall Position on Uncorrected Data

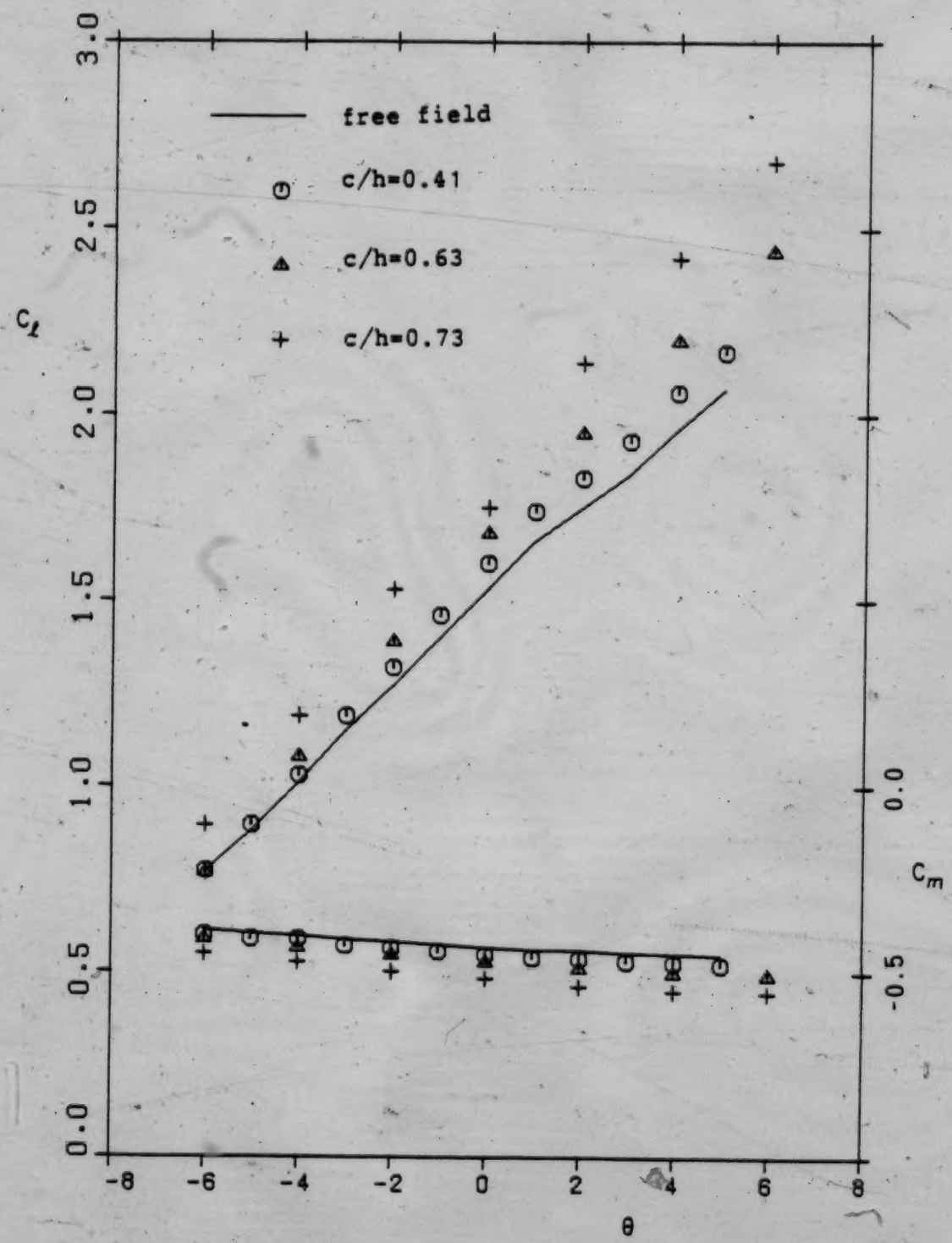

Figure 48 Model #3 - Effect of Wall Position on Uncorrected Data

This high blockage data was corrected using the standard forms, but ignoring the wake blockage, to yield the results shown in Figures 49 to 51. The first order corrections are consistently too large, while the second order corrections are too small, and the errors in these corrections increase with tunnel blockage and lift. The standard forms, both first and second order, are clearly unsatisfactory for c/h ratios greater than 0.5.

The present corrections were implemented as follows. The theoretical analysis was used to generate correction tables for each model which contained values of the lift and moment increments as functions of the uncorrected lift coefficient and c/h ratio. The correction tables for the three models are displayed graphically in Figures 52 to 54. For a given test, the relevant correction was obtained by entering the table at the experimentally obtained lift coefficient and c/h ratio and extracting the relevant correction. This procedure was automated using a two-way cubic spline interpolation, shown schematically in Figure 55. The correction table data was used to construct the splines S1 to S5 for five c/h ratios between 0.2 and 1.0, which bracketed the experimental tests. The increment at the uncorrected lift coefficient was then determined by interpolation on S1 to S5. A cross-spline was then fitted, S6, to these increments and the final correction was extracted by interpolation on S6 at the experimental c/h ratio. This somewhat involved procedure allowed a great

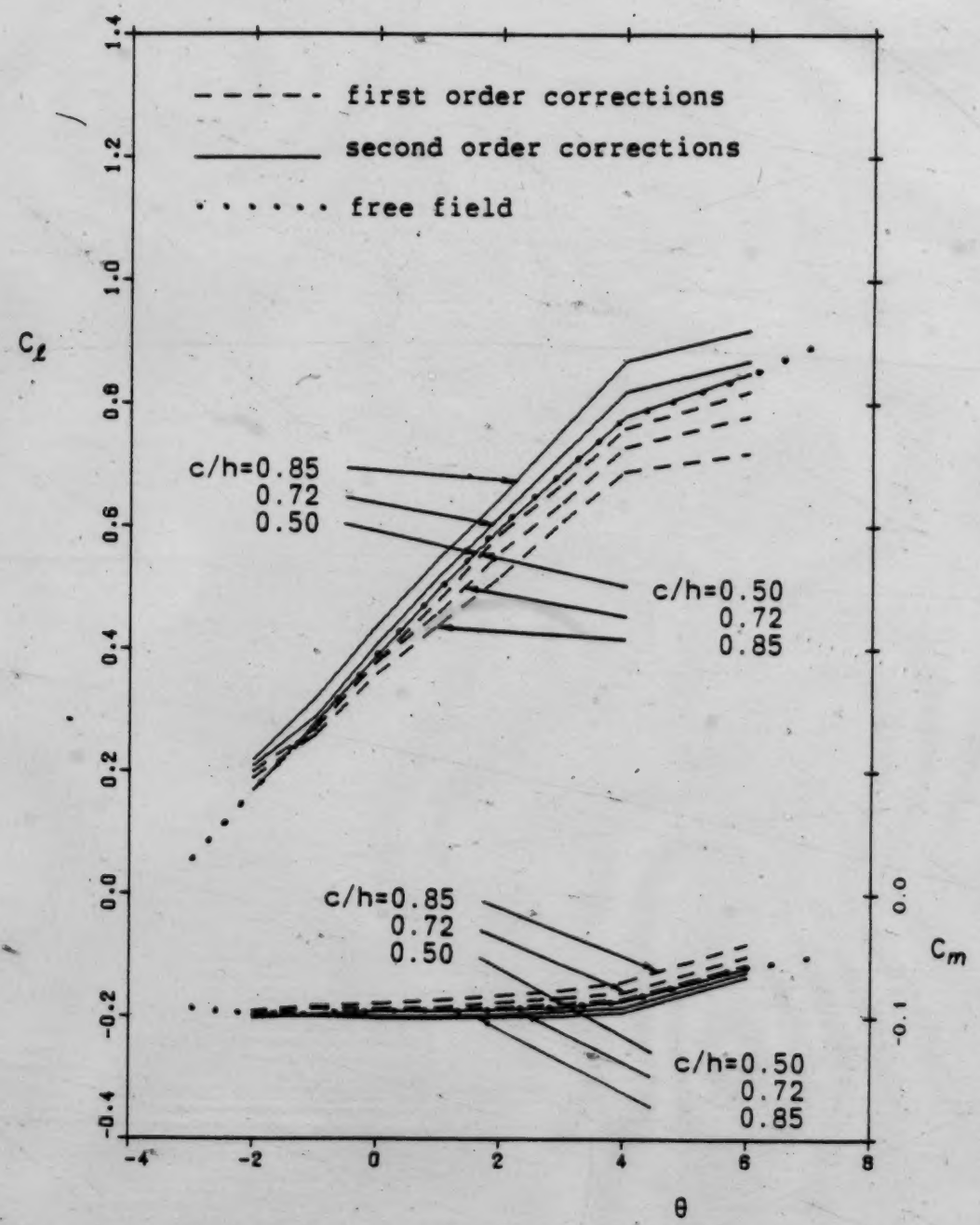

Figure 49 Model #1 - High Blockage Results (Standard Corrections)

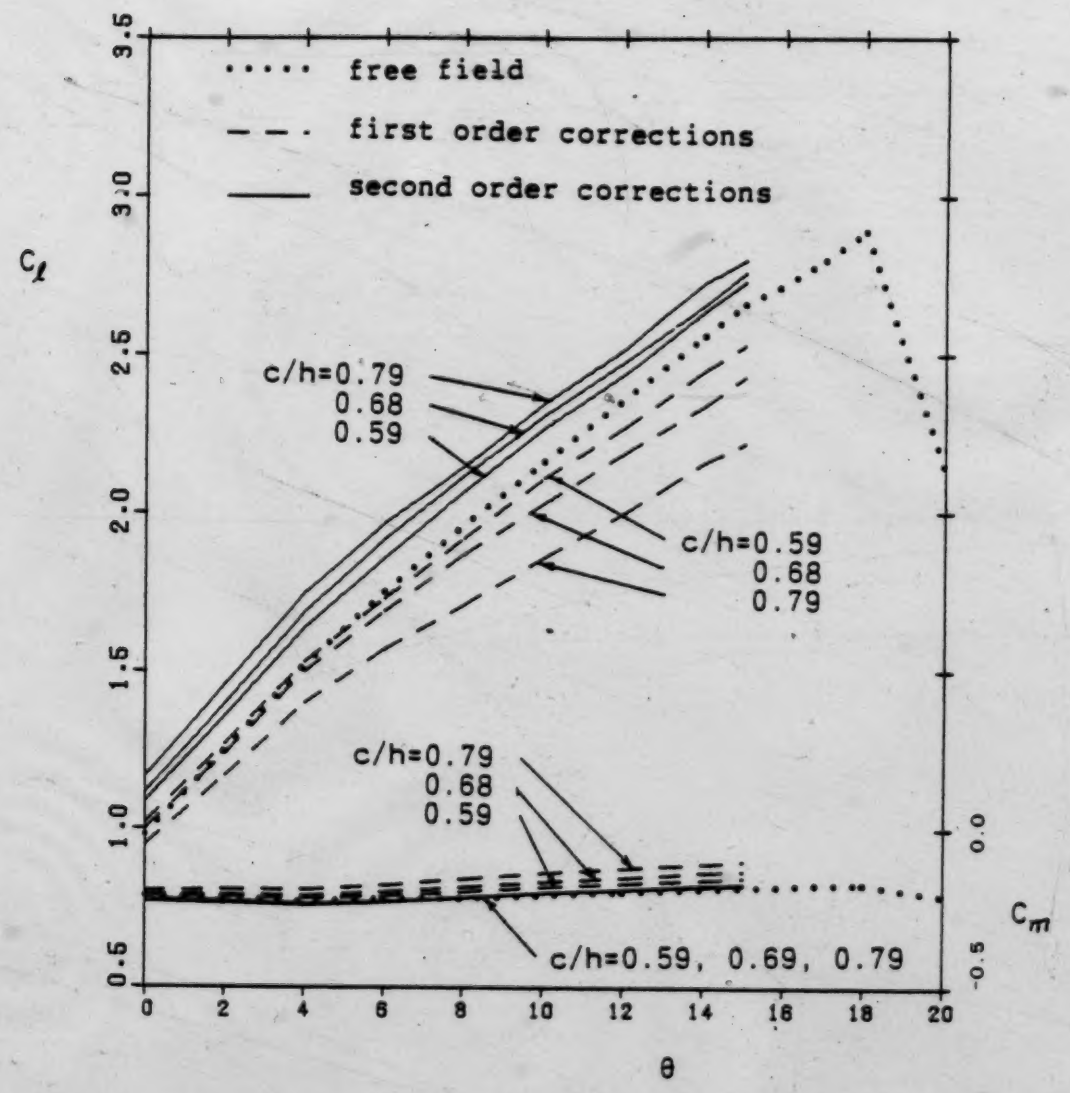

Figure 50 Model #2 - High Blockage Results (Standard Corrections)

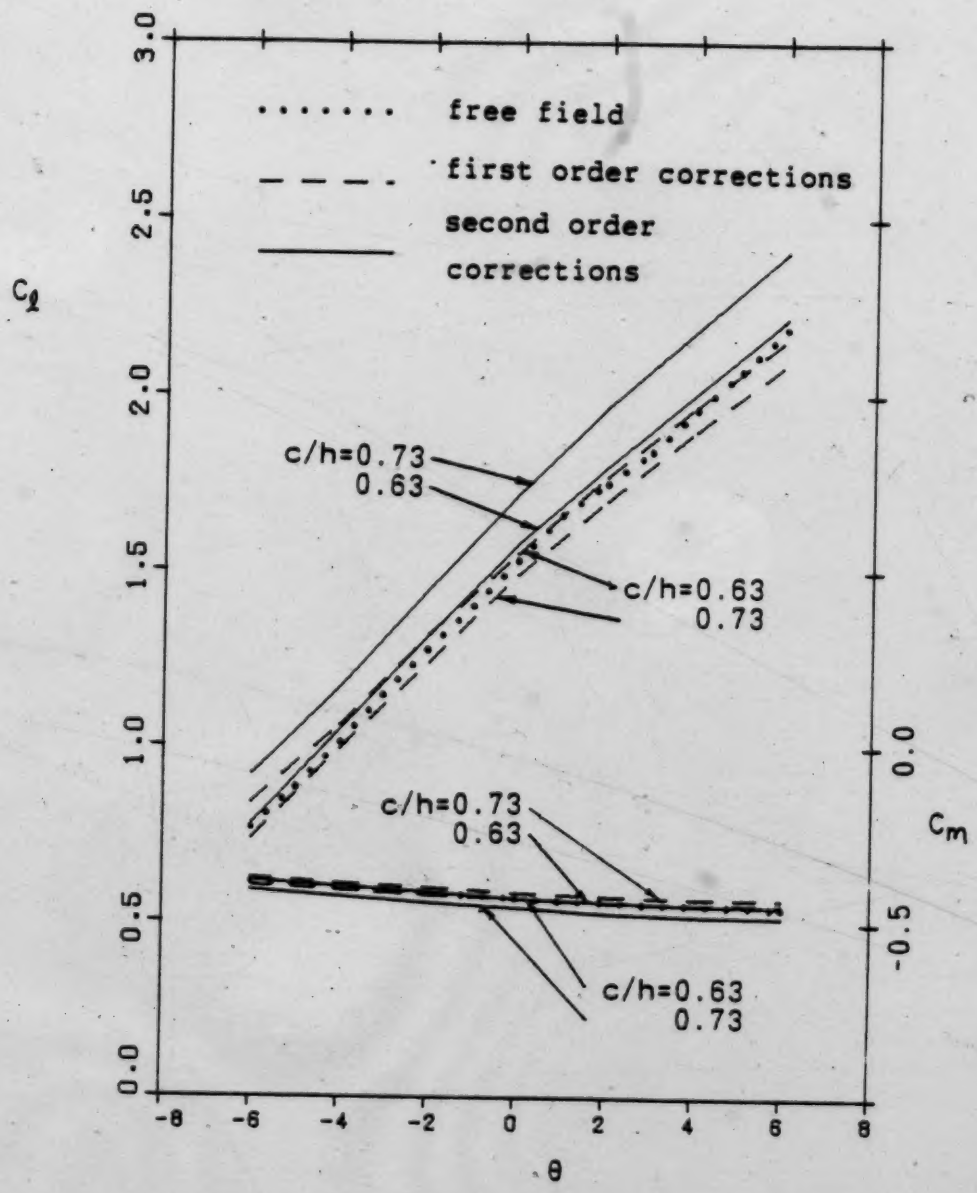

Figure 51 Model #3 - High Blockage Results (Standard Corrections)

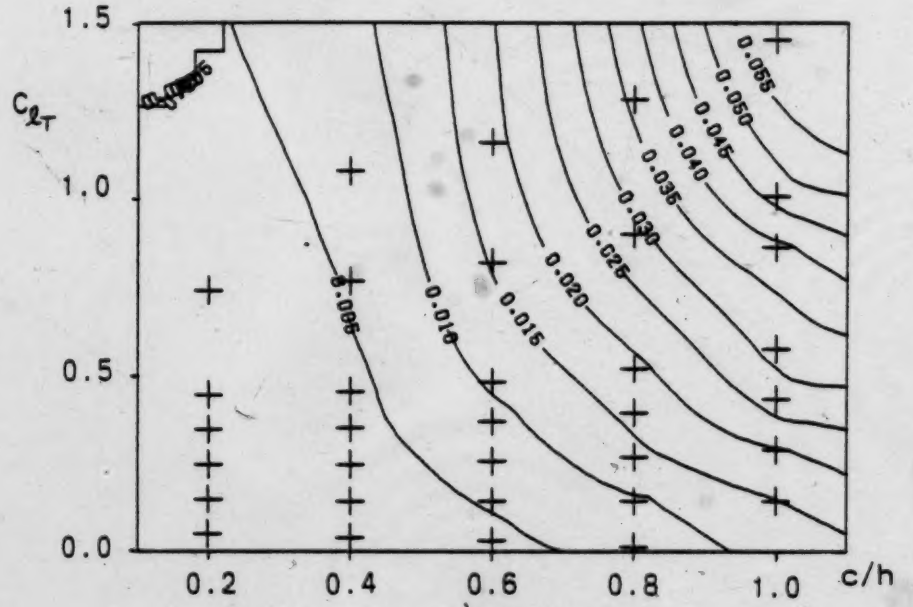

a) moment increment, ΔC_m

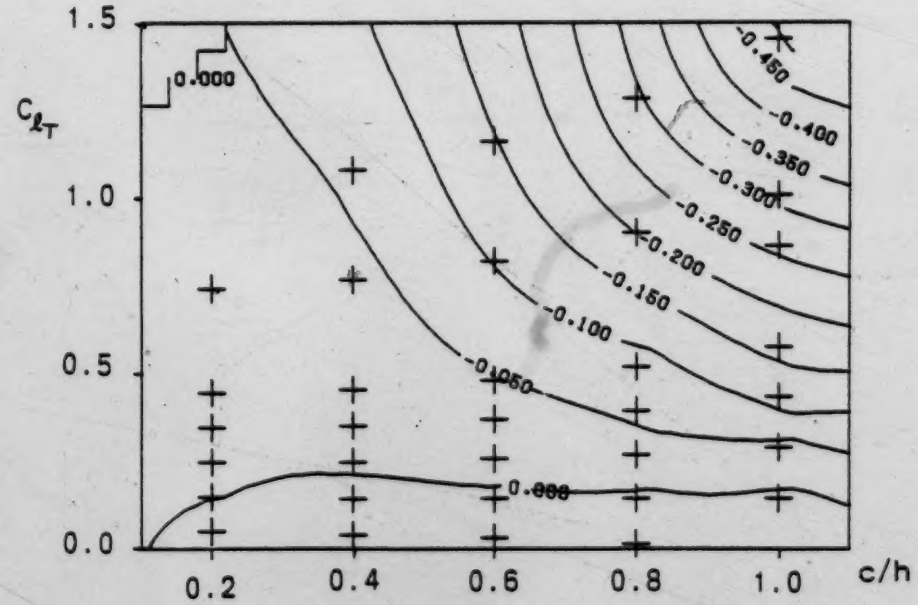

b) lift increment, ΔC_ℓ

Figure 52 Model #1 - Correction Table

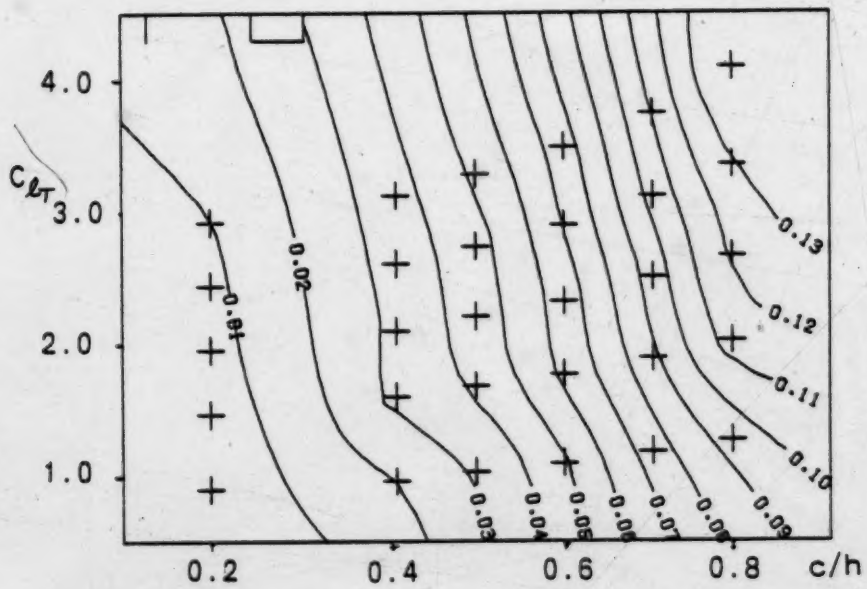

a) moment increment, ΔC_m

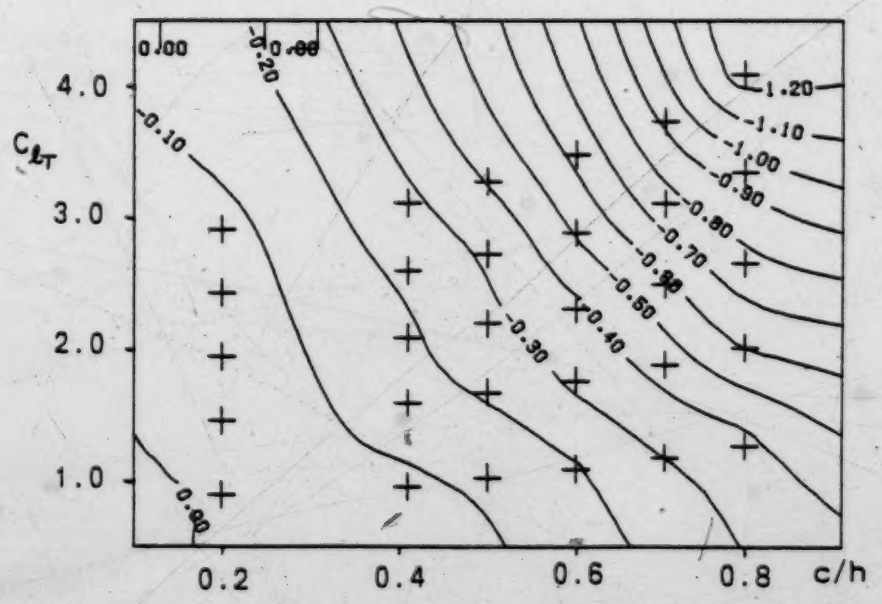

b) lift increment, ΔC_ℓ

Figure 53 Model #2 - Correction Table

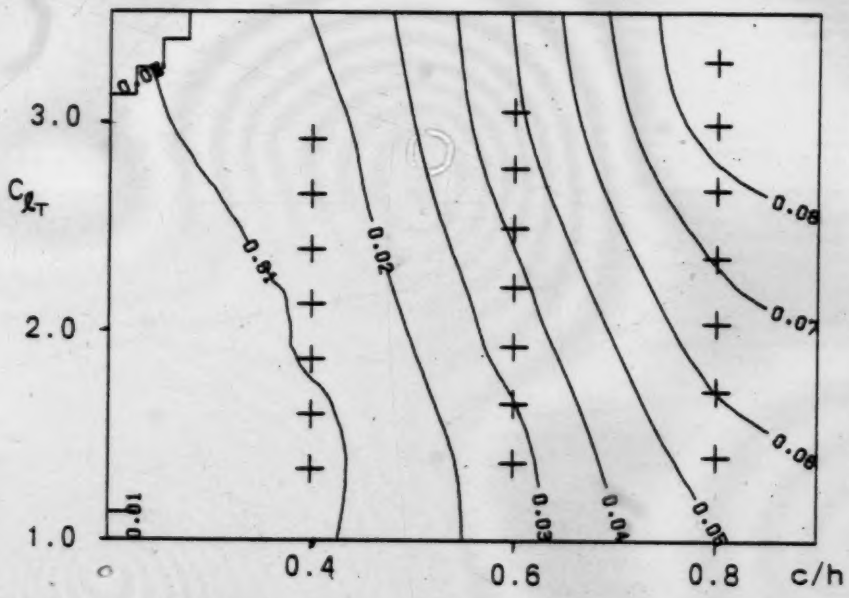

a) moment increment, ΔC_m

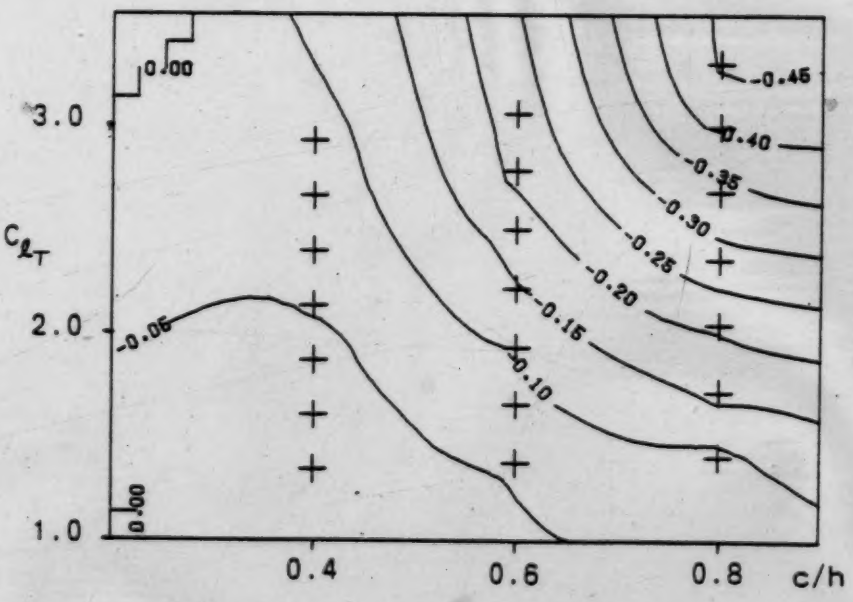

b) lift increment, ΔC_ℓ

Figure 54 Model #3 - Correction Table

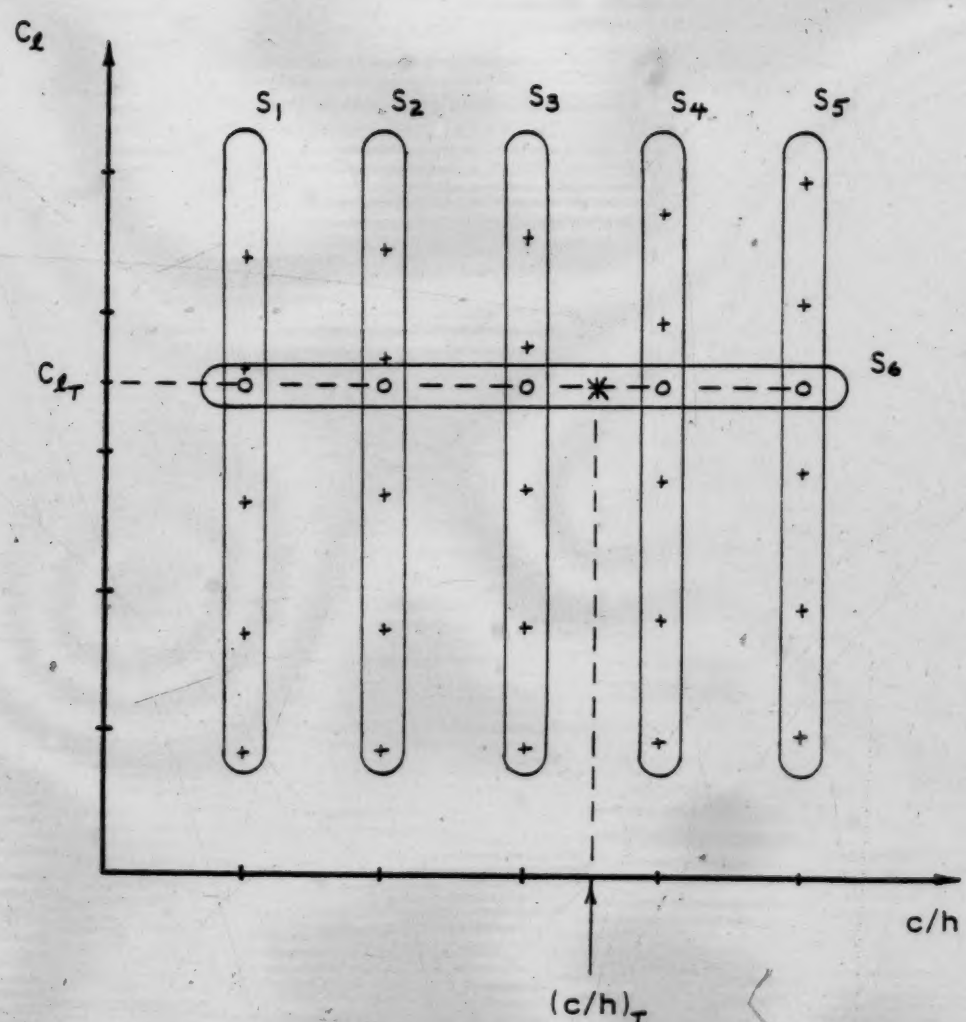

\+ theoretical correction evaluated

o first interpolation at measured lift

* second interpolation at test c/h

Figure 55 Spline Interpolation Scheme for Correction Tables

reduction in the number of complete theoretical calculations used to generate the table: the data base consisted of calculations at five different angles of attack, for each of the five c/h ratios. The splines S1 to S5 were evaluated only once for each model.

The data corrected using the above procedure is shown in Figures 56 to 58 for the three models, along with the free field results obained using the second order corrections for the lowest c/h ratio. There is good agreement of the corrected data with the free field data. Results for model #1, a more typical airfoil shape, are excellent. The results for model #2 are satisfactory for all but the highest c/h ratio, where the effect of the pressure distribution distortion is evident. The two-element section lift results are satisfactory; however the moment corrections are not an improvement over the standard forms. This was thought to be due to errors in the theoretical pressure distribution in the slot region on the main section, caused by the grid geometry. Although not largely affecting the lift, this had a large effect in the theoretical pitching moment.

For a normal test, at a single c/h ratio, the above procedure using the complete correction table is not required. In this case, theoretical lift and moment increments may be calculated for several angles of attack for the experimental c/h ratio. A single spline may then be fitted through this data, and the correction interpolated at

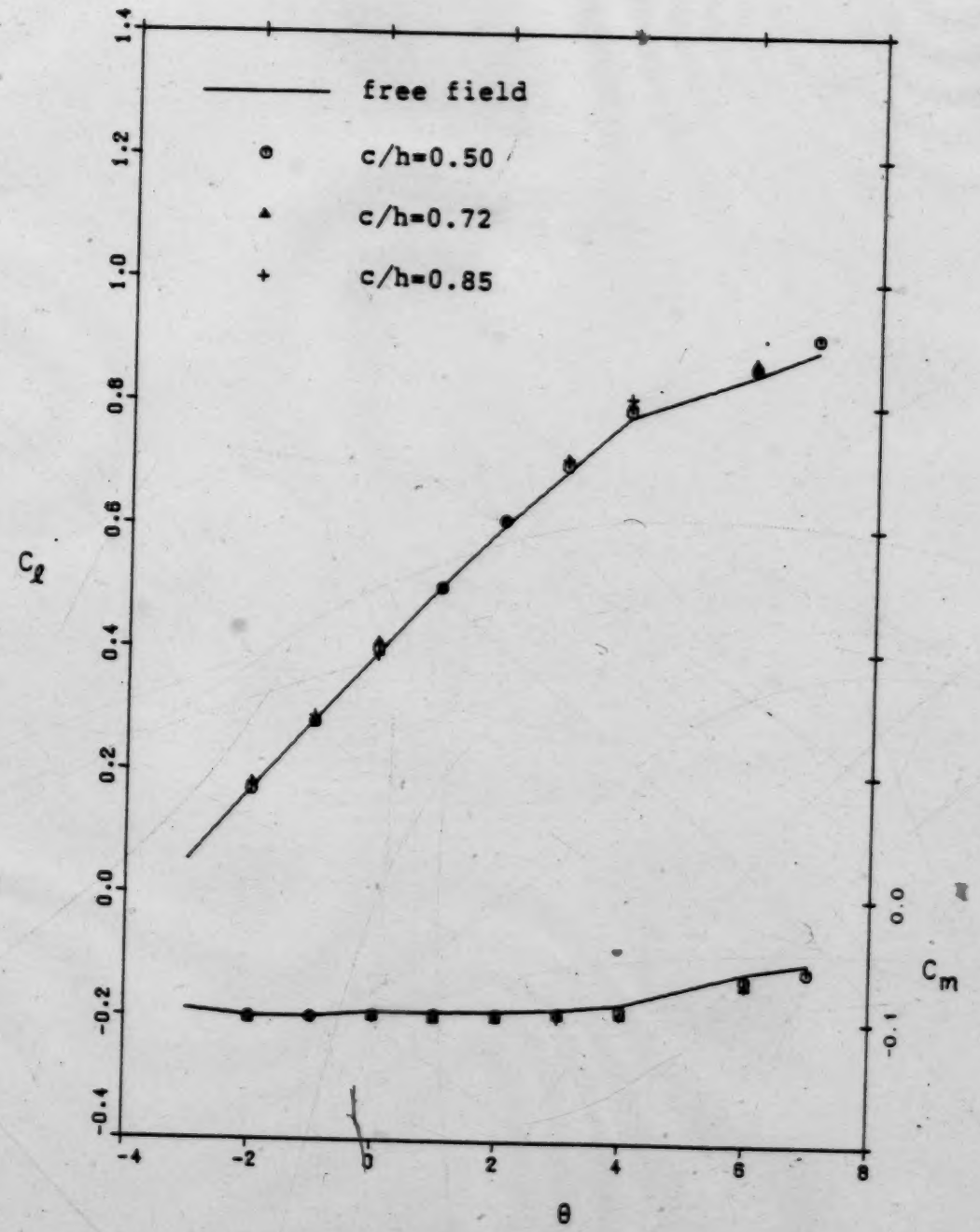

Figure 56 Model #1 - High Blockage Results Using Correction Table

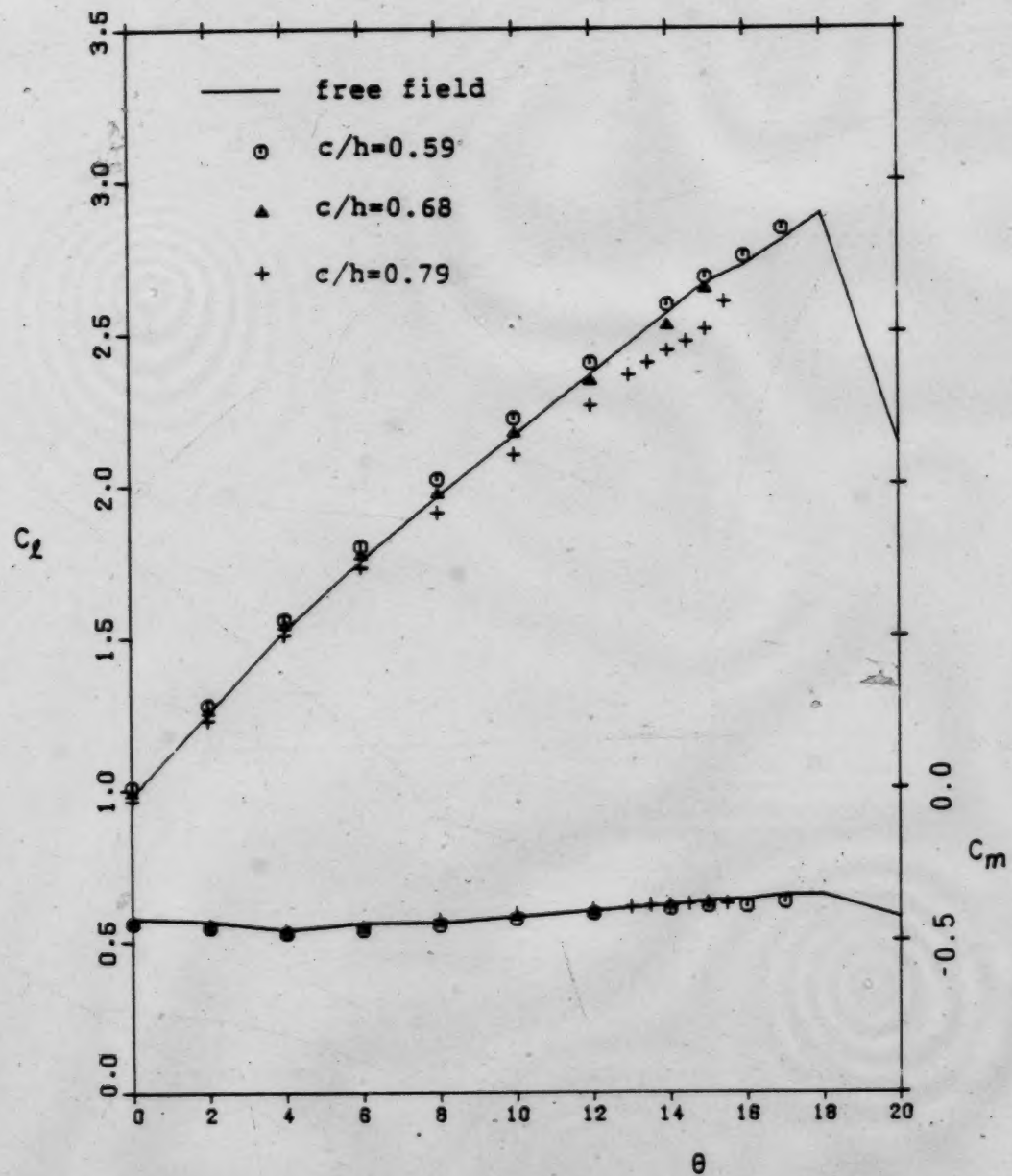

Figure 57 Model #2 - High Blockage Results Using Correction Table

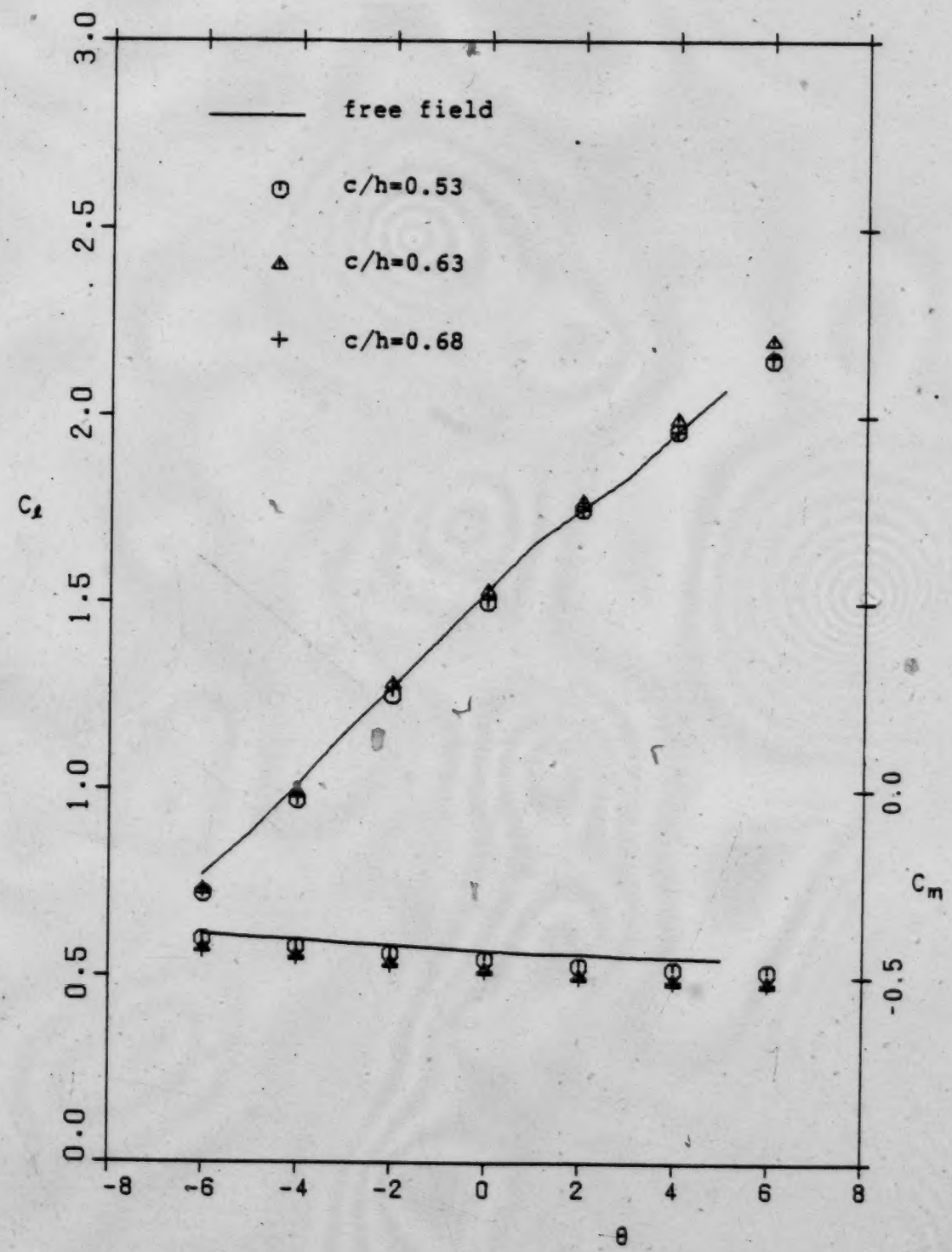

Figure 58 Model #3 - High Blockage Results Using Correction Table

the experimental lift coefficient.

D. Conclusion

The numerically generated corrections are a satisfactory improvement over the standard forms for the three models tested. This indicates the possibility of utilizing a wider range of tunnel geometries, in particular higher c/h ratios, for two-dimensional testing. The effect of pressure distribution distortion which occurs at very high blockage places an upper limit on the allowable range of c/h ratios for which reliable corrections can be made. This upper limit is near c/h=0.7, nearly twice the range for which the standard corrections are considered valid. The numerical corrections apply equally well for the two-element section, although great care in obtaining the theoretical solution is necessary. These results indicate that the present correction technique is valid, and can be used for a wide variety of wing profiles and wind tunnel geometries.

V. Conclusion

Aerodynamic performance data obtained in wind tunnels is subject to the influence of the tunnel boundaries. To obtain free field data, the experimental results must be corrected for this wall interference. For models which are small in relation to the tunnel height, the standard correction procedures are adequate; however, if the model is appreciably larger, the standard corrections are no longer suitable. A method has been developed which will accurately predict the lift and pitching moment corrections for these extreme geometries.

This estimation of the wall interference is based on an accurate potential flow solution for the flow in the tunnel. The effect of the walls is contained explicitly in the analysis. There are no restrictions on the model size or tunnel geometry, and the method applies equally well to multi-element sections. The solution contains the coupling of the lift interference and solid blockage effects, which is not accounted for in the standard correction procedures.

The method utilizes numerically generated boundary fitted coordinate systems which allow accurate and efficient numerical solutions for regions with irregularly shaped boundaries. The coordinate system is obtained by the finite difference solution of a system of elliptic partial differential equations, using either successive

over-relaxation (SOR) or line successive over-relaxation (LSOR) where appropriate. Several grid topologies have been investigated for application to the problem of determining the wind tunnel corrections for two-dimensional incompressible flow. This investigation resulted in determination of optimal numerical procedures for each grid type. Use of LSOR, where possible, was extremely beneficial in reducing computation time and cost.

Some care is required in choosing a grid which will lead to accurate results. The most appropriate grid geometry for the wind tunnel problem is the slit type, due to the uniformity of the grid properties throughout the solution field. For the multi-element section, using the double-slit geometry, adequate results can be obtained only by extensive use of special grid control functions. The decaying exponential form of the control function is easily implemented and quite adequate for the cases treated here.

The potential flow solution for the stream function is obtained using similar numerical procedures as the grid generation. The lifting potential flow is found by superposition of the basic solutions for uniform onset flow and pure circulatory flow. The circulation of the lifting flow is set by the Kutta condition. Implementation of the Kutta condition in the numerical scheme was investigated in detail: both trailing point and trailing edge velocity conditions were examined in two basic grid types. For the O- and C-type grids, the trailing point condition was superior

due to ease of implementation and the ability to treat sharp trailing edges. For the slit geometries, the velocity condition was superior.

The potential flow numerical solution compares in accuracy with other analysis techniques when suitable grids are used. Comparison of the numerical results for the wind tunnel geometry with free field results obtained using a proven singularity method yielded the desired wall corrections.

To test the accuracy of the numerically generated corrections, wind tunnel tests were carried out on three two-dimensional wing models, including one two-element section, of markedly different geometry and performance. Movement of two large wall inserts within the tunnel allowed testing for a wide range of tunnel geometries. Wind tunnel data was obtained using an accurate and efficient data acquisition system.

The measured wind tunnel data was corrected using both the standard correction forms and the numerically generated corrections. The latter proved to be far superior to the standard forms for extreme tunnel geometries. For all three models the numerical corrections were able to reduce the measured data for a wide range of tunnel geometries to a common set of data indicative of the free field performance. The corrections are most notably accurate for the single element high lift section and the two-element section. For very extreme geometries, however, the corrections become

somewhat in error due to the effect of the tunnel walls on the wing boundary layers through distortion of the airfoil pressure distribution. In this case, it is doubtful that any potential flow based wall correction scheme is suitable. Models with such sensitive boundary layer structure impose special limitations on the allowable test geometries. In general, accurate corrections may be obtained for model chord to tunnel height ratios up to 0.7, nearly double the range of the standard correction forms.

The numerical technique using boundary fitted coordinates is expensive and requires a substantial computer capacity. In addition, some subjective input is required to generate accurate solutions. In this regard, the need for automatic control of the grid properties (the adaptive grids) is well demonstrated. The final solution, however, contains a wealth of easily accessible information. For the wind tunnel problem, the majority of this information is not used. Nonetheless, the results obtained indicate that acceptable accuracy of the solution exists and that finite difference potential flow solutions can be an accurate and useful analysis tool.

References

1. Garner, H.C., Rogers, E.W.E, Acum, W.E.A. and Maskell, E.C. - 'Subsonic Wind Tunnel Wall Corrections', AGARD 109, 1966.

2. Williams, C.D. and Parkinson, G.V. - 'A Low-Correction Wall Configuration for Airfoil Testing', AGARD-CP-174, 1976.

3. Goodyer, M.J., - 'The Low Speed Self-Streamlining Wind Tunnel', AGARD-CP-174, 1976.

4. Vidal, R.J., Erickson, J.C., and Catlin, P.A., - 'Experiments With a Self-Correcting Wind Tunnel', AGARD-CP-174, 1976.

5. Pope, A. and Harper, J. - 'Low Speed Wind Tunnel Testing', John Wiley & Sons, 1966, pp. 300-377.

6. Goldstein, S. - 'Two Dimensional Wind Tunnel Interference', A.R.C. R & M 1902, 1942.

7. Allen, H.J., and Vincenti, W.G. - 'Wall Interference in a Two Dimensional Flow Wind Tunnel, with Consideration of the Effect of Compressibility', NACA Report 782, 1944.

8. Knechtel, E.D. - 'Experimental Investigation of Two-Dimensional Tunnel Wall Interference at High Subsonic Speeds', NACA TN 3087, 1953.

9. Moses, H.E. - 'Velocity Distributions on Arbitrary Airfoils in Closed Tunnels by Conformal Mapping', NACA TN 1899, 1949.

10. Pankhurst, R.C., and Holder, D.W. - 'Wind Tunnel Technique', Pitman & Sons, 1968.

11. Wentz, W.H., and Seetharam, H.C. - 'A Fowler Flap System For A High-Performance General Aviation Airfoil', Paper 740365, SAE Business Aircraft Meeting, Wichita, Kansas, 1974.

12. Foster, D.N., Irwin, H.P.A.H., and Williams, B.R. - 'The Two Dimensional Flow Around A Slotted Flap', ARC R&M 3681, 1970.

13. Kennedy, J.L. - 'The Design and Analysis of Airfoil Sections', Thesis, University of Alberta, 1976.

14. Mokry, M. - 'Influence Function Method in Wind Tunnel Wall Interference Problems', AGARD-CP-174, 1976.

15. de Vries, O., and Schipholt, G.J.L. - 'Two-Dimensional Tunnel Wall Interference for Multi-Element Aerofoils in Incompressible Flow', AGARD-CP-174, 1976.

16. Abbott, I.H., and von Doenhoff, A.E. - 'Theory of Wing Sections', Dover Publications, 1959, pp. 31-63.

17. Milne-Thomson, L.M. - 'Theoretical Aerodynamics', Macmillan, 1966, pp. 83-134.

18. Williams, B.R. - 'An Exact Test Case for the Plane Potential Flow About Two Adjacent Lifting Airfoils', A.R.C. R & M 3717, 1971.

19. Eisemann, P.R. - 'Automatic Algebraic Coordinate Generation', in 'Numerical Grid Generation', (J.F. Thompson, ed.), North-Holland, 1982, pp.447-464.

20. Thompson, J.F., Thames, F.C., and Mastin, C.W. - 'Automatic Numerical Generation of Body-Fitted Curvilinear Coordinate System for Field Containing Any Number of Arbitrary TwoDimensional Bodies', Journal of Computational Physics, 15, pp.299-319, 1974.

21. Thompson, J.F. - 'Numerical Solution of Flow Problems Using Body-Fitted Coordinate Systems', Von Karman Lecture Series - 4, 1978.

22. Kerlick, G.D., and Klopfer, G.H. - 'Assessing the Quality of Curvilinear Coordinate Meshes by Decomposing the Jacobian Matrix', in 'Numerical Grid Generation', (J.F. Thompson, ed.), North-Holland, 1982, pp.787-808.

23. Thompson, J.F. - private communication

24. Thompson, J.F., and Thames, F.C. - 'Numerical Solution of Potential Flow About Arbitrary Two-Dimensional Multiple Bodies', MSSU-EIRS-ASE-82-2, 1976.

25. Brackbill, J.U. - 'Coordinate System Control: Adaptive Meshes', in 'Numerical Grid Generation', (J.F. Thompson, ed.), North-Holland, 1982, pp.277-294.

26. Anderson, D.A., and Rai, M.M. - 'The Use of Solution Adaptive Grids in Solving Partial Differential Equations', in 'Numerical Grid Generation', (J.F. Thompson, ed.), North-Holland, 1982, pp.317-338.

27. Houghton, E.L., and Brock, A.E. - 'Aerodynamics for Engineering Students', Arnold, 1977, pp. 83-85.

28. Hamming, R.W. - 'Numerical Methods for Scientists and Engineers', McGraw-Hill, 1973.

29. Schlicting, H. - 'Boundary Layer Theory', 6th Edition, McGraw-Hill, 1968, p.712.